Universitat Autònoma de Barcelona

Stochastic multi-scale modelling of tumour growth

Roberto de la Cruz Moreno

Stochastic multi-scale modelling of tumour growth

Tesis Doctoral

Autor: Roberto de la Cruz Moreno

Director/Tutor: Tomás Alarcón Cor

Director: Pilar Guerrero Contreras

Universitat Autònoma de Barcelona

Centre de Recerca Matemàtica

Programa Doctorado en Matemáticas

Año depósito: 2017

Contents

Chapter 1

Introduction

1.1 What is cancer?

The concept of cancer spans a large set of genetic diseases characterised by uncontrolled cell growth within a group of cells (cancer cells or abnormal cells), which have the ability to spread and invade other parts of the body (metastasis). Cancer encompasses a number of different situations: benign and malignant. A tumour that does not have the potential to invade is called a benign tumour, otherwise it is referred to as a malignant tumour or a cancerous tumour. Benign tumours (which do not belong to the carcinogenic category) are localised and non-invasive (e.g. ductal carcinoma in situ). Malignant tumours have the ability of invading the surrounding tissue and other parts of the body. "Liquid tumours" are also prevalent among malignancies such as haematological tumours (e.g. leukaemia).

Cancer starts with the mutation of one or a small number of normal cells, triggering an uncontrolled cell growth (neoplasm). In solid tumours, growth is initially limited by the availability of resources (avascular phase); under these conditions of restricted access to nutrients, in particular oxygen, a portion of the avascular tumour cell population becomes hypoxic. This triggers the angiogenic switch, whereby cells secrete angiogenic factors, in particular, VEFG (Vascular Endothelial Growth Factor). Secretion of angiogenic factors triggers angiogenesis, i.e. the formation of new blood vessels by sprouting from the existing native vasculature. The new vasculature provides unlimited resources and the possibility that cancer cells migrate and invade other tissues and organs of the body (metastasis) [229]. A more comprehensive picture of cancer as a multi-step process is provided by Hanahan and Weinberg, under their celebrated "Hallmarks of Cancer" paradigm [91, 92]. According to this paradigm, all types of cancer obtain eight hallmarks of biological capabilities: to keep proliferative signalling, avoiding tumour suppressor genes, resisting apoptosis, unlimited replicative potential, angiogenesis, invasion, reprogramming energy metabolism and evading immune destruction [92]. These hallmarks are explained below:

- Keeping proliferative signalling: normal tissue maintains homeostasis through the production and release of growth-regulating signals. These signals guide the evolution through the cell division cycle. However, cancer cells have different mechanisms for evading this control and grow unlimitedly. Mechanisms used by cancer cells to evade homeostatic control include, but are not limited to, produce growth factor ligands, release signals to stimulate normal cells which reciprocatively stimulate the cancer cells and decrease the threshold of the receptors (making the cancer cells response to those lower signal concentration).

- Avoiding tumour suppressor genes: tumour suppressor genes possess the ability to inhibit cell division. However, in cancer cells, tumour suppressor genes cannot be expressed (due to their recessive trait). Thereby, they are unable to prevent cell division when necessary. This gives rise to uncontrolled growth of the tumour.

- Resisting apoptosis: apoptosis is the programmed cell death triggered by the organism itself, as a means of homeostatic control, as well as to eliminate damaged cells in order to avoid its replication. Cancer cells resist apoptosis in many ways: lack of equilibrium between pro-apoptotic and anti-apoptotic proteins, reducing caspase (key set of enzymes in apoptosis) function and impairing death receptor signalling, among others.

- Unlimited replicative potential: most normal cells can divide only a limited number of times, due to telomere shortening during the division process. Telomere is a region at the ends of each chromosome which protects it from deterioration and union with other chromosomes. However, cancer cells can present high telomerase activity (enzyme that add nucleotides at the ending of the telomere) thus compensating for telomere shortening leading to more duplication per cell.

- Angiogenesis: normally, in the early stages, solid tumours grow without blood supply to a maximum size limited by the amount of nutrients and metabolites that diffuse through its surface. Usually, in response to the lack of oxygen in the environment, the cancer cells secrete TAFs (tumour angiogenic factors) such as VEGF, which diffuse across the tissue until a vasculature zone. Consequently, those factors stimulate the formation of newly sprouting blood vessels which migrate (via chemotaxis) to the source of TAFs. The tumour has access to potentially unlimited resources and, eventually, a chance for invasion with adequate blood supply.

- Invasion: metastasis is in itself a multi-step process. Firstly, local infiltration of cancer cells into the adjacent tissue occurs, followed by intravasation (transendothelial migration into vessels). If metastatic cells survive their sojourn through the circulation, they eventually will extravasate. With a certain probability, which depends on the origin of the invader and the receptor tissues ("Seed and soil" theory) extravasated cells will start proliferating leading to the seeding of a (micro-)metastasis.

- Reprogramming energy metabolism: an uncontrolled cell proliferation implies an increase of energy consumption. Thus, cancer cells use a different metabolic pathway for glucose than normal cells. This pathway is more inefficient but it is much faster ("effect Warburg": cancer cells consume more than 20 times as much glucose compared to normal cells). Cancer cells produce ATP faster than normal cells. Also, this pathway produces intermediate biosynthetic precursos, used for the production of proteins, lipids and DNA (necessary for cell division).

- Evading immune destruction: there are points in common between cancer and wound healing: growth, formation new blood vessels and migration of cells (processes lead by growth factors). As immune cells secrete growth factors to help tissue repair, tumorus can use the same immune cells to promote their uncontrolled cell growth.

1.2 The *magic bullet* approach to therapy

Cancer is one of the principal causes of death in the world. According to the WHO (World Health Organization), in 2015 it was the second leading cause of death globally (approximately 1 in 6 deaths were due to cancer). Besides, it is expected that in the next two decades the number of new cases will rise by 70% [231]. The proportion of deaths is growing within the ever increasing aging population.

Despite all the resources invested in research for the development of new targeted therapies, the most used treatments to fight cancer continue to be non-specific therapies, such as surgery, radiotherapy and chemotherapy, that affect both healthy and cancer cells (see e.g. Fig 1.1). In contraposition to unspecific therapies, an alternative approach has been used in medicine that is commonly referred to as *the magic bullet* to guide the development of new targeted therapies. The concept consists of finding a drug with a specific target (gene, protein, etc.) implicated at a particular stage of development of the disease by killing just unhealthy cells whilst leaving normal cells unharmed. Although it is not a new approach, its impact on complex diseases has been discreet [154]. The precursor of this idea was the Nobel laureate Paul Erhlich in the early 20th century. Consequently, Ehrlich's work inspired multiple successful investigations as did the antibacterial drug research of Alexander Fleming [207].

A few decades ago, with the birth of the genomic technology, *the magic bullet* approach was expected to finally come to fruition, as new omics techniques allow to identify abnormalities of individual tumours, which then become potential targets (e.g. personalised medicine). Thus, the principal aim of oncological research has been to develop targeted therapies to find drugs that interfere at various stages of the cancer growth and progression. However, the efficiency of these new therapies has been rather modest [154]. In spite of important projects as *The Cancer Genome Atlas (TGCA)*,

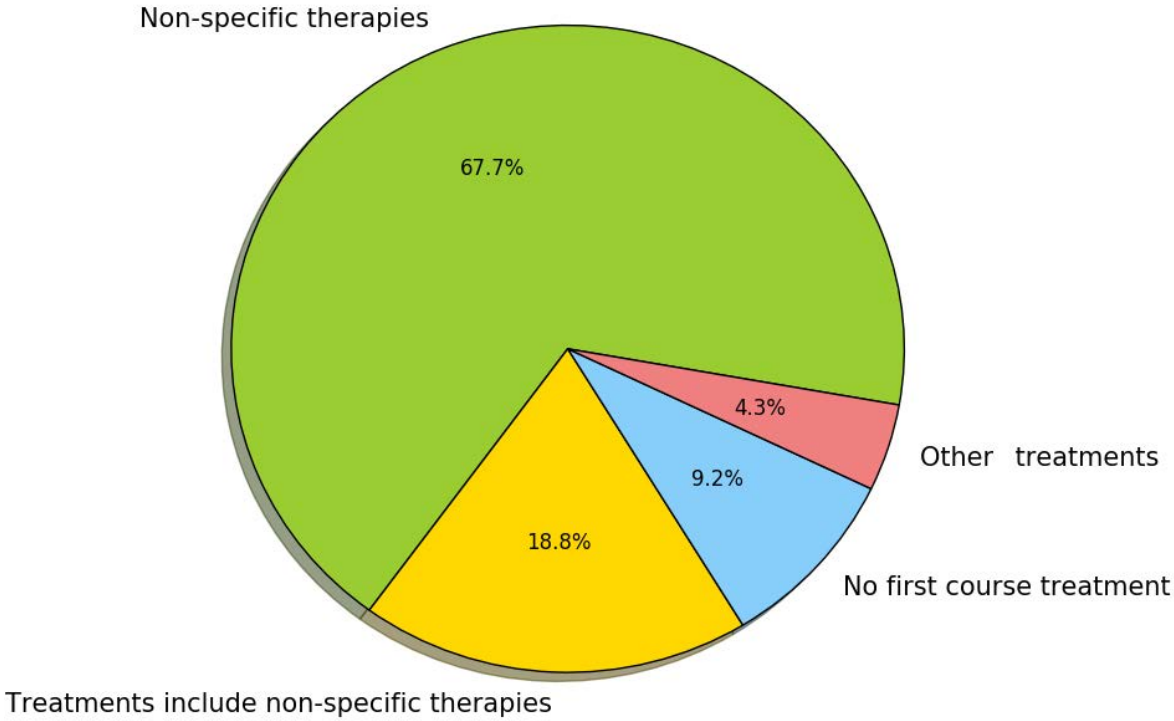

Figure 1.1: First course treatments of all cancer diagnosed in USA from 2004 to 2014 [165]

the *Cancer Genome Project* and the *International Cancer Genome Consortium* [108], the success of these new drugs against cancer has been very low [3, 171, 208].

The lack of effectiveness of the *magic bullet* approach brings about two questions: *Why does that approach fail in the case of cancer?* and *What do we do to improve its effectiveness?*.

There are various reasons why that approach has not been widely successful at replacing non-specific therapies. Tumours exhibit remarkable intratumoral cellular heterogeneity. Cellular heterogeneity often produces a sub-population of cancer cells to survive an anticancer therapy and lead to tumour reappearance [95, 101, 162, 163]. Tumours also employ a number of systems used to endure hazardous enviroments (e.g. hypoxia) [131]. They present multiple mechanisms whose functions allow to minimise cytotoxin levels [160, 190], block apoptosis [236, 237] or withstand hypoxic environment [86, 94, 103, 132].

Besides all the mechanisms of drug resistance in tumours, there are also reasons for

the failure of magic bullet approaches, which have to do with the intrinsic complexity and multi-scale nature of tumours. The behaviour and traits of biological systems are influenced by a complex network of interactions between genes and gene products which regulate gene expression. The non-linear, high-dimensional dynamical structures have undergone evolutionary changes by natural selection. As time progresses, the resilience of the phenotype against genetic alteration increases allowing canalisation (the ability to become more robust). Particularly, in malignancies these properties and structures are exploited by the tumour to increase its proliferative potential and resist therapies. The layers of complexities involved within the system, induce difficulties in predicting the effect of a perturbation applied in the system [89]. In order to successfully address the issues, a huge amount of research has been undertaken involving analysis and development of multi scale models. These models incorporate different sub-models corresponding to different biological levels such that the global tissue behaviour could be analysed as an emergent property of the coupled elements [34, 45, 147, 168, 186, 218].

1.3 Multi-scale modelling

The intrinsic complexity of the biological processes, together with the wide range of temporal and spatial scales over which they operate and the complicated way in which they are coupled, makes multi-scale approaches fundamental in the field of Systems Biology. Tissues in living organisms are organised in different structural integration levels (see Fig. 1.2), namely, an intracellular level (including genes, molecules and all their regulatory machinery), a cellular level (which accounts for all processes that have to do with interactions between cells), and a tissue level (which encompasses all those processes involving large ("macroscopic") numbers of cells). All these levels possess an intrinsically complex dynamics, which additionally, is coupled to all others (see Fig.1.2 for illustration). The highly non-linear dynamics of these systems cause the perturbations affecting single levels to provoke significant global effects (see Fig 1.2).

Recently, multi-scale modelling has become an important topic in the biological systems field, including areas like cardiology [93, 139, 153, 203], developmental biology [99, 164, 196, 199, 227] or tumour growth [5, 34, 45, 52, 116, 147, 149, 168, 170, 176, 180, 181, 186, 187, 211, 218, 219].

One of the principal features of biological systems is their complexity. Modelling in any field means to reduce the complexity of the system as much as possible and, at the same time, trying to retain the maximum amount of information. Therefore, this could pose to be a difficult challenge in the case of biological systems particularly.

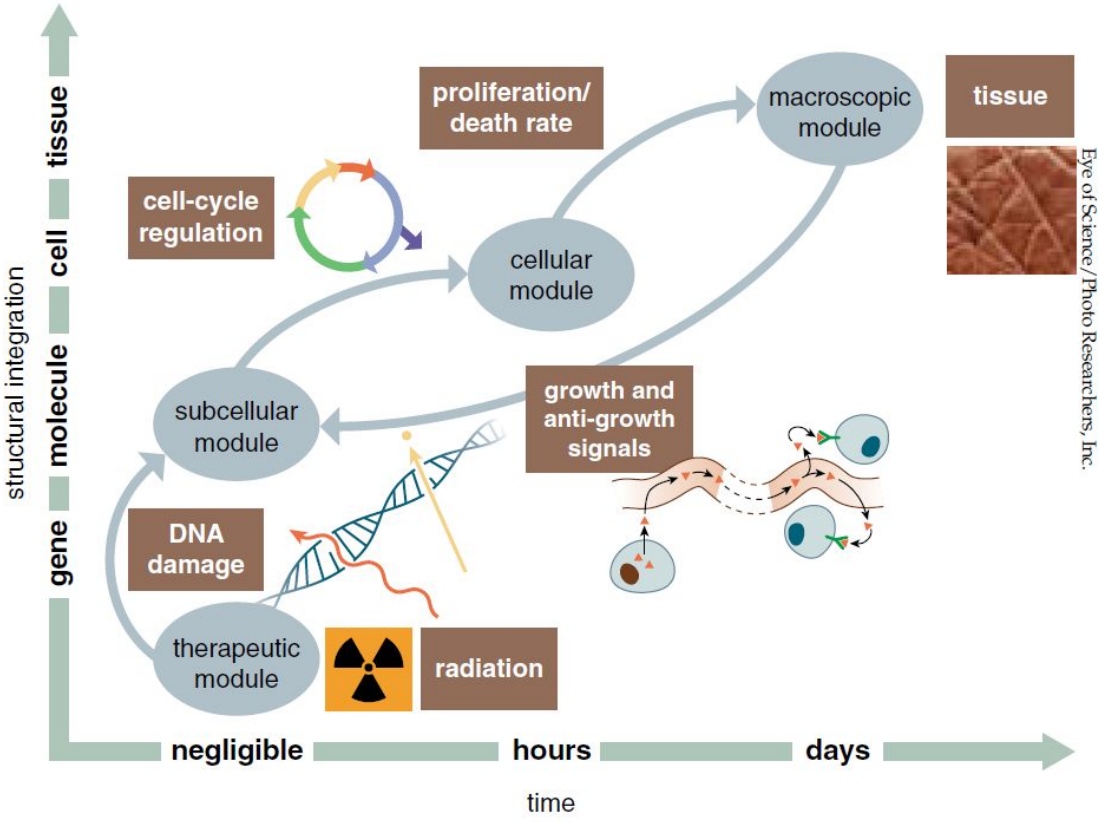

Figure 1.2: Biological processes are multiscale phenomena

As previously mentioned, the multi-scale modelling is necessary since biological processes are a multi-scale phenomena. It is the behaviour of these processes that have attributed to the emergent property of non-linear coupling between systems with different time and length scales. Hence, it is extremely difficult to predict the effect of a perturbation at a particular level. However, this modelling presents certain problems when trying to simulate all that is possible. As an example, we could consider the 3D multi-scale modelling of angiogenesis and vascular tumour growth developed in [176]. The model couples:

- ODE models of signalling pathways (for example VEGF)
- ODE models of intracellular pathways (for example between extra-cellular oxygen and cell cycle)
- Cellular automata models of competition between normal and cancer cells for resources.
- Reaction-diffusion PDEs for the oxygen and signalling cues.
- Continuous models for blood flow and angiogenesis.

The results of the simulations of this model are satisfactory (see Fig 1.3). However, the model is too complex and the analysis is even more difficult. One of these issues concerns computational costs. Simulation of IBMs (individual-based models) in which individual cells and their intracellular states are resolved impose heavy computational costs, since we must keep track of their temporal evolution. They also normally contain a large number of parameters which are difficult to estimate using standard methods such as Bayesian inference or Approximate Bayesian Computation. Beyond these "technical" issues, current multiscale models do not account for the effects of random fluctuations. Such effects are known to radically affect the dynamics at the intracellular level ([2, 16, 35, 55, 90, 138, 146, 148, 151, 175, 182]). Random effects also dominate the dynamics at the cell population level whenever cell numbers are small enough (e.g. the dynamics of small micro-metastase [90]).

The formulation of these models can be developed from different points of view. Among the most relevant are IBMs, off-lattice models and hybrid models. IBMs focus on the behaviour of the individuals (in our case cells) of the system and the interactions among them. This approach allows us to study the emergent behaviour that arises from the interactions between individuals beyond the continuum classic methods and to capture the heterogeneity of the population. However, the computational cost is usually high, meaning that, unless high performance computing facilities are available, only small cell numbers can be simulated. IBMs have had an important repercussion in a number of fields. For example, in ecology, models of forest dynamics [24, 145, 201] or schooling fish dynamics [109, 110, 111, 136] have been developed. We could differentiate two types of IBM models: the lattice-based models where each individual (cell) solely could be in a determined position of a specific lattice; and the off-lattice models where the individuals are located (and move) in a continuous domain, the latter being more relevant.

In lattice models, the behaviour of cells regarding its interactions with other cells is determined by a set of prefixed rules (e.g. cellular automata (CA) models [97, 117] or cellular Potts model (CPM) [169, 221]), being computationally less expensive than the off-lattice models. Nevertheless, the lattice models do not consider, for example, the mechanical properties of the cells. Off-lattice models are necessary for considering such properties and are a more suitable framework to study phenomena such as cell migration. Normally, the cell shapes in the off-lattice models are spheres, ellipsoids or shapes within a Voronoi tessellation and the interactions amongst them are modelled by Netwon's law, although the nature of the forces varies depending on the model. In the particular case of cell growth, off-lattice models have the capacity to explain processes such as growth and pattern formation of cell populations under standard culture conditions [66] or the growth of avascular tumours in suspension [51].

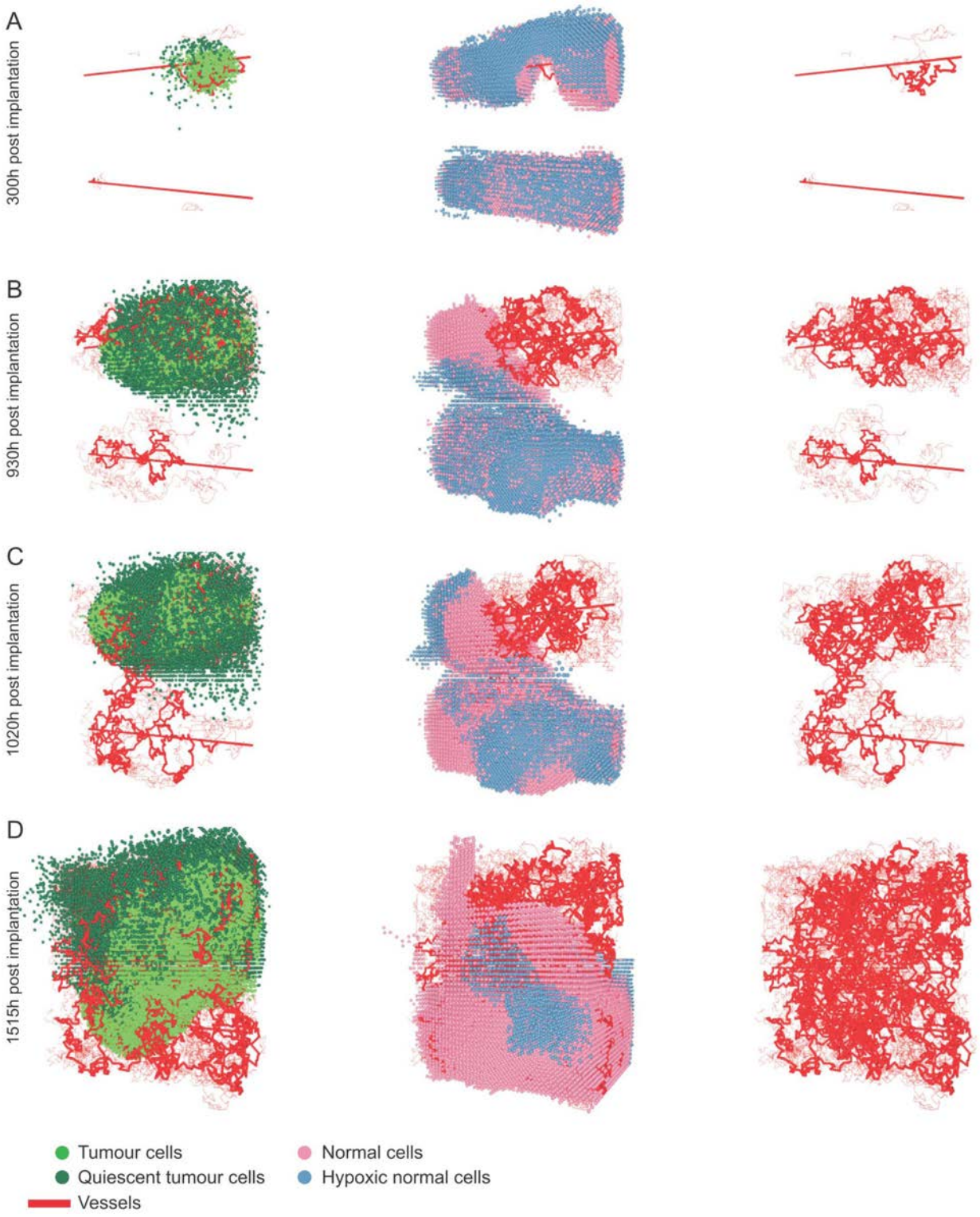

Figure 1.3: Simulation result of the tumour growth model developed in [176]

Another approach which is gaining importance is the hybrid modelling (combination of continuous and discrete formulations) [6, 127, 149, 168, 186, 187]. These models are formed by different sub-models, each modelled in terms of different mathematical descriptions (PDEs, ODEs, etc.). These models normally use IBM for the dynamics of one or more cellular compartments of the model [170, 176] and the other phases are modelled as continuous phases [127, 149]. These models have been invested in the evolutionary dynamics of tumour growth [186] as well as in the angiogenesis [149, 170, 176] or the response to therapy [6, 187].

Nevertheless, despite all the prevalent research conducted in recent times, certain major aspects are not well treated by most of these models. One of the most consistent limitations is that of the noise and its impact. Although several models consider random effects [170, 176], there doesn't exist a general method to add and to analyse the effects of noise. The objective of this thesis is the development of stochastic multi-scale modelling in tumour growth.

1.4 Aim and structure of the thesis

Multi-scale models of the types discussed in the previous section are known to be affected by a number of issues. The principal aim of this thesis is the formulation and analysis of stochastic multi-scale model of the dynamics of cellular populations that shed light on:

- The effects of coupling between intrinsic fluctuations at the intracellular and population levels. We aim to establish how the different sources of noise affect global properties of growing tumours, such as the speed of invasion.
- Derive coarse-grained limits of these models so that the parameters of the multi-scale models can be lumped together into a smaller number of parameters. This will facilitate the task of parameter estimation.
- To formulate hybrid methods which allow us to simulate larger systems while losing none of the essential features of the multi-scale system.

To this end, we establish a systematic way to consider the noise in multi-scale models.

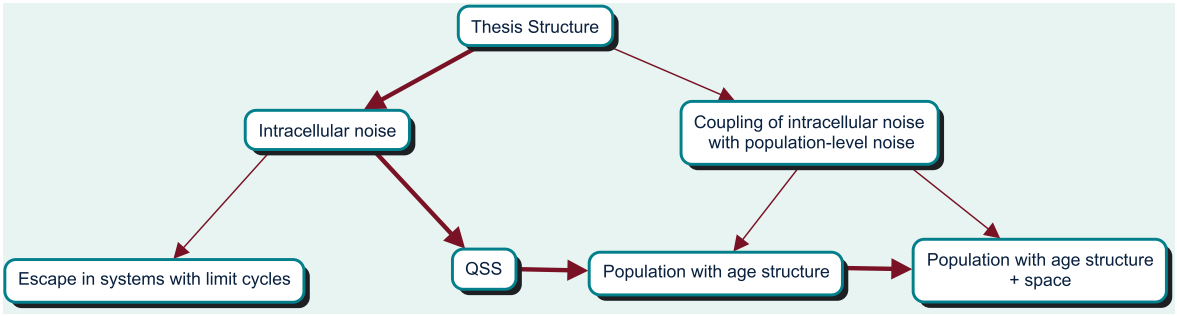

Figure 1.4: This thesis is structured into two parts, namely, a first part which concerns intracellular noise in isolation, and a second part where both intracellular and population fluctuations are considered.

In the first chapter we start to assemble the model from the intracellular level where we analyse the effects of the intrinsic fluctuations at an intracellular level. We consider a stochastic version of a bistable system which is part of the G_1/S transition of the eukaryote cell cycle model proposed in [224]. We formulate the chemical reactions in terms of the chemical master equation (CME) [120] and we use the semi-classic quasi-steady state to resolve it. In particular, we aim and analyse the effect of intrinsic fluctuations on the properties of bistable stochastic systems with time scale separation operating under quasi-steady state conditions. To this end, we first formulate a stochastic generalisation of the quasi-steady state approximation based on the semi-classical approximation of the partial differential equation for the generating function associated with the Chemical Master Equation. Such approximation proceeds by optimising an action functional whose associated set of Euler-Lagrange (Hamilton) equations provide the most likely fluctuation path. We show that, under appropriate conditions granting time scale separation, the Hamiltonian can be re-scaled so that the set of Hamilton equations splits up into slow and fast variables, whereby the quasi-steady state approximation can be applied. Our theory establishes that the number of molecules of the conserved species are order parameters whose variation regulates bistable behaviour in the associated systems beyond the predictions of the mean-field theory. This prediction is fully confirmed by direct numerical simulations using the stochastic simulation algorithm. This result allows us to propose strategies whereby, by varying the number of molecules of the three conserved chemical species, cell properties associated with bistable behaviour (phenotype, cell-cycle status, etc.) can be controlled.

The next chapter considers the escape problem in biochemical systems with limit cycles. Cell state determination is the outcome of intrinsically stochastic biochemical reactions. Transitions between such states are studied as noise-driven escape problems in the chemical species space. Escape can occur via multiple possible multidimensional paths, with probabilities depending non-locally on the noise. Here, we characterise

the escape from an oscillatory biochemical state by minimising the Freidlin-Wentzell action, deriving from it the stochastic spiral exit path from the limit cycle. We also use the minimised action to infer the escape time probability density function.

We then move to the second part of thesis where we consider the cell-population level. In Chatper 4, we analyse the properties of heterogeneous populations under the effects of fluctuations both within the intracellular pathways regulating (individual) cell behaviour those associated with intrinsic randomness due to finite size of the population. We propose a modelling framework to analyse the stochastic behaviour of heterogeneous, multi-scale cellular populations. We illustrate our methodology with a particular example in which we study a population with an oxygen-regulated proliferation rate. Our formulation is based on an age-dependent stochastic process. Cells within the population are characterised by their age (i.e. time elapsed since they were born). The age-dependent (oxygen-regulated) birth rate is given by a stochastic model of oxygen-dependent cell cycle progression. Once the birth rate is determined, we formulate an age-dependent birth-and-death process, which dictates the time evolution of the cell population. The population is under a feedback loop which controls its steady state size (carrying capacity): cells consume oxygen which in turns fuels cell proliferation. We show that our stochastic model of cell cycle progression allows for heterogeneity within the cell population induced by stochastic effects. Such heterogeneous behaviour is reflected in variations in the proliferation rate. Within this set-up, we have established three main results. First, we have shown that the age to the G1/S transition, which essentially determines the birth rate, exhibits a remarkably simple scaling behaviour. Besides the fact that this simple behaviour emerges from a rather complex model, this allows for a huge simplification of our numerical methodology. A further result is the observation that heterogeneous populations undergo an internal process of quasi-neutral competition. Finally, we investigated the effects of cell-cycle-phase dependent therapies (such as radiation therapy) on heterogeneous populations. In particular, we have studied the case in which the population contains a quiescent sub-population. Our mean-field analysis and numerical simulations confirm that, if the survival fraction of the therapy is too high, rescue of the quiescent population occurs. This gives rise to emergence of resistance to therapy since the rescued population is less sensitive to therapy.

Finally, we consider spatially heterogeneity. The development of hybrid methodologies is of current interest in both multi-scale modelling and stochastic reaction-diffusion systems regarding their applications to biology. We formulate a hybrid method for stochastic multi-scale models of cells populations that extends the remit of existing hybrid methods for reaction-diffusion systems. Such method is developed for a stochastic multi-scale model of tumour growth, i.e. population-dynamical models which account for the effects of intrinsic noise affecting both the number of cells and the intracellular dynamics. In order to formulate this method, we develop a coarse-grained approximation for both the full stochastic model and its mean-field limit. Such approximation

involves averaging out the age-structure (which accounts for the multi-scale nature of the model) by assuming that the age distribution of the population settles onto equilibrium very fast. We then couple the coarse-grained mean-field model to the full stochastic multi-scale model. By doing so, within the mean-field region, we are neglecting noise in both cell numbers (population) and their birth rates (structure). This implies that, in addition to the issues that arise in stochastic-reaction diffusion systems, we need to account for the age-structure of the population when attempting to couple both descriptions. We exploit our coarse-graining model so that, within the mean-field region, the age-distribution is in equilibrium and we know its explicit form. This allows us to couple both domains consistently, as upon transference of cells from the mean-field to the stochastic region, we sample the equilibrium age distribution. Furthermore, our method allows us to investigate the effects of intracellular noise, i.e. fluctuations of the birth rate, on collective properties such as travelling wave velocity. We show that the combination of population and birth-rate noise gives rise to large fluctuations of the birth rate in the region at the leading edge of front, which cannot be accounted for by the coarse-grained model. Such fluctuations have non-trivial effects on the wave velocity. Beyond the development of a new hybrid method, we thus conclude that birth-rate fluctuations are central to a quantitatively accurate description of invasive phenomena such as tumour growth.

Part 1

Intracellular noise

Chapter 2

The effects of intrinsic noise on the behaviour of bistable cell regulatory systems under quasi-steady state conditions

2.1 Introduction

The networks of interacting genes and proteins that are responsible for regulation, signalling and response, and which, ultimately, orchestrate cell function, are under the effect of noise [118, 125, 146, 151, 182]. It is this randomness that materialises in the form of fluctuations of the number of molecules of the species involved, subsequently leading to fluctuations in their activity. Besides external perturbations, biochemical reactions can be intrinsically noisy, especially when the number of molecules are very low.

Far from necessarily being a mere disturbance, fluctuations are an essential component of the dynamics of cellular regulatory systems which, in many instances, are exploited to improve cell function [35, 55]. For example, randomness has been shown to enhance the ability of cells to adapt and increase their fitness in random or variable environments [2, 89, 138]. Random noise also serves the purpose of assisting cell populations to sustain phenotypic variation by enabling cells to explore the phase space. [16, 55, 146, 148, 151, 182].

One of the mechanisms that allows noise-induced phenotypic variability relies on multi-stability [40, 114]. The basis of this mechanism was first proposed by Kauffman [122], who associated phenotypes or differentiated states to the stable attractors of the dynamical systems associated to gene and protein interaction networks. In the presence of noise, the corresponding phase space generates an epigenetic landscape, where cells exposed to the same environment and signalling cues can coexist in different cellular

phenotypes [106].

Multi-stability is also an essential element in the control of cell response and function via signalling pathways [223]. In particular, bi-stability as a means to generate reliable switching behaviour is widely utilised in numerous pathways such as apoptosis [141], cell survival [142], differentiation [119], and cell-cycle progression [58, 224] pathways. For example, bi-stability is used to regulate such critical cell functions as the transition from quiescence to proliferation through bistable behaviour associated with the Rb-E2F switch within the regulatory machinery of the mammalian cell-cycle [18, 71, 73, 74, 234, 233].

A common theme which appears when trying to model cell regulatory systems is separation of time scales. When noise is ignored and systems are treated in terms of deterministic mean-field descriptions, such separation of time scales and the associated slow-fast dynamics are often exploited for several forms of model reduction, of which the most common is the so-called quasi-steady state approximation (QSSA) [123]. This approximation is ubiquitously used whenever regulatory processes involve enzyme catalysis, which is a central regulation mechanism in cell function [223]. In this chapter, we investigate the effects of intrinsic noise on the bi-stability of an enzyme-catalysed system of mutual inhibition. The mean-field limit of that system has been shown to exhibit bi-stability [224]. The aim is to analyse how noise alters the mean-field behaviour associated to these systems when they operate under quasi-steady state conditions.

We note that we do not concern ourselves with the subject of noise-induced bifurcations [67]. Such phenomenon has been studied in many situations, including biological systems. An example which is closely related to the system we analyse here is the so-called enzymatic futile cycles. Samoilov et al. [193] have shown that noise associated to the number of enzymes induce bistability. In the absence of this source of noise, i.e. in the mean-field limit, the system does not exhibit bistable behaviour. The treatment of this phenomena would require to go to higher orders in the WKB expansion, which we do not explore here.

The issue of separation of time scales in stochastic models of enzyme catalysis has been addressed using a number of different approaches. Several such analysis have been carried out in which the QSSA is directly applied to the master equation by setting the fast reactions in partial equilibrium (i.e. the probability distribution corresponding to the fast variables remains unchanged), and letting the rest of the system to evolve according to a reduced stochastic dynamic [183, 222]. Other approaches have been proposed such as the QSSA to the exact Fokker-Planck equation that can be derived from the Poisson representation of the chemical master equation [216]. Approaches based on enumeration techniques have also been formulated [50]. Furthermore, Thomas et al.[215] have recently formulated a rigorous method to eliminate fast stochastic vari-

ables in monostable systems using projector operators within the linear noise approximation [215]. Methods for model reduction based on perturbation analysis have been developed in [4, 31]. Additionally, driven by the need of more efficient numerical methods, there has been much activity regarding the development of numerical methods for stochastic systems with multiple time-scales [33, 150, 226]. Several of these methods are variations of the stochastic simulation algorithm [36, 37, 54, 183, 192, 195] or the τ-leap method [184] where the existence of fast and slow variables is exploited to enhance their performance with respect to the standard algorithms. Another family of such numerical methods is that of the so-called hybrid methods, where classical deterministic rate equations or stochastic Langevin equations for the fast variables are combined with the classical stochastic simulation algorithm for the slow variables [96, 191]. Other related methods were studied in [13, 121, 159].

Here, we advance the formalism developed in [4], in which a method based on the semi-classical approximation of the Chemical Master Equation allows to evaluate the effects of intrinsic random noise under quasi-steady conditions. In the analysis of the Michaelis-Menten model of enzyme catalysis in [4], it is shown that the semi-classical quasi-steady state approximation reveals that the velocity of the enzymatic reaction is modified with respect to the mean-field estimate by a quantity which is proportional to the total number of molecules of the (conserved) enzyme. We extend this formalism to show that, associated to each conserved molecular species, the (constant) number of molecules is a bifurcation parameter which can drive the system into bi-stability beyond the predictions of the mean-field theory. We then proceed to test our theoretical results by means of direct numerical simulation of the Chemical Master Equation using the stochastic simulation algorithm [76]. We should note the Hamiltonian formalism derived from the semi-classical approximation is formulated on a continuum of particles, which requires the number of particles to be large enough. This must hold true for all the species in our model, both fast and slow. Since this separation between fast and slow species is based on their relative abundance, one must be careful that the scaling assumptions are consistent. This assumption, however, has been used in previous studies [15]. We also show that our simulation results of the full stochastic processes agree with our analysis and, therefore, our re-scaled equations are able to predict the behaviour of the system.

The approximation we develop falls within the general framework of the optimal fluctuation path theory [26]. This framework is a particular case of large deviation theory which allows us to study rare events (i.e. events whose frequency is exponentially small with system size). Within these framework we will show that, upon carrying out the QSSA, the only source of noise in the system is associated to the random initial conditions of the species whose numbers are conserved. We therefore predict that a population of cells, each having a random number of conserved molecules, will have a bimodal distribution.

This chapter is organised as follows. Next section is devoted to a detailed exposition of the semi-classical quasi-steady state approximation for stochastic systems. In Section 2.3 we apply this formalism to analyse the behaviour of a bistable enzyme-catalysed system. We will show that our semi-classical quasi-steady state theory allows us to study the effect of intrinsic noise on the behaviour of this system beyond the predictions of their mean-field descriptions. We also verify our theoretical predictions by means of direct stochastic simulations. In the Chapter 6, in Section 6.1.1, we summarise our results and discuss their relevance.

2.2 Semi-classical quasi-steady state approximation

In this section we introduce a stochastic generalization of the quasi-steady state approximation and use such approximation to determine the effects of the noise on the behaviour of the system beyond the predictions of the corresponding mean-field model. We investigate how our stochastic system, whose mean-field model predict bistability, is affected for stochastic effects.

The analysis is carried out in the context of Markovian models of the corresponding reaction mechanisms formulated in terms of the so-called chemical master equation (CME) [120]. Following [4], we formulate the QSS approximation for the asymptotic solution of the CME obtained by means of large deviations/WKB approximations [8, 135, 217]. The CME is given:

$$\frac{\partial P(X,t)}{\partial t} = \sum_i (W_i(X - r_i)P(X - r_i, t) - W_i(X)P(X,t)) \tag{2.2.1}$$

where $P(X,t)$ is the probability of the molecular species vector to be X at time t, $W_i(X)$ is the transition rate corresponding to reaction channel i and r_i is a vector whose entries denote the change in the number of molecules of each molecular species when reaction channel i fires up, i.e. $P(X(t+\Delta t) = X(t) + r_i | X(t)) = W_i(X)\Delta t$.

An way to analyse the dynamics of continuous-time Markov processes on a discrete space of states is to derive an equation for the generating function, $G(p_1, \ldots, p_n, t)$ of the corresponding probabilistic density:

$$G(p_1, \ldots, p_n, t) = \sum_x p_1^{X_1} p_2^{X_2} \cdots p_n^{X_n} P(X_1, \ldots, X_n, t) \tag{2.2.2}$$

where $P(X_1, \ldots, X_n, t)$ is the solution of the Master Equation (2.2.1). G satisfies a partial differential equation (PDE) which can be derived from the Master Equation. This PDE is the basic element of the so-called momentum representation of the Master Equation [14].

Although closed, analytic solutions are rarely available, the PDE for the generating function admits a perturbative solution, which is commonly obtained by means of the WKB method [14]. More specifically, the (linear) PDE that governs the evolution of the generating function can be written as:

$$\frac{\partial G}{\partial t} = H_k\left(p_1, \ldots, p_n, \partial_{p_1}, \ldots, \partial_{p_n}\right) G(p_1, \ldots, p_n, t) \tag{2.2.3}$$

where the operator H_k is determined by the reaction rates of the Master Equation (2.2.1). Furthermore, the solution to this equation must satisfy the normalisation condition $G(p_1 = 1, \ldots, p_n = 1, t) = 1$, for all t. This PDE, or, equivalently, the operator H, are obtained by multiplying both sides of the Master Equation (2.2.1) by $\prod_{i=1}^{n} p_i^{X_i}$ and summing up over all the possible values of $(X_1, \ldots, X_n)$. In the particular case in which every transition rate is a linear polynomial and the amount of any specie changes at most one, there is a systematic way to calculate that PDE:

We suppose in (2.2.1) that the transition rate of reaction i, $W_i(X)$, is expressed as

$$W_i(X) = k_i X_{i_1} X_{i_2} \cdots X_{i_m}, \quad \{i_1, i_2, \cdots, i_m\} \subset \{1, 2, ..., n\},$$

and we assume that the components of vector r_i are $+1$, -1 or 0. We denote by $r_i(j)$ the component j of r_i. Let:

$$A_i = \{a | r_i(a) = -1\} = \{a_1, \cdots, a_\alpha\},$$

$$B_i = \{b \notin \{i_1, \cdots, i_m\} | r_i(b) = 1\} = \{b_1, \cdots, b_\beta\}$$

and

$$D_i = \{d \in \{i_1, \cdots, i_m\} | r_i(d) = 1\} = \{d_1, \cdots, d_\delta\}$$

Note that if $z \in A_i$ then $z \in \{i_i, \cdots, i_m\}$ (because of $x_k \geq 0$). Let

$$C_i = \{c \in \{i_1, \cdots, i_m\} | r_i(c) = 0\} = \{c_1, \cdots, c_\gamma\}$$

Then:

$$\begin{aligned} &\sum_x p_1^{X_1} p_2^{X_2} \cdots p_n^{X_n} (W_i(X - r_i) P(X - r_i) - W_i(X) P(X)) = \\ &= k_i (p_{b_1} \cdots p_{b_\beta} p_{c_1} \cdots p_{c_\gamma} p_{d_1}^2 \cdots p_{d_\delta}^2 - p_{i_1} \cdots p_{i_m}) \frac{\partial G}{\partial p_{i_1} \cdots \partial p_{i_m}} \end{aligned} \tag{2.2.4}$$

From the mathematical point of view, Eq. (2.2.3) is a Schrödinger-like equation and, therefore, there is a plethora of methods at our disposal in order to analyse it. In particular, when the fluctuations are (assumed to be) small, it is common to resort to WKB methods [8, 85, 135]. This approach is based on the WKB-like Ansatz that

$G(p_1,\ldots,p_n,t) = e^{-S(p_1,\ldots,p_n,t)}$. By substituting this Ansatz in Eq. (2.2.3) we obtain the following Hamilton-Jacobi equation for the function $S(p_1,\ldots,p_n,t)$:

$$\frac{\partial S}{\partial t} = -H_k\left(p_1,\ldots,p_n,\frac{\partial S}{\partial p_1},\ldots,\frac{\partial S}{\partial p_n}\right) \tag{2.2.5}$$

Instead of directly tackling the explicit solution of Eq. (2.2.5), we will use the so-called semi-classical approximation. We use the Feynman path-integral representation which yields a solution to Eq. (2.2.3) of the type [46, 56, 59, 135, 213]:

$$G(p_1,\ldots,p_n,t) = \int_0^t e^{-S(p_1,\ldots,p_n,Q_1,\ldots,Q_n)}\mathcal{D}Q(s)\mathcal{D}p(s), \tag{2.2.6}$$

where $\mathcal{D}Q(s)\mathcal{D}p(s)$ indicates integration over the space of all possible trajectories and $S(p_1,\ldots,p_n,Q_1,\ldots,Q_n)$ is given by [135]:

$$\begin{aligned} &S(p_1,\ldots,p_n,Q_1,\ldots,Q_n) = \\ &-\int_0^t\left(H_k(p_1,\ldots,p_n,Q_1,\ldots,Q_n) + \sum_{i=1}^n Q_i(s)\dot{p}_i(s)\right)ds + \sum_{i=1}^n S_{0,i}(p_i,Q_i), \end{aligned} \tag{2.2.7}$$

where the position operators in the momentum representation have been defined as $Q_i \equiv \partial_{p_i}$ with the commutation relation $[Q_i,p_j] = S_{0,i}\delta_{i,j}$. $S_{0,i}(p_i,Q_i)$ corresponds to the action associated with the generating function of the probability distribution function of the initial value of each variable, $X_i(t=0)$, which are assumed to be independent random variables.

The so-called semi-classical approximation consists of approximating the path integral in Eq. (2.2.6) by

$$G(p_1,\ldots,p_n,t) = e^{-S(p_1,\ldots,p_n,t)} \tag{2.2.8}$$

where $p_1(t),\ldots,p_n(t)$ are now the solutions of the Hamilton equations, i.e. the orbits which maximise the action S:

$$\frac{dp_i}{dt} = -\frac{\partial H_k}{\partial Q_i} \tag{2.2.9}$$

$$\frac{dQ_i}{dt} = \frac{\partial H_k}{\partial p_i} \tag{2.2.10}$$

where the pair (Q_i,p_i) are the generalised coordinates corresponding to chemical species $i = 1,\ldots,n$. These equations are (formally) solved with boundary conditions [56] $Q_i(0) = x_i(0)$, $p_i(t) = p_i$, where $x_i(0)p_i(0)$ is the initial number of molecules of species i.

Eqs. (2.2.9)-(2.2.10) are the starting point for the formulation of the semi-classical quasi-steady state approximation (SCQSSA) [4]. In order to proceed further, we assume, as per the Briggs-Haldane treatment of the Michealis-Menten model for enzyme kinetics [29, 123], that the species involved in the system under scrutiny are divided into two groups according to their characteristic scales. More specifically, we have a subset of chemical species whose numbers, X_i, scale as:

$$X_i = \mathcal{S} x_i, \tag{2.2.11}$$

where $x_i = O(1)$, whilst the remaining species are such that their numbers, X_j, scale as:

$$X_j = \mathcal{E} x_j, \tag{2.2.12}$$

where $x_j = O(1)$. Key to our approach is the fact that $\mathcal{S}$ and $\mathcal{E}$ must be such that:

$$\epsilon = \frac{\mathcal{E}}{\mathcal{S}} \ll 1. \tag{2.2.13}$$

We further assume that the generalised coordinates, Q_i, scale in the same fashion as the corresponding variable X_i, i.e.

$$Q_i = \mathcal{S} q_i, \tag{2.2.14}$$

where $q_i = O(1)$. We refer to the variables belonging to this subset as *slow variables*. Similarly,

$$Q_j = \mathcal{E} q_j, \tag{2.2.15}$$

where $q_j = O(1)$, which are referred to as *fast variables*. Moreover, we assume that the moment coordinates, p_i, are all independent of $\mathcal{S}$ and $\mathcal{E}$, and therefore remain invariant under rescaling.

Under this scaling for the generalised coordinates, we define the following scale transformation for the Hamiltonian in Eq. (2.2.7):

$$H_k(p_1, \ldots, p_n, Q_1, \ldots, Q_n) = k_J \mathcal{S}^k \mathcal{E}^l H_\kappa(p_1, \ldots, p_n, q_1, \ldots, q_n) \tag{2.2.16}$$

where J identifies the reaction with the largest order among all the reactions that compose the dynamics and k_J is the corresponding rate constant. For example, in the case of the bistable enzyme-catalysed system whose reactions or elementary events and the corresponding transition rates are given in Table 2.1, $J = 1$, as this reaction is order 3 whereas all the others are order 0, 1, or 2.

The last step is to rescale the time variable so that a dimensionless variable, τ, is defined such that:

$$\tau = k_J \mathcal{S}^{k-1} \mathcal{E}^l t \tag{2.2.17}$$

It is now a trivial exercise to check that, upon rescaling, Eqs. (2.2.9)-(2.2.10) read

$$\frac{dp_i}{d\tau} = -\frac{\partial H_\kappa}{\partial q_i}, \tag{2.2.18}$$

$$\frac{dq_i}{d\tau} = \frac{\partial H_\kappa}{\partial p_i}, \tag{2.2.19}$$

for the slow variables. By contrast, rescaling of the Hamilton equations corresponding to the subset of fast variables leads to:

$$\epsilon \frac{dp_j}{d\tau} = -\frac{\partial H_\kappa}{\partial q_j}, \tag{2.2.20}$$

$$\epsilon \frac{dq_j}{d\tau} = \frac{\partial H_\kappa}{\partial p_j}, \tag{2.2.21}$$

where ϵ is defined in Eq. (2.2.13). The QSS approximation consists on assuming that $\epsilon \frac{dp_j}{d\tau} \simeq 0$ and $\epsilon \frac{dq_j}{d\tau} \simeq 0$ in Eqs. (2.2.20)-(2.2.21),

$$-\frac{\partial H_\kappa}{\partial q_j} = 0, \tag{2.2.22}$$

$$\frac{\partial H_\kappa}{\partial p_j} = 0, \tag{2.2.23}$$

resulting in a differential-algebraic system of equations which provides us with the semi-classical quasi-steady state approximation (SCQSSA).

2.3 Model of the G_1/S transition

We analyse a stochastic system proposed in [4, 89], whose mean-field limit has been shown to correspond to a bistable system which is a part of a model for the G_1/S transition of the eukaryote cell cycle proposed in [224]. Tyson & Novak [224] have formulated a (deterministic) model of the cell cycle such that the core of the system regulating the G_1/S transition is a system of two mutually-repressing proteins (Cdh1 and CycB). This system of mutual repression gives rise to a bistable system where one of the stable steady states is identified with the G_1 phase whereas the other corresponds to a state where the cell is ready to go through the other three phases of the cell-cycle, known as S, G_2, and M. This central module, which is the one we focus on, is acted upon by a complex regulatory network which monitors if conditions are met for the cell to undergo this transition and accounts for its accurate timing. Presently,

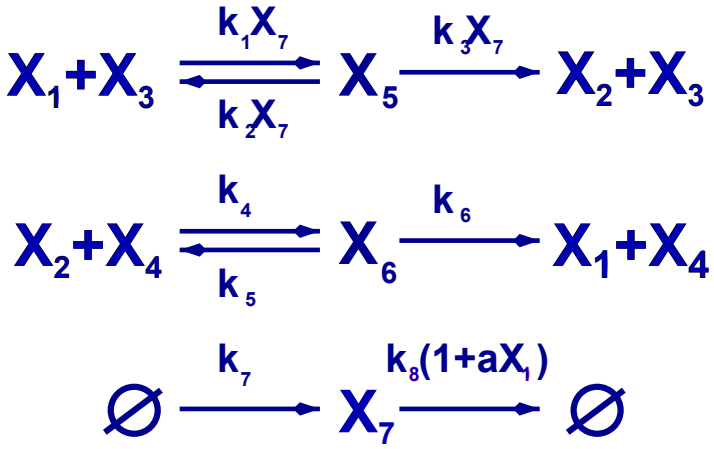

Figure 2.1: Reactions for the bistable enzyme-catalysed system proposed by Tyson & Novak [224]. X_1 represents active Cdh/Apc, X_2 inactive Cdh/Apc, X_3 inactivating enzymes, X_4 activating enzymes, X_5 active Cdh/Apc-inactivating-enzyme complexes, X_6 inactive Cdh/Apc-activating-enzyme complexes, and X_7 the number of CycB-CDK complexes. The first two reactions correspond to enzyme-catalysed activation and inactivation of Cdh/APC. The third reaction corresponds to the dynamics of CycB activity: synthesis at a constant rate, k_7, and degradation by natural decay and active Cdh/Apc-induced inactivation.

we ignore this network and focus on the central bistable system. It is shown in [224] that the mean field version of the model exhibits bistable behaviour as a function of a bifurcation parameter m, i.e. the mass of the cell. For very small values of m, the system is locked into a high (low) Cdh1(CycB)-level stable fixed point (i.e. into the G_1 phase). For very large values m, the system has only one stable steady state corresponding to a low (high) Cdh1(CycB)-level fixed point. For intermediate values of m the system exhibits bistability, i.e. both of these stable fixed points coexist with an unstable saddle point. In this section, we focus on how noise alters the behaviour of the mean-field dynamics.

The transition rates corresponding to the different reactions involved in the stochastic model associated to the enzyme-regulated kinetics shown in Fig. 2.1 are given in Table 2.1. This kinetics corresponds to the enzyme regulated activation and inhibition of Cdh1 (an inhibitor of cell-cycle progression). Cdh1 inactivation is further (up)regulated by the presence of CycB, an activator of cell-cycle progression. CycB is synthesised and degraded at basal rates and is further degraded in the presence of active Cdh1 (see Fig. 2.1). Therefore, the resulting dynamics leads to a system with mutual inhibition which produces bistable behaviour. It is important to note that the associated reaction kinetics exhibits three conservation laws (see Table 2.1): $X_3 + X_5 = e_0$, $X_4 + X_6 = e_0$, and $X_1 + X_2 + X_5 + X_6 = s_0$. The first two of these conservation laws are

Variable	Description
X_1, X_2	Number of active and inactive (respectively) Cdh1 molecules
X_3, X_4	Number of Cdh1-inactivating/activating (respectively) enzyme molecules
X_5, X_6	Number of enzyme-active/enzyme-inactive (respectively) Cdh1 complexes
X_7	Number of active cyclin molecules

Transition rate	r	Event
$W_1(x) = k_1 X_7 X_1 X_3$	$r_1 = (-1, 0, -1, 0, +1, 0, 0)$	Enzyme and active Cdh1 form complex
$W_2(x) = k_2 X_7 X_5$	$r_2 = (+1, 0, +1, 0, -1, 0, 0)$	Enzyme-(active Cdh1) complex splits
$W_3(x) = k_3 X_7 X_5$	$r_3 = (0, +1, +1, 0, -1, 0, 0)$	Inactivation of Cdh1 and enzyme release
$W_4(x) = k_4 X_2 X_4$	$r_4 = (0, -1, 0, -1, 0, +1, 0)$	Enzyme and inactive Cdh1 form complex
$W_5(x) = k_5 X_6$	$r_5 = (0, +1, 0, +1, 0, -1, 0)$	Enzyme-(inactive Cdh1) complex splits
$W_6(x) = k_6 X_6$	$r_6 = (+1, 0, 0, +1, 0, -1, 0)$	Activation of Cdh1 and enzyme release
$W_7(x) = k_7$	$r_7 = (0, 0, 0, 0, 0, 0, +1)$	CycB synthesis
$W_8(x) = k_8(1 + aX_1)X_7$	$r_8 = (0, 0, 0, 0, 0, 0, -1)$	CycB degradation

Table 2.1: Random variables and transition rates of the stochastic model associated to the enzymatic reaction shown in Fig. 2.1.

associated to the conservation of the number of Cdh1-inhibiting and Cdh1-activating enzymes, respectively, whilst the latter expresses the conservation of the total number of Cdh1 molecules. The quantities e_0 and s_0 are the (conserved) number of enzymes and Cdh1, respectively. Note that, as per the methodology developed in Section 2.2, we assume that $s_0 = O(\mathcal{S})$ and $e_0 = O(\mathcal{E})$.

The corresponding stochastic Hamiltonian, H_k, which is derived by applying the methodology of Section 2.2 to the Master Equation associated to the chemical kinetics described in Table 2.1, can be split into three parts,

$$H_k(p_1, \ldots, p_7, Q_1, \ldots, Q_7) = H_A + H_I + H_B, \tag{2.3.1}$$

where H_I is the Hamiltonian corresponding to the CycB-regulated enzymatic inactivation of Cdh1 (reactions 1 to 3 in Table 2.1):

$$H_I(p, Q) = k_4(p_6 - p_2 p_4)Q_2 Q_4 + k_5(p_2 p_4 - p_6)Q_6 + k_6(p_1 p_4 - p_6)Q_6, \tag{2.3.2}$$

H_A corresponds to enzymatic activation of Cdh1 (reactions 4 to 6 in Table 2.1):

Rescaled variables	Dimensionless parameters
$\tau = k_1 \mathcal{E} \mathcal{S} t$	$\epsilon = \mathcal{E}/\mathcal{S}$, $\alpha = a\mathcal{S}$
$q_1 = Q_1/\mathcal{S}$	$\kappa_2 = k_2/(k_1\mathcal{S})$
$q_2 = Q_2/\mathcal{S}$	$\kappa_3 = k_3/(k_1\mathcal{S})$
$q_3 = Q_3/\mathcal{E}$	$\kappa_4 = k_4/(k_1\mathcal{S})$
$q_4 = Q_4/\mathcal{E}$	$\kappa_5 = k_5/(k_1\mathcal{S}^2)$
$q_5 = Q_5/\mathcal{E}$	$\kappa_6 = k_6/(k_1\mathcal{S}^2)$
$q_6 = Q_6/\mathcal{E}$	$\kappa_7 = k_7/(k_1\mathcal{E}\mathcal{S}^2)$
$q_7 = Q_7/\mathcal{S}$	$\kappa_8 = k_8/(k_1\mathcal{E}\mathcal{S})$

Table 2.2: Dimensionless variables used in Eqs. (2.3.7). $\mathcal{S}$ and $\mathcal{E}$ are the average concentration of Cdh1 (active plus inactive) and the average concentration of both Cdh1-activating and Cdh1-inactivating enzymes, respectively. We further assume that the stationary concentration of active CycB also scales with $\mathcal{S}$.

$$H_A(p,Q) = k_1 p_7(p_5 - p_1 p_3)Q_1 Q_3 Q_7 + k_2 p_7(p_1 p_3 - p_5)Q_5 Q_7 + k_3 p_7(p_2 p_3 - p_5)Q_5 Q_7, \tag{2.3.3}$$

and, finally, H_B, which corresponds to synthesis and degradation of CycB, is given by (reactions 7 and 8 in Table 2.1):

$$H_B(p,Q) = k_7(p_7 - 1) + k_8(1 - p_7)Q_7 + k_8 a p_1(1 - p_7)Q_1 Q_7, \tag{2.3.4}$$

where the expressions H_I, H_A and H_B can be obtained by applying (2.2.4).

We now proceed to apply the procedure explained in Section 2.2 in order to obtain the SCQSSA for the system determined by the transition rates given in Table 2.1. We first need to determine which of the variables are slow variables and which ones are fast variables. As shown in Table 2.2, the pairs (p_1, Q_1), (p_2, Q_2), and (p_7, Q_7), corresponding to the active and inactive forms of Cdh1 and to CycB, respectively, are the slow generalised coordinates, as the generalised positions scale with s_0. The remaining generalised coordinates scale as e_0 and, therefore, are fast variables. Furthermore, the rescaled Hamiltonian is given by:

$$H_k(p,Q) = k_1 \mathcal{E} \mathcal{S}^2 H_\kappa(p,q) \tag{2.3.5}$$

where

$$H_\kappa(p,q) = H_{\kappa,A} + H_{\kappa,I} + H_{\kappa,B}, \tag{2.3.6}$$

with

$$H_{\kappa,I} = \kappa_4(p_6 - p_2 p_4)q_2 q_4 + \kappa_5(p_2 p_4 - p_6)q_6 + \kappa_6(p_1 p_4 - p_6)q_6$$

$$H_{\kappa,A} = p_7(p_5 - p_1p_3)q_1q_3q_7 + \kappa_2 p_7(p_1p_3 - p_5)q_5q_7 + \kappa_3 p_7(p_2p_3 - p_5)q_5q_7$$
$$H_{\kappa,B} = \kappa_7(p_7 - 1) + \kappa_8(1 - p_7)q_7 + \kappa_8\alpha p_1(1 - p_7)q_1q_7 \tag{2.3.7}$$

The rescaled parameters κ_i are given in Table 2.2. Last, by rescaling time and defining the dimensionless time variable as $\tau = k_1\mathcal{E}\mathcal{S}t$ (Table 2.2), the SCQSSA equations (2.2.18)-(2.2.19) and (2.2.22)-(2.2.23) lead to (see [4] for a detailed derivation):

$$\frac{dq_1}{d\tau} = p_4 p_{e_4}\frac{\kappa_6 q_2}{q_2 + J_2} - p_7 p_3 p_{e_3}\frac{\kappa_3 q_7 q_1}{q_1 + J_1} + \kappa_8\alpha(1 - p_7)q_7q_1 \tag{2.3.8}$$
$$\frac{dq_2}{d\tau} = -p_4 p_{e_4}\frac{\kappa_6 q_2}{q_2 + J_2} + p_7 p_3 p_{e_3}\frac{\kappa_3 q_7 q_1}{q_1 + J_1} \tag{2.3.9}$$
$$\frac{dq_7}{d\tau} = \kappa_7 - \kappa_8(1 + \alpha p_1 q_1)q_7 \tag{2.3.10}$$
$$p_5 = p_3 p_1 \tag{2.3.11}$$
$$p_6 = p_4 p_2 \tag{2.3.12}$$
$$\frac{dp_7}{d\tau} = -(1 - p_7)\kappa_8(1 + \alpha p_1 q_1) \tag{2.3.13}$$

where $p_1 = p_2$, p_3, and p_4 are constants to be determined and $J_1 = \kappa_2 + \kappa_3$ and $J_2 = \kappa_4^{-1}(\kappa_5 + \kappa_6)$, and $p_{e_3} = e_3/\mathcal{E}$ and $p_{e_4} = e_4/\mathcal{E}$. Note that for $q_1(\tau) + q_2(\tau) = p_c$, with $p_c = s_0/\mathcal{S}$, to hold $p_7 = 1$ must be satisfied. In this case, we have

$$\frac{dq_1}{d\tau} = p_4 p_{e_4}\frac{\kappa_6(p_c - q_1)}{(p_c - q_1) + J_2} - p_3 p_{e_3}\frac{\kappa_3 m q_7 q_1}{q_1 + J_1} \tag{2.3.14}$$
$$\frac{dq_7}{d\tau} = \kappa_7 - \kappa_8(1 + \alpha p_1 q_1)q_7 \tag{2.3.15}$$
$$p_5 = p_3 p_1 \tag{2.3.16}$$
$$p_6 = p_4 p_1 \tag{2.3.17}$$

As shown in [4], the parameter values are determined by comparing the corresponding mean-field approximation, which is obtained by taking $p_i = 1$ [56], and $p_c = p_{e_3} = p_{e_4} = 1$, i.e. the total number of molecules of Cdh1 and its activating and inhibiting enzymes be exactly equal to its average, i.e. $s_0 = \mathcal{S}$ and $e_3 = e_4 = \mathcal{E}$, to the system originally proposed by Tyson & Novak [224]. In Eq. (2.3.14) we have redefined $\kappa_3 \to \kappa_3 m$ in order to make explicit the dependence on the bifurcation parameter, m, as used by Tyson & Novak [224]. The parameter values are shown in Table 2.3.

Upon rescaling of the variables (Table 2.2) and the Hamiltonian (Eq. (2.2.16)), the action functional reads:

$$S(p,q) = s_0\int_0^\tau \left(-H_\kappa(p,q) - \sum_{slow} q_i\frac{dp_i}{ds} - \sum_{fast} q_j\epsilon\frac{dp_j}{ds}\right)ds + \sum_i^n S_{0,i}(p_i) \tag{2.3.18}$$

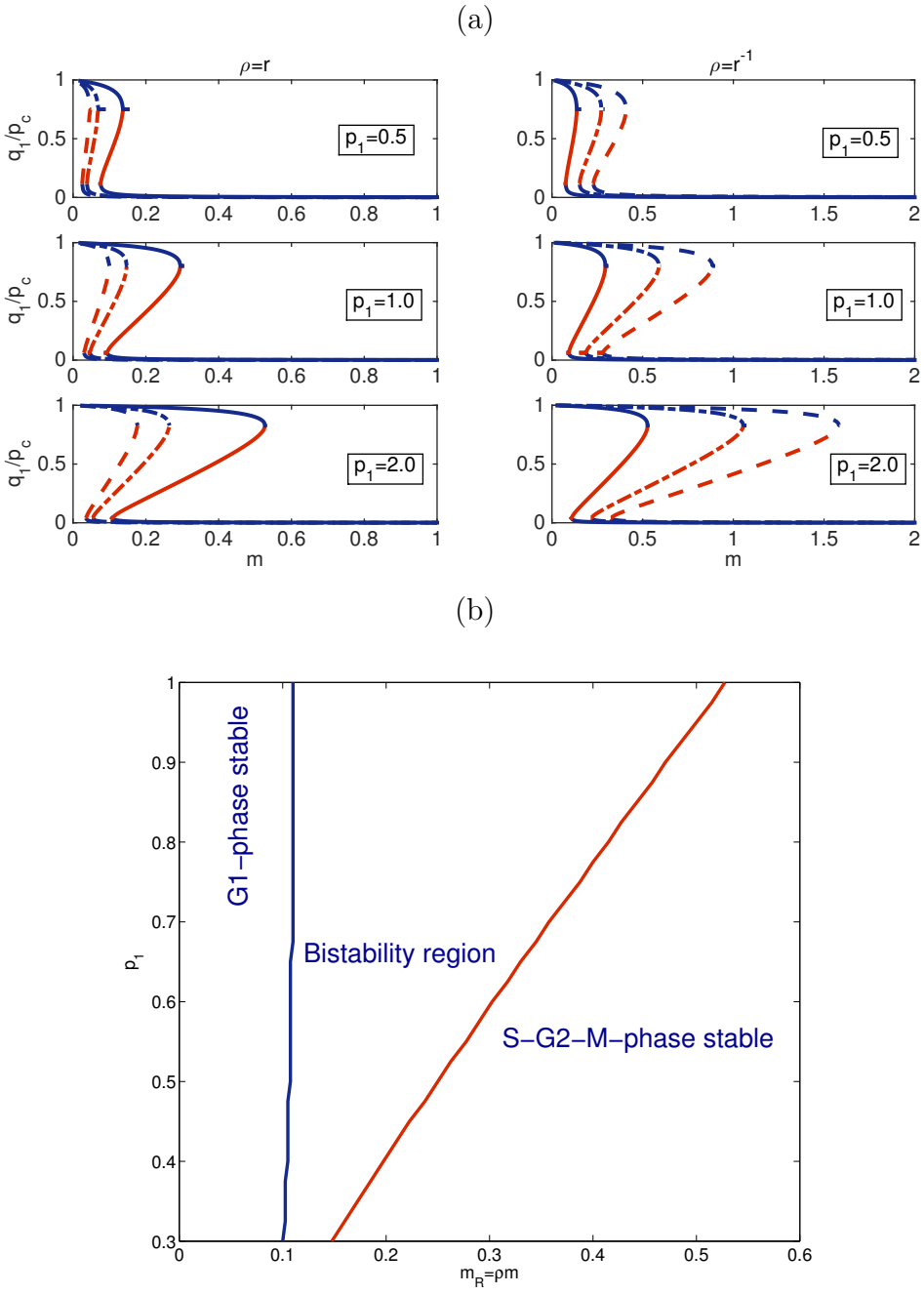

Figure 2.2: Bifurcation analysis for the SCQSSA of Eqs. (2.3.14)-(2.3.17). The panels on the top plot (a) shows the bifurcation diagrams for different values of the parameters p_1, $p_c = p_1$ and $\rho = \frac{p_3 p_{e_3}}{p_4 p_{e_4}}$. If e_0 and s_0 are random Poisson variables with parameter $\mathcal{S}$ and $\mathcal{E}$, respectively, then $\rho = \frac{p_3^2}{p_4^2}$ (see Eq. 2.3.23). Solid lines correspond to $r = 1$, dot-dashed lines to $r = 2$, and dashed lines to $r = 3$. The bottom plot (b) shows the bistability boundaries in $p_1 - m_R$ parameter space. The region between the boundaries corresponds to the bistable region of the stochastic system according to the SCQSSA.

Rescaled parameter	Parameter	Units	Reference
$\kappa_2 = J_4 - \kappa_3$	$a_1' = 0.04$	min^{-1}	[224]
$\kappa_3 m = \frac{a_4 m}{k_1 \mathcal{E} \mathcal{S}}$	$a_2' = 0.04$	min^{-1}	[224]
$\kappa_6 = \frac{a_3'}{k_1 \mathcal{E} \mathcal{S}}$	$a_2'' = 1$	min^{-1}	[224]
$\kappa_5 = \kappa_4 J_3 - \kappa_6$	$a_3 = 1$	min^{-1}	[224]
$\kappa_7 = \frac{a_1'}{k_1 \mathcal{E} \mathcal{S}}$	$a_4 = 35$	min^{-1}	[224]
$\kappa_8 = \frac{a_2'}{k_1 \mathcal{E} \mathcal{S}}$	$m = 0.3$	Dimensionless	–
$a = \frac{a_2''}{k_1 \mathcal{E} \mathcal{S} \kappa_8}$	$\mathcal{E} = 4$	Dimensionless	[4]
	$\mathcal{S} = 400$	Dimensionless	[4]
	$k_1 = 1$	min^{-1}	[183]
	$\kappa_4 = \kappa_3$	Dimensionless	[4]
	$J_3 = J_4 = 0.04$	Dimensionless	[224]

Table 2.3: Parameter values used in simulations of the stochastic bistable enzyme-catalysed system

It is straightforward to check that in SCQSSA conditions $H_\kappa(p, q) = 0$. Furthermore, since $p_1 = p_2 =$const. and $p_7 = 1$, and $\epsilon \dot{p_j} \simeq 0$ for the fast generalised coordinates, the SCQSS approximation of the action Eq. (2.3.18), S_{QSS}, reduces to:

$$S_{QSS}(p) = \sum_{i=1}^{n} S_{0,i}(p_i) \tag{2.3.19}$$

where, as per the SCQSSA, p_5 and p_6 are determined by Eqs. (2.3.16) and (2.3.17), respectively, $p_7 = 1$, which implies $S_{0,7}(p_7) = 0$, and $p_1 = p_2$, p_3 and p_4 are constants that remain to be determined. In order to do so, we resort to the method developed in reference [4]. The quasi-steady state characteristic function, $G_{QSS}(p, \tau)$ is given by:

$$G_{QSS}(p, \tau) = e^{\left(-\sum_{i=1}^{6} S_{0,i}(p_i)\right)} = \prod_{i=1}^{6} G_{0,i}(p_i) \tag{2.3.20}$$

where $G_{0,i}(p_i) = e^{-S_{0,i}(p_i)}$ is the generating function of the probability distribution for the initial condition of species X_i $i = 1, \ldots, 6$. In [4], we have shown that, applying a Laplace-type asymptotic method [1, 158] to the integrals

$$\begin{aligned} P(X_1(\tau = 0) = s_0) &= \frac{1}{2\pi i} \oint_C \frac{G_{0,1}(p_1)}{p_1^{s_0+1}} dp_1 = \frac{1}{2\pi i} \oint_C \frac{e^{-(S_{0,1}(p_1) + s_0 \log p_1)}}{p_1} dp_1, \\ P(X_i(\tau = 0) = e_i) &= \frac{1}{2\pi i} \oint_C \frac{e^{-(S_{0,i}(p_i) + e_0 \log p_i)}}{p_i} dp_i \text{ with } i = 3, 4 \end{aligned} \tag{2.3.21}$$

where, $p_1 = p_2$, p_3 and p_4 can be given as functions of s_0 and e_i, $i = 3, 4$, i.e. the initial numbers of Cdh1 molecules and Cdh1-inactivating and Cdh1-activating enzymes, respectively:

$$\begin{aligned} -p_1 \frac{dS_{0,1}}{dp_1} &= s_0 \\ -p_i \frac{dS_{0,i}}{dp_i} &= e_i \text{ for } i = 3, 4 \end{aligned} \tag{2.3.22}$$

$P(X_1(\tau = 0) = s_0)$, $P(X_3(\tau = 0) = e_3)$ and $P(X_4(\tau = 0) = e_4)$ are the probabilities that X_1 initially takes the value $X_1(\tau = 0) = s_0$ and that X_3 and X_4 have initial values $X_3(\tau = 0) = e_3$ and $X_4(\tau = 0) = e_4$. These probabilities can be interpreted to correspond to variability in the abundance of these enzymes within a population of cells. A particularly simple case results from assuming that $P(X_1(\tau = 0) = s_0)$, $P(X_3(\tau = 0) = e_3)$ and $P(X_4(\tau = 0) = e_0)$ are Poisson distributions with parameter $\mathcal{S}$ and $\mathcal{E}$, respectively. In this case [4]:

$$\begin{aligned} p_1 &= \frac{s_0}{\mathcal{S}} \\ p_3 &= \frac{e_3}{\mathcal{E}} \\ p_4 &= \frac{e_4}{\mathcal{E}} \end{aligned} \tag{2.3.23}$$

Note that, in the particular case in which the total numbers of Cdh1 and enzyme molecules are random Poisson variables, we have that $p_1 = p_c$, $p_3 = p_{e_3}$, and $p_4 = p_{e_4}$.

2.3.1 Bifurcation analysis

Fig. 2.2 shows results regarding the bifurcation behaviour of the SCQSS approximation of the stochastic bistable enzyme-catalysed system Eqs. (2.3.14)-(2.3.17). In particular we are interested in a comparison between the bistable behaviour of the mean-field model, corresponding to taking $p_i = 1$ for all i, and that of the SCQSS approximation with p_1, p_3 and p_4 given by Eq. (2.3.22). i.e. they are determined as functions of s_0 and e_0.

We have shown that both the ratio of p_3 and p_4, $\rho = \frac{p_3 p_{e_3}}{p_4 p_{e_4}} = \frac{p_3^2}{p_4^2} = \frac{e_3^2}{e_4^2}$, and p_1 alter the bistable behaviour of the system beyond the predictions of the mean-field model. In particular, we observe that decreasing the value of ρ extends the region of stability of the G_1-fixed point, i.e. the fixed point corresponding to the steady-state value of q_1, such that $q_1 \sim 1$. By contrast, when ρ is increased the stability region of the G_1-fixed point shrinks. Intuitively, given the relation between p_3 and p_4 and the number of Cdh1-inactivating and Cdh1-activating enzyme, this result is straightforward to interpret: decreasing the number of Cdh1-inactivating enzyme demands a

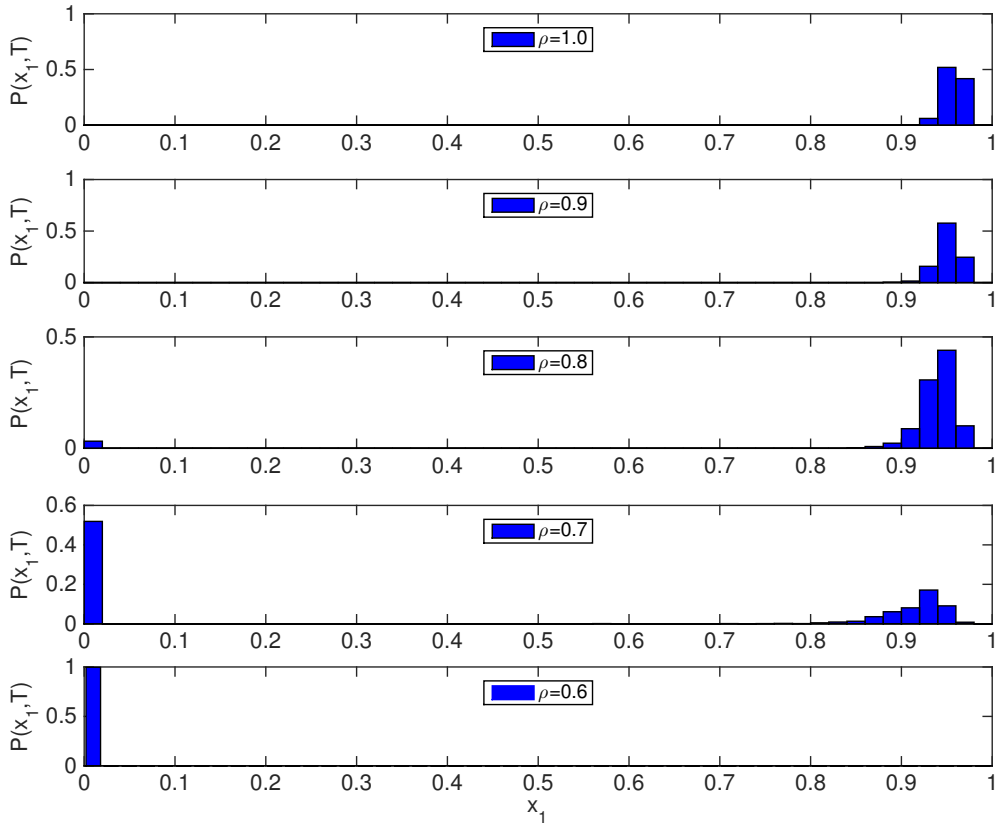

Figure 2.3: Simulation results for the stochastic bistable enzyme-catalysed system Table 2.1. We have plotted the probability $P(x_1, T) = \text{Prob}(x_1(\tau = T))$ where $x_1 = X_1/\mathcal{S}$ and $T = 100$ for different values of ρ. The initial number of Cdh1-inactivating and Cdh1-activating enzymes are fixed according to $X_3(t = 0) = \frac{e_0}{\rho}$ and $X_4(t = 0) = e_0$, respectively. $m = 0.3$. We aim to check our predictions regarding the effect of the ratio $\rho = p_3^2/p_4^2 = e_3^2/e_4^2$ on the stability properties of the system. According to our results shown in Fig. 2.2, decreasing the ratio between the number of Cdh1-inactivating (e_4) and Cdh1-activating (e_3) enzymes, the system should be driven away from bistability and into the stable G_1-phase regime (see Fig. 2.2(b)). The remaining parameter values are inferred from those given by Tyson & Novak [224] as shown in Tables 2.2 and 2.3. We see that when varying ρ, the system switches from a state of high x_1 ($\rho \geq 0.9$) to a state of low x_1 ($\rho \leq 0.6$), whereas at the intermediate levels of (e.g. $\rho = 0.7$ and $\rho = 0.8$) the system is in a bistable state. We take $p_1 = p_c = 1$ in all the simulations shown in this figure. Average is performed over 1000 realisations.

larger value of m in order to de-stabilise the G_1-fixed point. This is fully confirmed by direct simulation using Gillespie stochastic simulation algorithm [76]. Fig. 2.3 shows simulation results in which we compute the probability $P(x_1, T) = \text{Prob}(x_1(\tau = T))$ for different values of $\rho \leq 1$. T has been chosen so that the system has reached steady state conditions. We observe, that for $\rho = 1$ and $m = 0.3$, the system evolves towards the $q_1 \ll 1$-fixed point (i.e. the S-G_2-M fixed point). As ρ decreases, i.e. there is more Cdh1-inactivating enzyme than Cdh1-activating enzyme, the system enters the bistable regime. If ρ reaches low-enough values (depending upon the initial condition), we may even observe an exchange of stability, i.e. the system evolves towards the $q_1 \sim 1$-fixed point.

Regarding the dependence on p_1, we have checked the predictions of the SCQSS approximation by means of simulations with different values of s_0. Figure 2.2 shows the bi-stability region of system Eqs. (2.3.14)-(2.3.17) in $p_1 - m_R$-space, where $m_R = \rho m$. For a fixed value of m_R, there is a threshold value for p_1 below which the system stops being bistable to become entrapped into the the S-G_2-M fixed point (i.e. $q_1 \ll 1$). In order to validate this prediction, we have conducted stochastic simulations for different values of s_0. Figure 2.4 shows simulation results for $P(x_1, T) = \text{Prob}(x_1(\tau = T))$. We observe that for small values of s_0, the system is locked into the the S-G_2-M fixed point, as predicted by the SCQSS approximation. As s_0 increases, the system enters a fluctuation-dominated bistable regime where, as the system goes through the bifurcation point, the system undergoes bistable behaviour. This behaviour is typical in a system undergoing a phase transition, where fluctuations unboundedly increase [84]. Finally, as s_0 continues to increase, the system becomes trapped into G_1-fixed point (see Figure 2.4). These results fully reproduce the behaviour predicted by our SCQSSA stability analysis.

The aforementioned behaviour regarding unbounded increase of fluctuations close to a bifurcation [84] is used to locate the critical value of the associated control parameter, i.e. ρ and p_c for the simulations shown in Figs. 2.3 and 2.4, respectively. This property allows us to do a quantitative comparison between the simulations and asymptotic analysis. To this end, we plot how the variance, $\sigma^2 = \langle (x_1 - \langle x_1 \rangle)^2 \rangle$ where $x_1 = X_1(\tau = T)/S$, changes as the corresponding control parameter varies. Regarding the results shown in Fig. 2.5(a) (associated to the simulations shown in Fig. 2.3), we observe that the critical value of the control parameter ρ, ρ_B, is approximately $\rho_B \simeq 0.7$, which, taking into account that $m = 0.3$, implies that the critical value of the renormalised mass, $m_R = \rho m$, $m_B = \rho_B m \simeq 0.21$. Our asymptotic analysis predicts that $m_B = 0.11$ (see Fig. 2.2(b) with $p_c = 1$). The results shown in in Fig. 2.5(b) (corresponding to the simulations shown in Fig. 2.4), the critical value of p_c, p_B, is approximately $p_B \simeq 0.7$. The prediction of our asymptotic analysis (see Fig. 2.2(b) with $\rho = 1$) is $p_B = 0.6$.

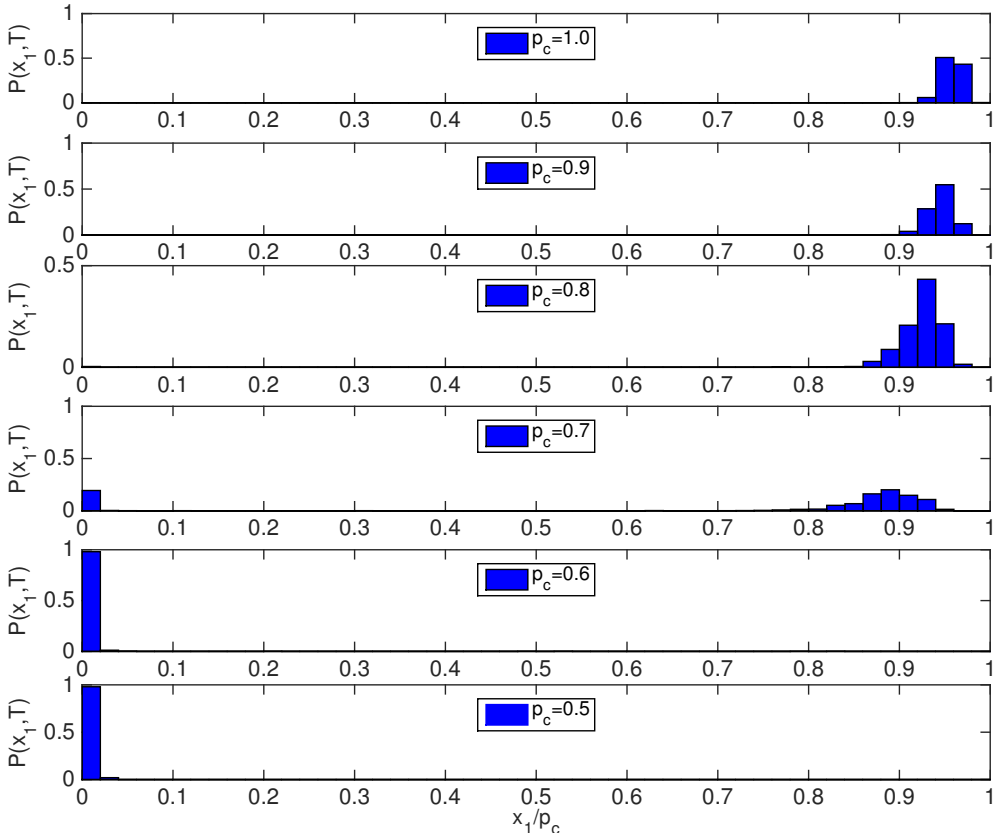

Figure 2.4: Simulation results for the stochastic bistable enzyme-catalysed system Table 2.1. We have plotted the probability $P(x_1, T) = \text{Prob}(x_1(\tau = T))$ where $x_1 = X_1/\mathcal{S}$ and $T = 100$ with different initial conditions and different values of p_c. Average is performed over 1000 realisations. $m = 0.3$ and $X_3(t = 0) = e_0$ and $X_4(t = 0) = e_0$. The remaining parameter values are inferred from those given by Tyson & Novak [224] as shown in Tables 2.2 and 2.3. We see that when varying p_c, the system switches from a state of high x_1 ($p_c \geq 0.8$) to a state of low x_1 ($p_c \leq 0.6$), whereas at the intermediate levels of $p_c = 0.7$ the system is in a bistable state.

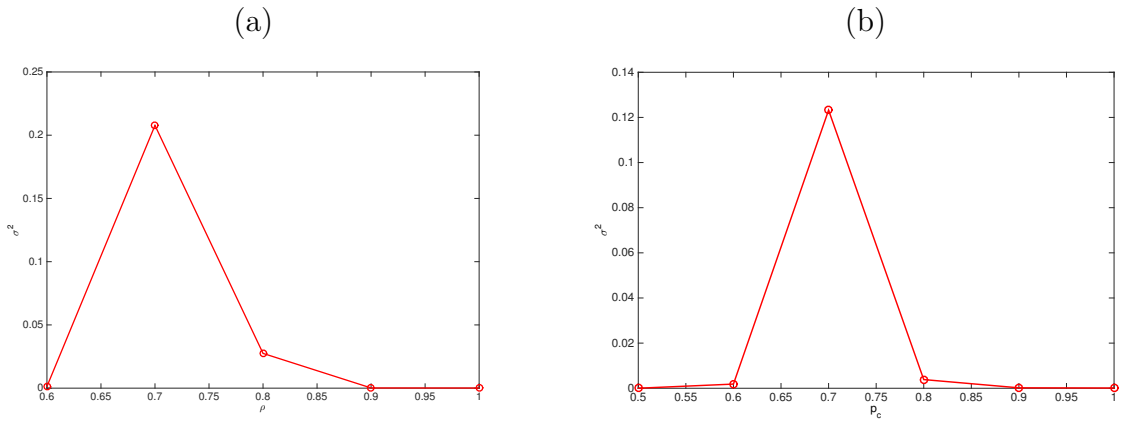

Figure 2.5: Plots showing the variance $\sigma^2 = \langle (x_1 - \langle x_1 \rangle)^2 \rangle$ where $x_1 = X_1(\tau = T)/S$ associated to the simulation results shown in Fig. 2.3 (panel (a)) and in Fig. 2.4 (panel (b)). These plots show how σ^2 changes as the control parameter (ρ, for the simulations associated to plot (a), and p_c for the simulations shown in plot (b)). The maximum of σ^2 as a function of the control parameter helps us to quantitatively determine the corresponding critical value [84].

Chapter 3

Minimum Action Path theory of stochastic biochemical transitions out of oscillatory cellular states

3.1 Introduction

As discussed in chapter 2, cells are intrinsically noisy. Such stochasticity arises not only from the production and degradation of cellular components, but also from their mutual interaction or even the interaction with other cells. Nevertheless, some cellular processes require a precise deterministic output, and noise-suppression mechanisms are necessary within the cell [118, 125, 146, 151, 182]. On the other hand, since fluctuations are an intrinsic component of cellular dynamics, mechanisms are in place that cells exploit to improve its function [35, 55]. For example, randomness can enhance the ability of cells to adapt and increase their fitness in random variable environments [2, 90, 138], or to sustain phenotypic variation [16, 146, 148, 151, 182].

Mean-field descriptions of biochemical processes can be analyzed using dynamical systems theory [47], where stable steady states, sustained oscillations or even transients of the ODEs correspond to different possible cellular states [114, 225]. Relevant examples including sustained oscillations are circadian rhythms [82, 143, 204], cAMP oscillations in *Dictyostelium* [83], cell-cycle regulation [71, 72, 73], or patterns of bursting in neuronal activity [23, 48, 157, 212, 220].

When molecular populations are small, the mean-field framework is inaccurate and a stochastic description is required. This involves the formulation of the Master Equation (ME) describing the underlying multivariate biochemical birth-death process [12]. Unfortunately the ME is rarely solvable analytically, requiring the use of Monte Carlo methods (such as the Gillespie algorithm [77]). These numerical methods are often computationally costly and in usually infeasible [36, 37]. This is especially true in

phenomena associated with rare fluctuations, as in the noise-induced escape from a basin of attraction. In these escape problems, approximations such as the Langevin equation [78, 120] or extreme event theory become necessary [175, 217]. In spite of the importance of oscillatory phenomena in biology, most studies have tackled escape problems from point attractors, and a general theory of escape from stable limit cycles is lacking. In order to fill this gap, we consider a simplified oscillatory kinetic model and unveil the ability of the Minimum Action Path (MAP) method from large deviation theory [63, 228], which specifies the most probable path between attractors and the mean escape time by minimization of an action functional.

3.2 The model

In order to study the limit cycle-fixed point transition we construct a generic tunable dynamical landscape and then derive the underlying kinetic reactions. This approach allows for a thorough analysis of the escape problem when changing key parameters, such as the angular velocity along the stable limit cycle or the distance between the fixed point and the stable limit cycle.

We construct this prototypical two-dimensional dynamical system, for species X and Y, such that there is a single stable fixed point at (x_c, y_c), and a stable limit cycle of radius c centered at the fixed point (see Fig.3.1). In order to determine the basins of attraction, we include an elliptical repulser, $E(x,y) \equiv 1 - \frac{(x-x_c-x_0)^2}{a^2} - \frac{(y-y_c)^2}{b^2} = 0$, separating the stable limit cycle from the fixed point. The evolution of the system is given by:

$$\dot{r} = r(r^2 - c^2)E(x,y), \qquad \dot{\theta} = \omega, \tag{3.2.1}$$

where $r \equiv \sqrt{(x-x_c)^2 + (y-y_c)^2}$ is the distance from the fixed point, and θ is the corresponding angular coordinate, $\tan\theta \equiv (y-y_c)/(x-x_c)$, and ω is the angular velocity. Trajectories are either attracted to the fixed point or to the limit cycle, with the exception of points lying on an unstable limit cycle, which remain on that orbit. It is important to note that the unstable limit cycle is not the same as the repulser.

3.3 Stochastic description

To formulate a stochastic system whose mean-field behavior is given by Eqs. (3.2.1), we must derive a compatible set of biochemical reactions. Considering four reactions, each species being produced and degraded, the reaction rates are obtained by splitting the rhs of Eq. (3.2.1) into positive and negative contributions:

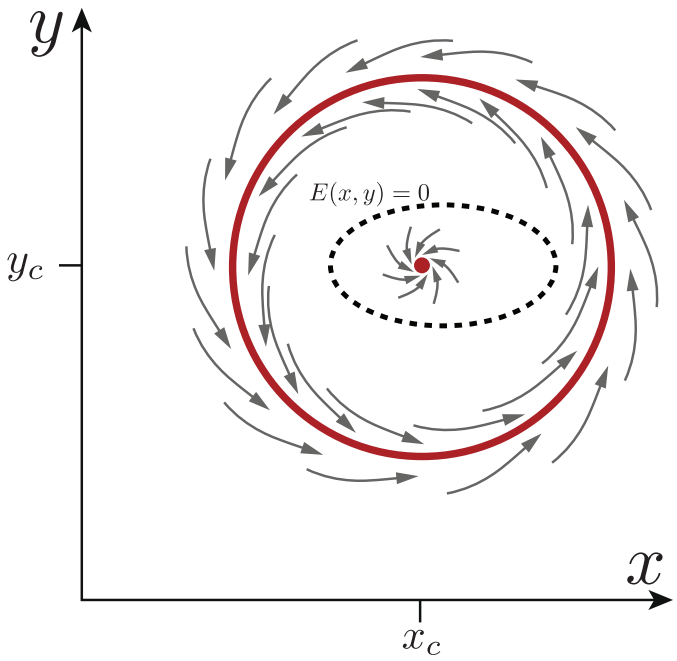

Figure 3.1: Dynamical landscape of the model. Stable limit cycle and fixed point are shown in red. Dashed line indicates the repulser $E(x,y)=0$.

$$\begin{aligned}\dot{x} &= \rho_x^+(x,y) - \rho_x^-(x,y),\\ \dot{y} &= \rho_y^+(x,y) - \rho_y^-(x,y),\end{aligned} \tag{3.3.1}$$

where:

$$\begin{aligned}\rho_x^+ = &\ r^2\left(x + x_c(1-E)\right) + c^2(x_c + x(1-E)) + \omega y_c,\\ \rho_x^- = &\ r^2\left(x_c + x(1-E)\right) + c^2(x + x_c(1-E)) + \omega y,\\ \rho_y^+ = &\ r^2\left(y + y_c(1-E)\right) + c^2(y_c + y(1-E)) + \omega x,\\ \rho_y^- = &\ r^2\left(y_c + y(1-E)\right) + c^2(y + y_c(1-E)) + \omega x_c.\end{aligned} \tag{3.3.2}$$

Identifying $\rho_x^\pm$ and $\rho_y^\pm$ with the rates of the biochemical reactions, the deterministic system Eq. (3.3.1) corresponds to the macroscopic limit of the set of kinetic reactions:

$$\varnothing \xrightarrow{\Omega\rho_x^+} X, \quad X \xrightarrow{\rho_x^-/x} \varnothing, \quad \varnothing \xrightarrow{\Omega\rho_y^+} Y, \quad Y \xrightarrow{\rho_y^-/y} \varnothing, \tag{3.3.3}$$

where the system size, Ω, relates the concentrations x and y with the numbers of molecules of each species, $X = x\Omega$ and $Y = y\Omega$. Reactions (3.3.3) describe a multivariate birth-death process that can be solved numerically using the Gillespie algorithm [77]. As Ω grows, the intrinsic noise is reduced, recovering the mean-field limit (3.2.1) when $\Omega \to \infty$. For large (but finite) Ω, the Master Equation can be approximated by the Chemical Langevin Equation (CLE) [78],

$$\begin{aligned}\dot{x} &= \rho_x^+ - \rho_x^- + \Omega^{-1/2}\sqrt{\rho_x^+ + \rho_x^-}\xi_x(t),\\ \dot{y} &= \rho_y^+ - \rho_y^- + \Omega^{-1/2}\sqrt{\rho_y^+ + \rho_y^-}\xi_y(t),\end{aligned} \tag{3.3.4}$$

where $\xi_x(t)$ and $\xi_y(t)$ are uncorrelated white Gaussian noises, of zero mean, and autocorrelation $\langle \xi_x(t)\xi_x(t')\rangle = \langle \xi_y(t)\xi_y(t')\rangle = \delta(t-t')$. Within this formulation Ω contributes only to the stochastic terms of the CLE (3.3.4). Therefore tuning the value of Ω allows us to investigate the role of fluctuations in the transition between the stable limit cycle and the fixed point.

3.4 Minimum Action Path

The intrinsic noise described in the previous section allows for transitions between the limit cycle and the fixed point. Such transitions can occur through many possible transient trajectories, $\varphi(x(t), y(t))$. Nevertheless, not all the transitions are equally probable. In particular, for reaction systems, unlikely transitions decay exponentially with Ω, $\mathcal{P} \sim \mathrm{e}^{-\Omega \mathcal{S}(\varphi)}$ [120, 217]. Where the decay rate $\mathcal{S}(\varphi)$ is the so-called action of the transition. This means that for large enough values of Ω, the stochastic transition will concentrate along the path, φ^*, which minimizes the action:

$$\mathcal{S} \equiv \mathcal{S}(\varphi^*) = \min_{\varphi} \mathcal{S}(\varphi). \tag{3.4.1}$$

For the n-dimensional stochastic differential equation $\dot{\varphi} = f(\varphi) + g(\varphi)\Omega^{-\frac{1}{2}}\xi(t)$, the action for any path φ_τ of duration τ is given by the Freidlin-Wentzell functional [63]:

$$\mathcal{S}(\varphi_\tau) = \frac{1}{2}\int_0^\tau \|\dot{\varphi}_\tau(t) - f(\varphi_\tau(t))\|^2_{g(\varphi_\tau(t))}\,\mathrm{d}t, \tag{3.4.2}$$

where $f(\varphi_\tau)$ is the deterministic field describing the dynamical system, given for our system by the rhs of Eq. (3.3.1):

$$\begin{pmatrix} f_x(x,y) \\ f_y(x,y) \end{pmatrix} = \begin{pmatrix} \rho_x^+(x,y) - \rho_x^-(x,y) \\ \rho_y^+(x,y) - \rho_y^-(x,y) \end{pmatrix} \tag{3.4.3}$$

The multiplicative noise appears in the norm $\|\bullet\|^2_{g(\varphi_\tau)}$, corresponding with the inner product $\left\langle \bullet, \left(g(\varphi_\tau)g(\varphi_\tau)^\top\right)^{-1} \bullet \right\rangle$, where $g(\varphi_\tau)g^\top(\varphi_\tau) \equiv D$ is the diffusion matrix. Here D takes the form:

$$D(x,y) = \begin{pmatrix} \rho_x^+ + \rho_x^- & 0 \\ 0 & \rho_y^+ + \rho_y^- \end{pmatrix} \tag{3.4.4}$$

Interestingly, the action and, consequently, the most probable path, are independent of Ω. Additionally, the mean first passage time (MFPT) T from one attractor to the

other can be expressed as [63, 217]:

$$T \simeq C\mathrm{e}^{\Omega \mathcal{S}}. \tag{3.4.5}$$

In order to find numerically the path minimizing $\mathcal{S}(\varphi_\tau)$, each path of duration τ was divided into a chain of N segments with initial and final points in the relevant attractors. This reduces finding the optimal path to a minimization problem with $2(N-2)$ degrees of freedom. This was solved using the Broyden-Fletcher-Goldfarb-Shanno algorithm [61, 65], using the analytical expression for the gradient of the action in any of the $2(N-2)$ dimensions [175] (see appendix A for further details).

3.5 Results.

To assess whether MAP theory can characterise the escape from a stable limit cycle, we have divided the analysis into two sections. First, we compare the MAP with paths obtained numerically from the Master Equation and the CLE. In the second section, we compare MAP predictions of the MFPT with those derived from CLE numerical solutions.

3.5.1 The MAP predicts average stochastic escape trajectories.

The MAP defines the most probable transient molecular concentrations during the escape from the stable limit cycle at low noise. Direct comparison of the MAP with trajectories obtained from numerical integration of the CLE or Gillespie simulations shows good agreement for $\Omega \geq 150$ (Fig. 3.2). This reveals that, as Ω increases, the stochastic escape trajectories converge to the MAP. Stochastic simulations for $\Omega < 100$ reveal that, when the number of molecular species is low, oscillations have poor quality, and escape trajectories do not concentrate around a single path (data not shown). In addition, our simulations show that the MAP recapitulates changes in escape trajectory with the angular velocity ω (Fig. 3.2).

A more detailed comparison between stochastic simulations and MAP theory reveals that the prediction of the latter becomes less accurate close to the exit point from the cycle. The discrepancy originates in a fraction of trajectories following the limit cycle for a bit longer before starting the transition (Fig. 3.2). This results in the prediction of a smaller exit angle than the actual average exit angle (Fig. 3.3). To gain deeper understanding into the origin and magnitude of the discrepancy, we computed the angular probability distribution along the cycle, and the probability distribution of the escape angle from a thin annulus around the limit cycle (Fig. 3.3). The latter has been proposed in [102] as a quantity that characterises escape from a stable limit cycle in the low noise limit. Strikingly, our analysis shows that neither measure is as informative as the MAP regarding the escape angle. These results suggest that, even

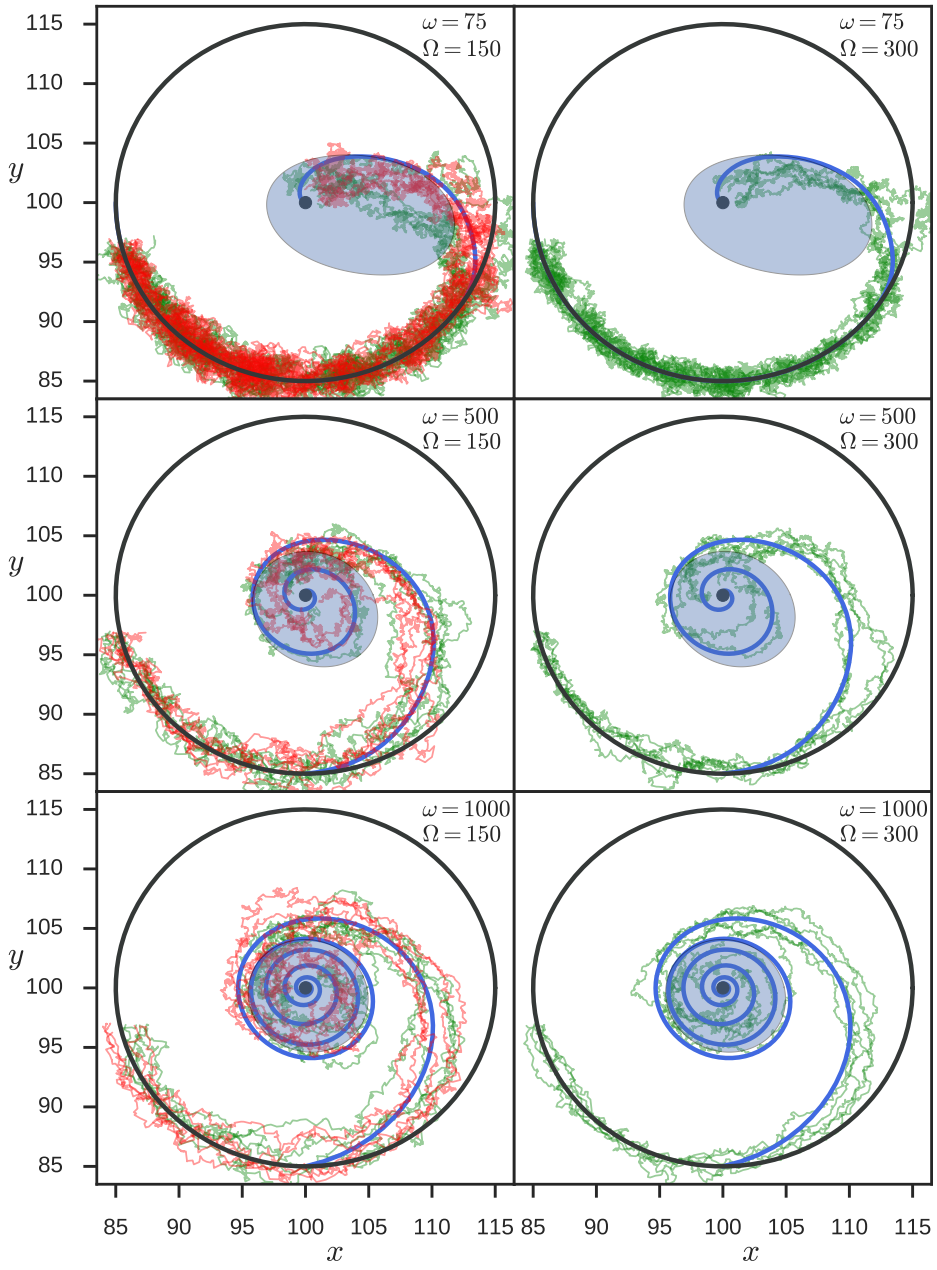

Figure 3.2: Comparison of escape trajectories from the limit cycle to the stable fixed point. Results show 5 trajectories of the CLE (*green*) compared with the MAP (*blue*) for different values of ω and Ω. For $\Omega = 150$, results are also compared with 5 Gillespie trajectories (*red*). The unstable limit cycle separating the basins of attraction (*shaded area*) is found by temporal inversion of eq. (3.3.1). For the sake of clarity, only the last turn of each trajectory prior to escape is shown. The rest of the parameters are x_c=100, y_c=100, $x_0 = 5$, $a = 8$, $b = 5$, $c = 15$.

for a simple dynamical system, knowledge of the whole dynamical landscape is required to predict the exit angle from a stable limit cycle, since the purely local analysis around the stable limit cycle does not produce accurate predictions. In this respect, the MAP proves to be useful, since action minimization takes place along the whole escape trajectory.

Localised inaccuracies in the MAP prediction suggest a highly heterogeneous contribution to the action along the MAP. In order to study this, we have evaluated the density of the action along the MAP, i.e. the Lagrangian of the system. Results show that the density is highest in the middle of the MAP (Fig. 3.3), becoming negligible close to the stable and unstable limit cycles, where, in addition, the MAP is tangent to both limit cycles. This leads to the discrepancy observed in the exit angles. Note that the portion of the MAP inside the basin of attraction of the stable node does not contribute to the action functional since it corresponds with the deterministic trajectory ($\dot{\varphi} = f(\varphi(t))$).

In usual escape problems, the path crosses from one basin of attraction to the other at the saddle point of the deterministic system. Here the boundary between basins of attraction is the unstable limit cycle, so the crossing point cannot be identified by a simple local stability analysis. This again shows the predictive power of the MAP approach.

3.5.2 Minimum action path theory predicts MFPT for escape from the cycle.

Besides the optimal path, we are also interested in testing the ability of MAP theory to predict the MFPT to exit the basin of attraction. Eq. (3.4.5) shows that this can be achieved to logarithmic precision, up to a constant, C. When the basins of attraction are separated by a saddle point, C can be determined by a Jacobian computed at the saddle [25]. However, in the current case, the separatrix is an unstable limit cycle and C must be computed numerically by solving the CLE at low Ω. It can then be used to predict MFPT for larger Ω, where numerical integration of the CLE is computationally costly. Our results show that the minimum action theory allows us to capture the MFPT dependence on model parameters (Fig. 3.4). In our model, we observe an increase in the MFPT with ω. In fact, C also depends non-monotonically on ω (see Fig. 3.4). Nevertheless, as Ω grows, the contribution of the prefactor becomes less important ($\ln T \approx \Omega\mathcal{S} + \ln C$), and the minimum action dominates the escape time estimate.

In addition to the MFPT, we are interested in finding the probability distribution of escape times from the stable limit cycle. Assuming that escape is a rare event focused around a certain exit angle, the escape problem can be described as a Bernoulli process with low success probability p taking place every period of the cycle $\tau = 2\pi/\omega$, at times

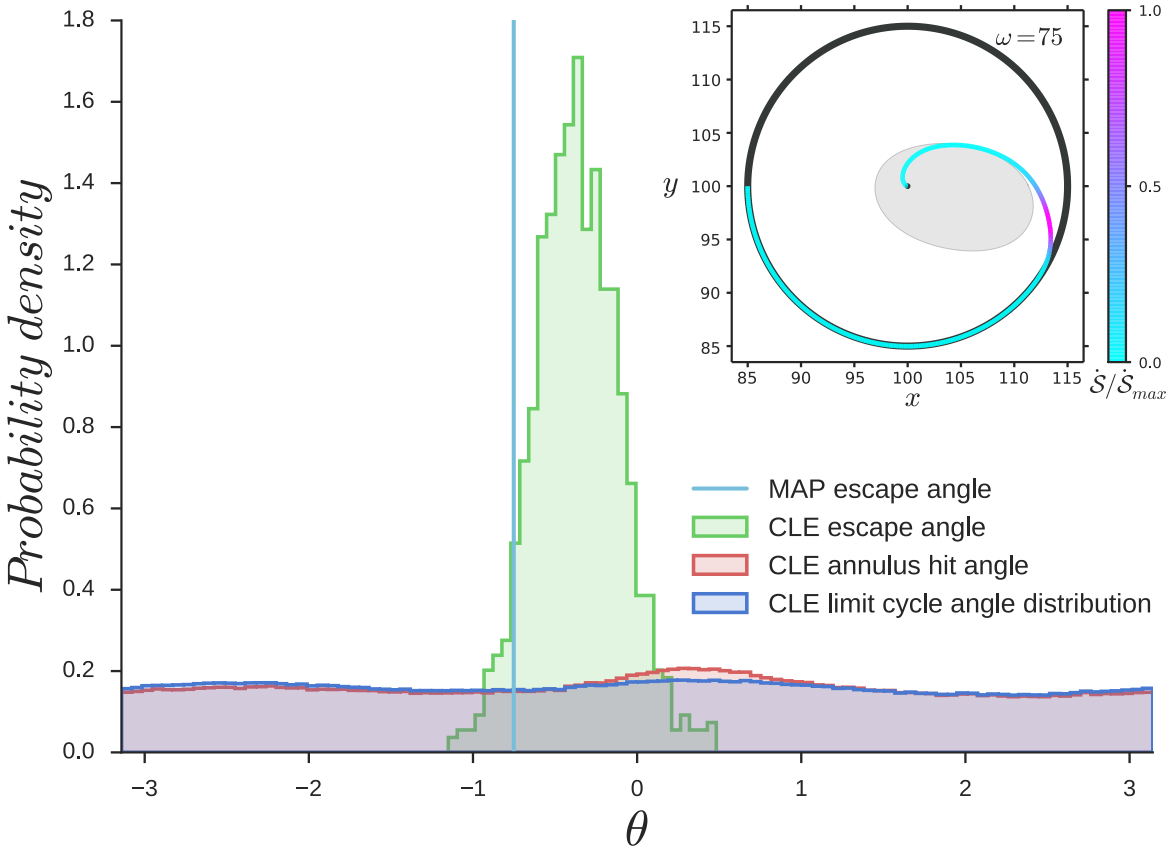

Figure 3.3: Comparison of the escape angle distribution from the limit cycle (*green*) with the escape angle predicted by the MAP (*cyan line*) for $\omega = 75$ and $\Omega = 150$. The results are also compared with the distribution of escape angles from an annulus of radius 0.001 around the limit cycle (*red*), and the angular distribution along the limit cycle, i.e. before escape, (*dark blue*). Inset: Action density (Lagrangian) along MAP normalized to the maximum density. Other parameters are the same as those of Fig. 3.2.

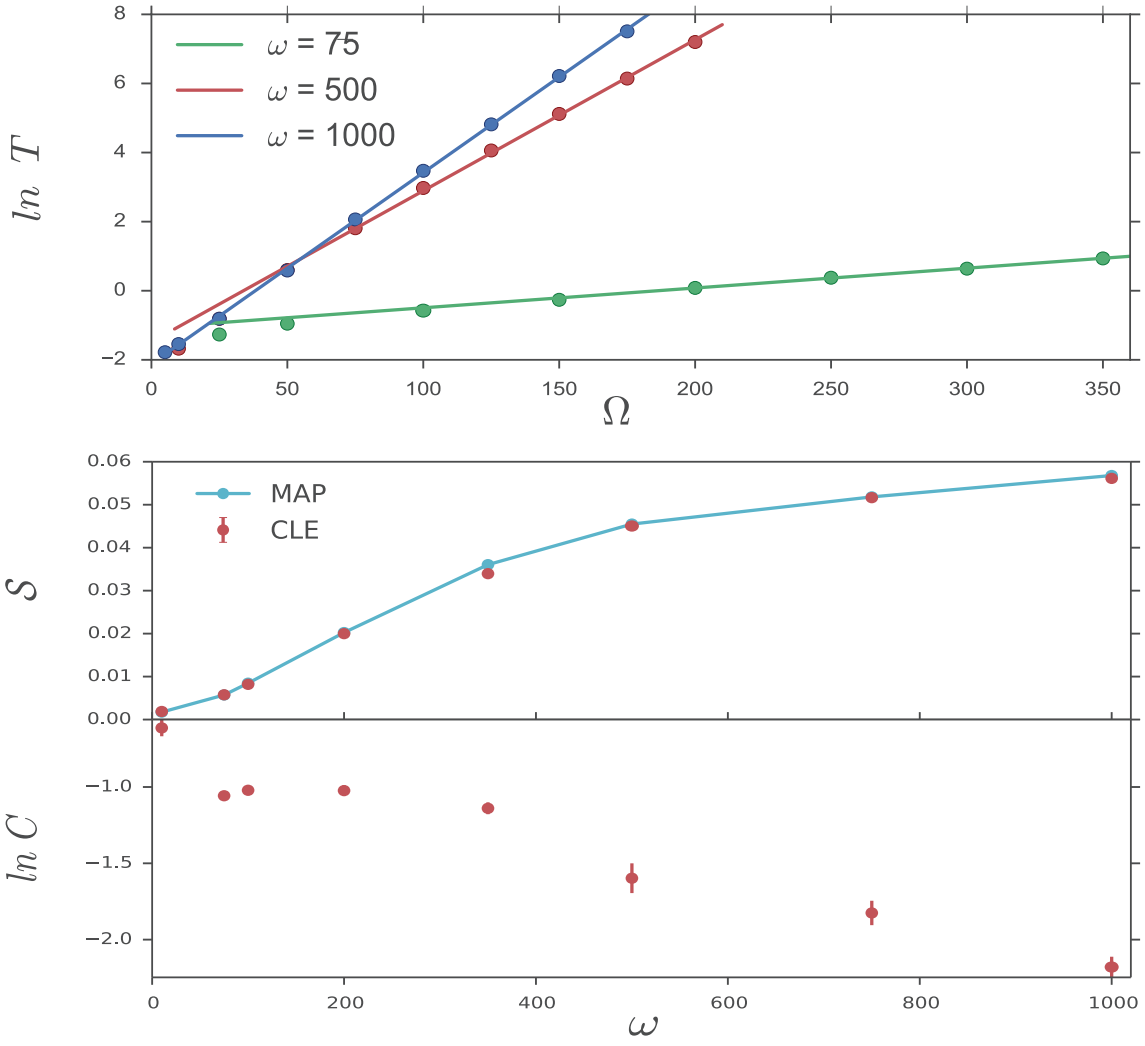

Figure 3.4: Comparison of predictions of the MFPT. Top) Comparison of MFPTs calculated from CLE simulations (*circles*) with the exponential dependence of the MFPT on Ω given by $\mathcal{S}$ (*lines*). Each line is computed by minimizing the action $\mathcal{S}$ for different ω and fitting the prefactor C. Bottom) Following the same procedure, the value of the action $\mathcal{S}$ and C are compared for different values of ω. Parameters values are the same as those of Fig. 3.2, error bars are standard error of the mean from the CLE.

$t_n = 2\pi n/\omega$. The probability of exiting at the $n-$th revolution follows the geometric distribution

$$\mathcal{P}(t_n) = p(1-p)^{\frac{\omega t_n}{2\pi}-1}. \tag{3.5.1}$$

Using rare event theory, we can write the success probability as $p = \mathrm{e}^{-\mathcal{S}\Omega}/\mathrm{C}$. The distribution Eq. (3.5.1) becomes

$$\mathcal{P}(t_n) = \frac{\left(1-\mathrm{e}^{-\mathcal{S}\Omega}/C\right)^{\frac{\omega t_n}{2\pi}}}{C\mathrm{e}^{\mathcal{S}\Omega}-1}. \tag{3.5.2}$$

Interestingly, since escape is rare, the probability p will be very small and there will usually be many revolutions before the exit from the limit cycle occurs. In the limit $p \to 0$, the discrete geometric distribution (3.5.2) can be approximated by its continuum counterpart, the exponential distribution, which does not depend explicitly on the angular velocity,

$$\mathcal{P}(t) = \frac{1}{C}\mathrm{e}^{-\mathcal{S}\Omega+\frac{t}{C}\exp(-\mathcal{S}\Omega)}. \tag{3.5.3}$$

Comparing the distributions Eqs. (3.5.2) and (3.5.3), with the probability distribution of MFPT obtained over several CLE realizations, we obtained a good agreement (see Fig. 3.5). Surprisingly, even for realizations with a low average number of revolutions prior to escape, the resulting probability distribution is more similar to an exponential distribution than to a geometric one. This is true even for escapes that occur during the first revolution, suggesting that θ differs significantly from ωt. A more accurate prediction would involve a convolution of geometric processes with the angular noise [19, 20]. However, for the parameters we used, the exponential distribution fits well independently of the average number of revolutions. Fitting the distribution (3.5.3) to the MPFTs from CLE realizations therefore provides an alternative method to compute the prefactor C.

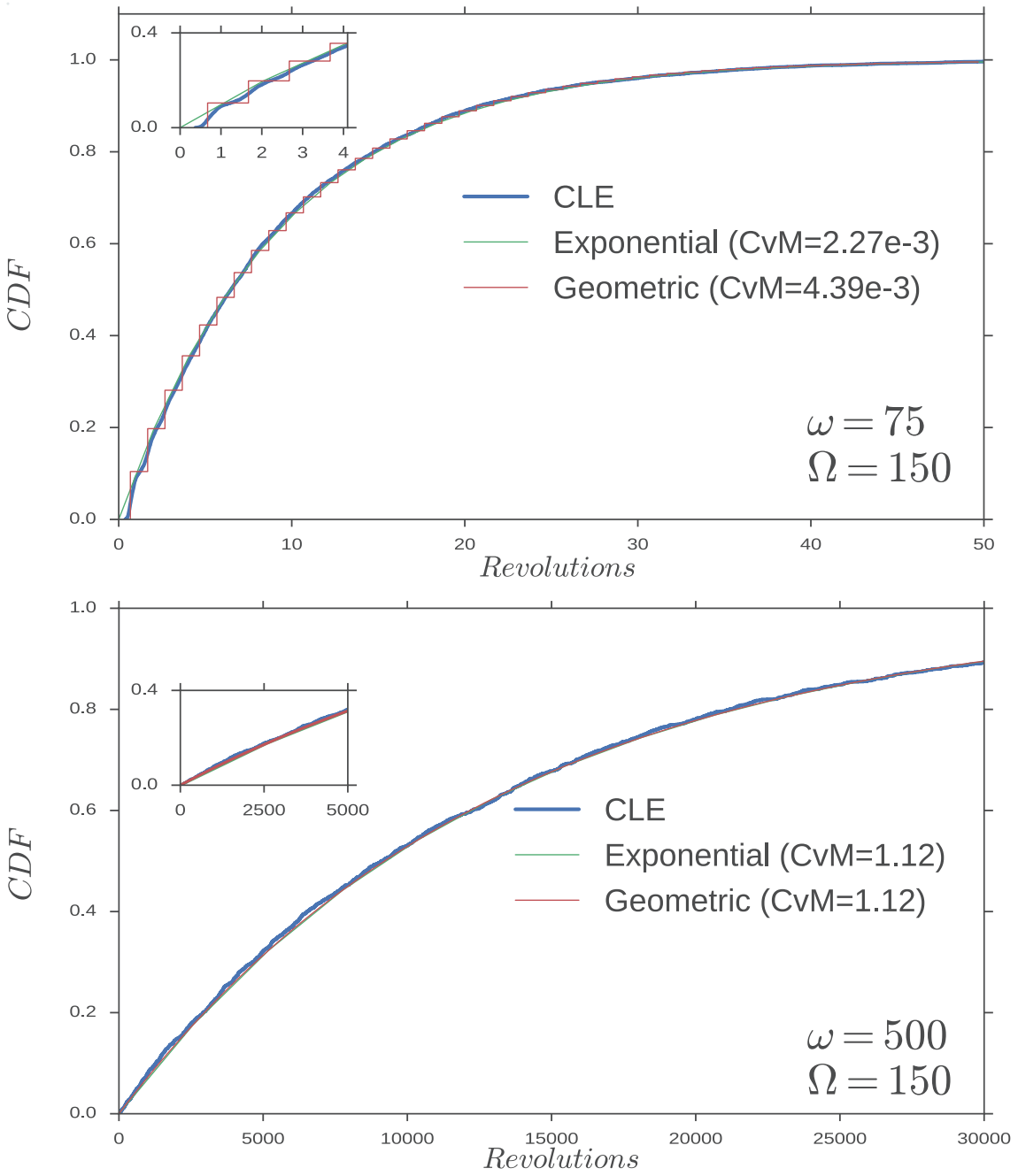

Figure 3.5: Comparison of the Cumulative Distribution Function (CDF) of the number of turns $t/(2\pi\omega)$ for 10000 realizations with $\omega = 75$ and 2000 realizations with $\omega = 500$ of CLE. For each distribution the Cramer-von Mises (CvM) criterion is computed to compare the resulting distribution with the geometric and exponential distribution determined by the value of the action.

Part 2

Stochastic multi-scale modelling of cellular populations

Chapter 4

Stochastic multi-scale models of competition within heterogeneous cellular populations: simulation methods and mean-field analysis

4.1 Introduction

In this chapter we analyse the properties of heterogeneous populations under the effects of fluctuations both within the intracellular pathways which regulate (individual) cell behaviour and those associated to intrinsic randomness due to finite size of the population. To this purpose, we expand upon the stochastic multi-scale methodology developed in [89], where it was shown that such a system can be described by an age-structured birth-and-death process, instead of a branching process [43, 52]. The coupling between intracellular and the birth-and-death dynamics is carried out through a novel method to obtain the birth rate from the stochastic cell-cycle model, based on a mean-first passage time approach. Cell proliferation is assumed to be activated when one or more of the proteins involved in the cell-cycle regulatory pathway hit a threshold. This view allows us to calculate the birth rate as a function of the age of the cell and the extracellular oxygen in terms of the associated mean-first passage time (MFPT) problem [185]. The present approach differs from that in [89] in that our treatment of the intracellular MFPT is done in terms of a large deviations approach, the so-called optimal path theory [27, 63].

This methodology allows us to explore the effects of intrinsic fluctuations within the intracellular dynamics, in particular a model of the oxygen-regulated G1/S which dictates when cells are prepared to divide, as a source of heterogeneous behaviour: fluctuations induce variability in the birth rate within the population (even to the point of rendering some cells quiescent, i.e. stuck in G0) upon which a cell-cycle dependent

therapy acts as a selective pressure.

This chapter is organised as follows. Section 4.2 provides a summary of the structure of the multi-scale. In Section 4.3, we give a detailed discussion of the intracellular dynamics, i.e. the stochastic model of the oxygen-regulated G1/S transition, and its analysis. In Section 4.4, we summarise the formulation of the age-structured birth-and-death process, the numerical simulation technique, and the mean-field analysis of a homogeneous population. In Section 4.5, we discuss how noise within the intracellular dynamics induces heterogeneity in the population and analyse the stochastic dynamics of competition for a limited resource within such heterogeneous populations. In Section 4.6 we further study the effects of noise-induced heterogeneity on the emergence of drug resistance upon administration of a cell cycle-specific therapy.

4.2 Summary of the multi-scale model

Before proceeding with a detailed discussion of the different elements involved in the formulation of the stochastic multi-scale model, it is useful to provide a general overview of the overall structure of the model, which is closely related to that of the model proposed in [6].

The model we present in this chapter integrates phenomena characterised by different time scales, as schematically shown in Fig.4.1. This model intends to tackle the growth and competition of cellular populations under the restriction of finite amount of available resources (in this case, oxygen) supplied at a finite rate, $\bar{S}$.

The general approach used in this model is a natural generalisation of the standard continuous-time birth-and-death Markov process and its description via a Master Equation [68]. As we will see, the consideration of the multi-scale character of the system, i.e. the inclusion of the physiological structure associated with the cell-cycle variables, introduce an age-structure within the population: the birth rate depends on the age of cell (i.e. time elapsed since last division) which determines, through the corresponding cell-cycle model, the cell-cycle status of the corresponding cells.

The evolution of the concentration of oxygen, $c(t)$, (*resource scale*, see Fig. 4.1) is modelled by:

$$\frac{dc}{dt} = \bar{S} - kc \sum_{i=1}^{N_T} N_i(t) \tag{4.2.1}$$

where N_T is the number of cellular types consuming the resource c, and $N_i(t)$, $i = 1, \ldots, N_T$, is the number of cells of type i at time t. Note that, in general, $N_i(t)$ is a stochastic process, and, therefore, in principle Eq. (4.2.1) should be treated as a

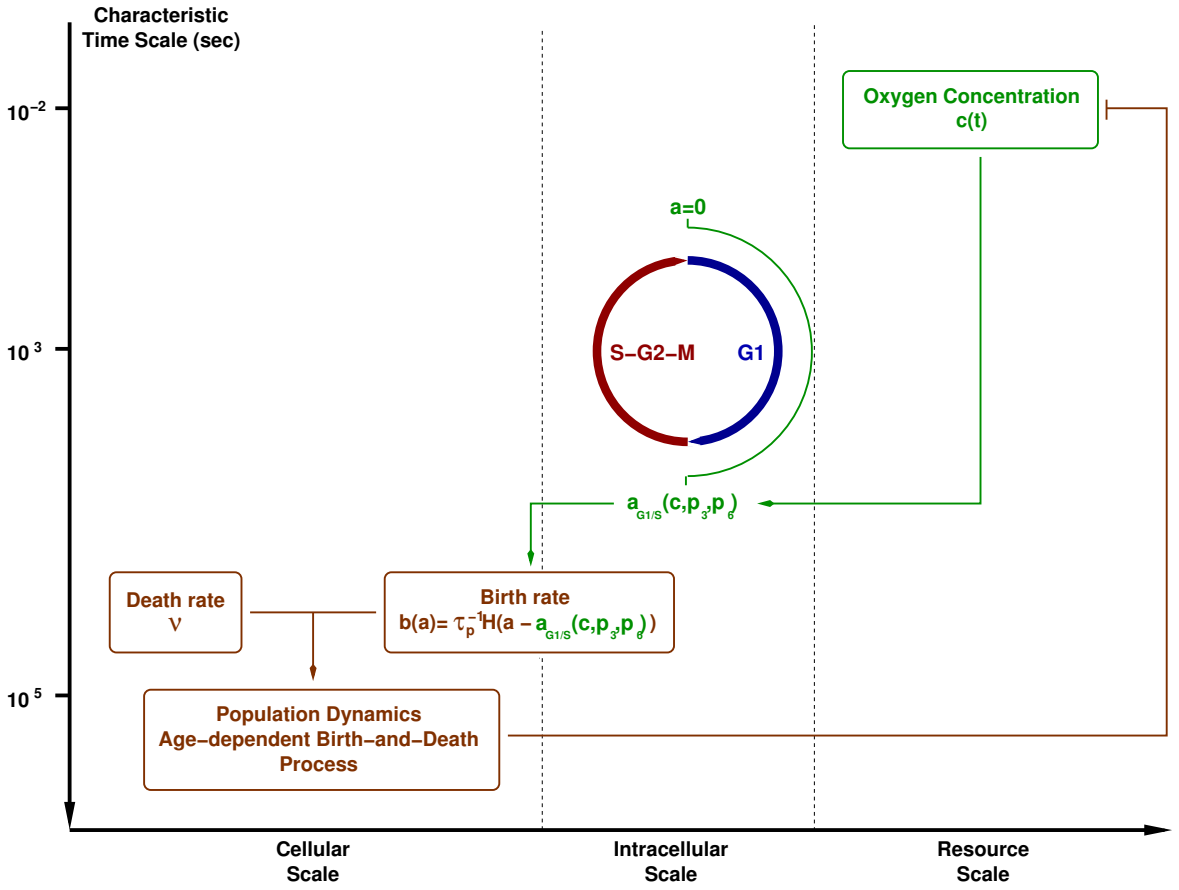

Figure 4.1: Schematic representation of the different elements that compose our multi-scale model. We show the different levels of biological organisation as well as associated characteristic time scales [89] associated to each of these layers: resource scale, i.e. oxygen which is supplied at a constant rate and consumed by the cell population, cellular scale, i.e. oxygen-regulated cell cycle progression which determines the age-dependent birth rate into the cellular layer, and, finally, the cellular scale, which is associated to the stochastic population dynamics.

stochastic differential equation [166].

The second sub-model considered in our multi-scale model, associated with the intracellular scale (see Fig. 4.1), is an stochastic model of oxygen-regulated cell-cycle progression. This sub-model is formulated using the standard techniques of chemical kinetics [76] so that the mean-field limit of the stochastic model corresponds to the deterministic cell-cycle model formulated in [18]. This model provides the physiological state of the cell in terms of the number of molecules of each protein involved in the cell-cycle of a cell of a given age, a. From such physiological state, we derive whether the G1/S transition has occurred. The cell-cycle status of a cell of age a is determined in terms of whether the abundance of certain proteins which activate the cell-cycle (cyclins) have reached a certain threshold. In our particular case, if at age a, the cyclin levels are below the corresponding threshold, the cell is still in G1. If, on the contrary, the prescribed threshold level has been reached, the cell has passed onto S, and therefore is ready to divide. This implies that the probability of a cell having crossed the threshold of cyclin levels at age a can be formulated in terms of a mean first-passage time problem (MFTP) in which one analyses the probability of a Markov process to hit a certain boundary [68, 185]. Unlike our approach in [89], based on approximating the full probability distribution of the stochastic cell cycle model, in the present approach, passage time is (approximately) solved in terms of an optimal trajectory path approach [27, 63].

At the interface between the intracellular and cellular scales sits our model of the (age-dependent) birth rate, which defines the probability of birth per unit time (cellular scale) in terms of the cell cycle variables (intracellular scale). The rate at which our cell-cycle model hits the cyclin activation threshold, i.e. the rate at which cells undergo G1/S transition, is taken as proportional to the birth rate. In particular, the birth rate is taken to be function of the age of the cell as well as the concentration of oxygen, as the oxygen abundance regulates the G1/S transition age, $a_{G1/S}(c)$, i.e. the time (age) elapsed between the birth of a cell and its G1/S transition:

$$b(a) = \tau_p^{-1}\mathcal{H}(a - a_{G1/S}(c)). \tag{4.2.2}$$

i.e. cell division occurs at a constant rate, τ_p^{-1}, provided cells have undergo the G1/S transition and $\mathcal{H}$ is the Heaviside function. In other words, we consider that the duration of the G1 phase is regulated by the cell cycle model, whereas the duration of the S-G2-M is a random variable, exponentially distributed with average duration equal to τ_p (see Fig. 4.1).

The third (and last) sub-model is associated with the cellular scale. It corresponds to the dynamics of the cell population and it is governed the Master Equation for the probability density function of the number of cells [68]. The stochastic process that describes the dynamics of the population of cells is an age-dependent birth-and-death

process where the birth rate is given by Eq. (4.2.2) where $a_{G1/S}(c)$ is provided by the intracellular model. The death rate is, for simplicity, considered constant. As a consequence of the fact that the birth rate is age-dependent, our Multi-Scale Master Equation (MSME) does not present the standard form for unstructured populations, rather, it is an age-dependent Master Equation.

A detailed description of each sub-model and its analysis is given in Sections 4.3 and 4.4, respectively.

4.3 Intracellular scale: Stochastic model of the oxygen-regulated G_1/S transition

4.3.1 Biological background

Cell proliferation is orchestrated by a complex network of protein and gene expression regulation, the so-called cell cycle, which accounts for the timely coordination of proliferation with growth and, by means of signalling cues such as growth factors, tissue function [233]. Dysregulation of such orderly organisation of cell proliferation is one of the main contributors to the aberrant behaviour observed in tumours [229].

The cell cycle has the purpose of regulating the successive activation of the so-called cyclin-dependent kinases (CDKs) which control the progression along the four phases of cycle: G1 (first gap phase), S (DNA replication), G2 (second gap phase), and M (mitosis) [71, 72, 75]. This four phases must be supplemented with a fifth, G0, which account for cells that are quiescent due to lack of stimulation (i.e. absence of growth factors, lack of basic nutrients, etc.) to proliferate. Current models of the cell cycle organise the complex regulatory network into CDK modules, each centred around a cyclin-CDK complex which is key for the transition between the cell cycle phases (see, for example, [71]): cyclin D/CDK4-6 and cyclin E/CDK2 regulate progression during the G1 phase and elicit the G1/S transition, cyclin A/CDK2 promote progression during S phase and orchestrates the S/G2 transition, and, finally, cyclin B/CDK2 brings about the G2/M transition. The activity of each of these cyclin-CDK complexes is regulated in a timely manner, so that each phase of the cell cycle ensues at the proper time, by means of transcriptional regulation, postranscriptional modifications (e.g. phosphorylation), and degradation (via ubiquitination) in which a large number of other components participate, including transcription factors, enzymes, ubiquitins, etc.

In this chapter, we propose a coarse-grained description of the cell cycle phases by lumping S, G2, and M into one phase, so that we consider a two-phase model G1 and S-G2-M, as shown in Fig. 4.1, [5]. In particular, we use the simplifying assumption that cells can only divide once they have entered the S-G2-M phase at a constant rate. Entry in S-G2-M is regulated by a (stochastic) model of the G1/S transition which takes

into account the regulation of the duration of the G1 phase by hypoxia (lack of oxygen).

The abundance of oxygen is known to be one of the factors that regulate the duration of the G_1 phase of the cell cycle. The issue of the regulation of the G_1/S transition by the oxygen concentration has been the subject of several modelling studies [5, 18]. These models focus on the hypoxia-induced delay of the activation of the cyclins either through activation of cyclin inhibitors [5] or via up-regulation of the HIF-1α transcription factor [18]. From the modelling point of view, both of them are mean-field models, thus neglecting fluctuations. In this Section, we formulate a stochastic version of the model of Bedessem & Stephanou [18], of which an schematic representation is shown in Fig. 4.2.

HIF-1 mediates adaptive responses to lack of oxygen [198]. HIF-1 is a heterodimer consisting of two sub-units: HIF-1α and HIF-1β. Whilst the latter is constitutively expressed, HIF-1α is O_2-regulated. In the presence of adequate oxygen availability is negatively regulated by the von Hippel-Lindau (VHL) tumour suppressor protein, which allows HIF-1α for degradation. VHL loss-of-function mutations are usual in many types of tumours, which allows for de-regulated HIF-1α degradation [198]. HIF-1 is involved in a number of cellular responses including switch from oxidative phosphorylation to glycolysis, activation of angiogenic pathways, and inhibition of cell cycle progression [30, 198].

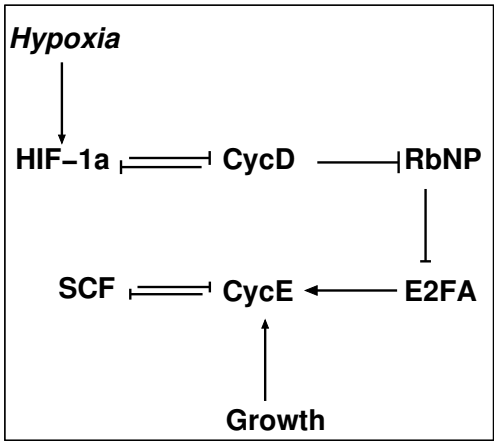

Figure 4.2: Schematic representation of the elements involved in the model of hypoxia-regulated G_1/S transition proposed by Bedessem & Stephanou [18]. Within the framework of this model, the negative-feedback between CycE and SCF is the key modelling ingredient for the system to emulate the behaviour of a cell during the G1/S transition. The relative balance between CycE (which promotes the G1/S transition) and SCF (G1/S transition inhibitor) is regulated by growth and hypoxia, so that the timing of the transition depends upon these two factors.

4.3.2 Mean-field model of the regulation of the G1/S transition by hypoxia

Bedessem & Stephanou formulate a model of the effect of hypoxia (mediated by HIF-1) on the timing of the G1/S transition [18]. The involvement of HIF-1 in cell cycle regulation is complex and not completely understood. There is evidence that HIF-1 delays entry into S(-G2-M) phase by activating p21, a CDK inhibitor, [134, 167]. HIF-1 up-regulation of p21 mediates indirect down-regulation of cyclin E [81]. Further to HIF-1 regulation of the cell cycle, there exists a feedback regulation of cell cycle proteins of HIF-1. Hubbi et al. [107] report that CDK1 and CDK2 physically and functionally interact with HIF-1α: CDK1 down-regulates lysosomal degradation of HIF-1α, thus consolidating its stability and promoting its transcriptional activity. On the contrary, CDK2 activates lysosomal degradation of HIF-1α and promotes G1/S transition. Bedessem & Stephanou [18] do not take into account all these issues and, for simplicity, chose to focus on the well-documented effect of HIF-1 on cyclin D [167, 230].

Bedessem & Stephanou [18] model formulation is based on the following assumptions:

1. The G1/S is modelled by a biological switch which emerges from the mutual inhibition between a cyclin (in this case, cyclin E) and an ubiquitin complex (SCF complex): The latter marks the former for degradation whereas cyclin E mediates inactivation of the SCF complex. This mutual inhibition gives rise to a bistable situation in which two stable fixed points coexist, each associated with the G1 phase (high SCF activity, low cyclin E concentration) and the S-G2-M phase (low SCF activity, high cyclin E concentration). Activation and inactivation of the SCF complex are assumed to follow Michaelis-Menten kinetics.

2. As in previous models [5, 161, 224], the G1/S transition is brought about by triggering a saddle-node bifurcation, whereby the G1 phase fixed point collides with the unstable saddle, driving the system into S-G2-M fixed point. Two factors drive the system through this bifurcation: cell growth (logistic increase of the cell mass [224]) and activation of the E2F transcription factor. In [18], both factors are taken to up-regulate the transcription of cyclin E.

3. Activation of E2F is modelled in terms of the E2F-Retinoblastoma protein (RBP) switch [140]. Briefly, E2F is captured (bound) by unphosphorylated RBP. Upon phosphorylation, RBP releases E2F which activates transcription of G1/S-transition promoting cyclins, such as cyclin E [9]. Further, E2F can be in unphosphorylated (active) form and phosphorylated (inactive) form. Following [161], Bedessem & Stephanou assume that fraction of active E2F and RBP-bound E2F are in adiabatic equilibrium with unphosphorylated RBP and total free E2F [18]. Furthermore, [18] takes cyclin D to phosphorylate RBP.

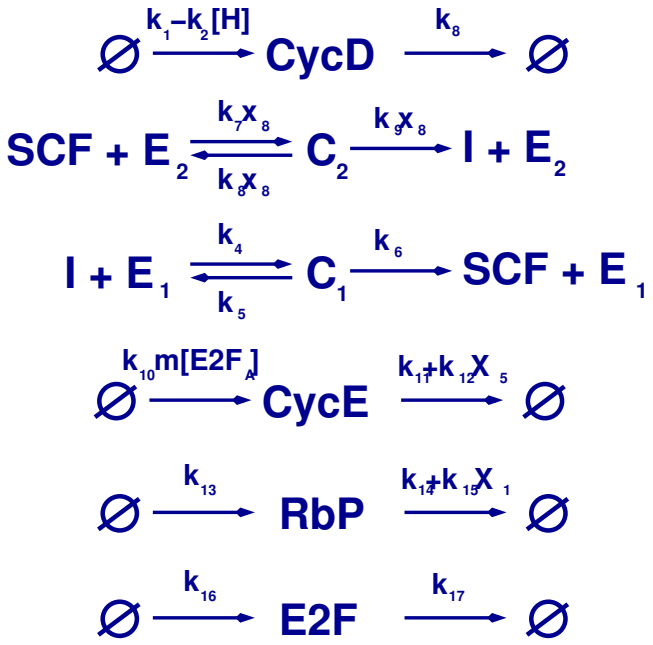

Figure 4.3: Reactions for the stochastic version of the model proposed by Bedessem & Stephanou [18]. The reactions correspond (from top to bottom): hypoxia-inhibited synthesis and degradation of CycD, enzyme-catalysed, CycE-mediated inactivation of SCF, enzyme-catalysed activation of SCF, synthesis (regulated by growth and active E2F) and degradation (up-regulated by active SCF) of CycE, synthesis and degradation of Rb, and, last, synthesis and degradation of E2F. The negative feedback (mutual inhibition) between SCF and CycE mediates bistable behaviour in this model of the G1/S transition. Some of the transition rates associated to the reactions shown in are not constant but depend on the number of molecules of chemical species i present at a particular time, X_i. For the definition of the quantities X_i, we refer the reader to Table 4.1.

4. Last, Bedessem & Stephanou [18] assume that HIF-1α inhibits synthesis of cyclin D. Following experimental evidence reported in [230], they assume that the level of HIF-1α depends exponentially of the oxygen concentration.

These basic hypotheses are primarily based on previous models [5, 161, 224]. The resulting pathway is schematically represented in Fig. 4.2.

4.3.3 Stochastic G1/S transition model

Based on the hypotheses summarised in Section 4.3.2, Bedessem & Stephanou [18] formulated a mean-field model which is able to reproduce such behaviours as delay of the G1/S due lo lack of oxygen as well as hypoxia-induced quiescence. Here, we present a stochastic model (see Fig. 4.3 and Table 4.1), whose mean field limit is the

Variable	Description
X_1, X_8	Number of CyclinD and CyclinE molecules, respectively
X_2, X_5	Number of inactive and active SCF molecules, respectively
X_3, X_6	Number of SCF-activating/inactivating enzyme molecules, respectively
X_4, X_7	Number of enzyme-inactive/active SCF complexes, respectively
X_9, X_{10}	Number of free RbP and E2F molecules, respectively

Reaction probability p.u.t	r_i
$W_1 = k_1 - k_2[H]$	$(1,0,0,0,0,0,0,0,0,0)$
$W_2 = k_3 X_1$	$(-1,0,0,0,0,0,0,0,0,0)$
$W_3 = k_4 X_2 X_3$	$(0,-1,-1,1,0,0,0,0,0,0)$
$W_4 = k_5 X_4$	$(0,1,1,-1,0,0,0,0,0,0)$
$W_5 = k_9 X_8 X_7$	$(0,1,0,0,0,1,-1,0,0,0)$
$W_6 = k_6 X_4$	$(0,0,1,-1,1,0,0,0,0,0)$
$W_7 = k_7 X_5 X_8 X_6$	$(0,0,0,0,-1,-1,1,0,0,0)$
$W_8 = k_8 X_8 X_7$	$(0,0,0,0,1,1,-1,0,0,0)$
$W_9 = k_{10} m \left(1 - \frac{X_9}{[E2F]_{tot}}\right) X_{10}$	$(0,0,0,0,0,0,0,1,0,0)$
$W_{10} = (k_{11} + k_{12} X_5) X_8$	$(0,0,0,0,0,0,0,-1,0,0)$
$W_{11} = k_{13}$	$(0,0,0,0,0,0,0,0,1,0)$
$W_{12} = (k_{14} + k_{15} X_1) X_9$	$(0,0,0,0,0,0,0,0,-1,0)$
$W_{13} = k_{16}$	$(0,0,0,0,0,0,0,0,0,1)$
$W_{14} = k_{17} X_{10}$	$(0,0,0,0,0,0,0,0,0,-1)$

Table 4.1: Reaction probability per unit time, $W_i \equiv W(X, r_i, t)$, $i = 1, .., 14$. The mass is assumed to grow following a logistic law: $m(a) = \frac{m_* K e^{\eta a}}{K e^{\eta a} - 1} = \frac{m_*}{1 - K e^{-\eta a}}$, where $K = 1 - \frac{m_*}{m(0)}$ and a is the age of the cell (i.e. the time elapsed since birth). According to [18], the level of active HIF-1α, $[H]$, depends exponentially on the extracellular oxygen concentration, c: $[H] = H_0 e^{\beta_1 (1-c)}$. Furthermore, Following Novak and Tyson [161], we assume that at each time, the active E2F, $[E2F_A]$, is the fraction of unphosphorylated free E2F factor, $[E2F]$: $[E2F_A] = \frac{([E2F]_{tot} - [E2F_{Rb}])[E2F]}{[E2F]_{tot}}$. The equilibrium between E2F-Rb complexes; free E2F and free Rb is given by [161]: $[E2F_{Rb}] = [Rb] = \frac{2[E2F]_{tot}[Rb]}{[E2F]_{tot} + [Rb] + \sqrt{([E2F]_{tot} + [Rb])^2 - 4[E2F]_{tot}[Rb]}} = \min\{[E2F]_{tot}, [Rb]\}$

model formulated in [18]. We analyse this model using the stochastic quasi-steady state approximation we have developed in Chapter 2.

The deterministic model formulated in [18], which we have briefly described in Section 4.3.2, is based on a series of reactions shown in Fig. 4.3, which include Michaelis-Menten kinetics for activation and inactivation of SCF complexes. Our stochastic model of the G1/S transition builds upon the stochastic (Markovian) description of the same set of reactions.

Our model is based on the stochastic dynamics of the state vector being described by a Markov jump process [88, 120], whereby the state of the system, X, changes by an amount r_i when the elementary reaction i occurs. The waiting time between Markovian events is exponentially distributed, the process is characterised by the associated transition rates, i.e. $P(X(a+\Delta a) = X + r_i | X(a) = X) = W_i(X)\Delta a + O(\Delta a^2)$. Using law of mass action [76] as our basic modelling framework, the transition rates of each elementary process are given in Table 4.1. Once we have determined the transition rates associated with each elementary reaction (or channel), the dynamics of the system is given by the Chemical Master Equation of a (non-structured) Markov Process, $X(a)$:

$$\frac{\partial P(X,a)}{\partial a} = \sum_{i=1}^{R} \left(W_i(X - r_i)P(X - r_i, a) - W_i(X)P(X,a) \right) \tag{4.3.1}$$

where $P(X,a)$ is the probability of the state vector of the system to be X at age a, i.e. the time reckoned from the last division. The transition rates, $W_i(X)$, the vectors r_i (whose components are the variation of the number of each chemical species upon occurrence of reaction i) are given in Table 4.1 and determine the dynamics of the system.

Even for moderately complex models, Eq. (4.3.1) has no solution in closed form. Therefore, in order to study the properties of the system one must resort to numerical simulation (Monte Carlo) or asymptotic approximations. In the next section, we present an asymptotic analysis based on developed in the chapter 2 stochastic quasi-steady state approximation.

4.3.4 Semi-classical quasi-steady state analysis of the stochastic G1/S transition model

In Chapter 2, we have developed a stochastic version of the classical QSS approximation, the so-called semi-classical QSS approximation (SCQSSA) which, within the framework of the optimal path theory, allows us to tackle systems which exhibit separation of time scales, such as enzyme-catalysed reactions. Since these type of reaction features prominently in our stochastic model of the hypoxia-regulated G1/S transition

(see Fig. 4.3), we will use the SCQSSA to analyse the effects of intrinsic noise on the stochastic model of the hypoxia-regulated G1/S transition (as determined by the transition rates shown in Table 4.1). This approximation allows us to study noise-induced phenomena which are relevant for the timing of the G1/S transition and, therefore, bear upon the population dynamics.

We derive the equations of the SCQSSA of the stochastic model of the G1/S transition as defined by the Master Equation Eq. (4.3.1) and the associated transition rates shown in Table 4.1. See section 2.2 for details of the procedure. The associated generating function satisfies the following PDE:

$$\frac{\partial G}{\partial t} = H(p_1, \ldots, p_{10}, \partial_{p_1}, \ldots, \partial_{p_{10}})G(p_1, \ldots, p_{10}, t) \tag{4.3.2}$$

where the operator $H(p_1, \ldots, p_{10}, Q_1, \ldots, Q_{10}) \equiv H(p, Q)$, where $Q_i \equiv \partial_{p_i}$ which satisfies the commutation relation $[Q_i, p_j] = S_{0,i}\delta_{i,j}$, is given by:

$$H(p, Q) = H_1(p, Q) + H_2(p, Q) + H_3(p, Q) + H_4(p, Q) + H_5(p, Q) + H_6(p, Q) \tag{4.3.3}$$

where the full Hamiltonian $H(p, Q)$ has been separated into 6 parts, each corresponding to one of the reactions shown in Fig. 4.3. Using (2.2.4) we obtain:

$$H_1(p, Q) = k_4(p_4 - p_2p_3)Q_2Q_3 + k_5(p_2p_3 - p_4)Q_4 + k_6(p_3p_5 - p_4)Q_4, \tag{4.3.4}$$

and

$$H_2(p, Q) = k_9p_8(p_2p_6 - p_7)Q_7Q_8 + k_7p_8(p_7 - p_5p_6)Q_5Q_6Q_8 + k_8p_8(p_5p_6 - p_7)Q_7Q_8, \tag{4.3.5}$$

correspond to enzymatic activation and (CycE-mediated) inactivation of SCF (X_5), respectively. $H_3(p, Q)$ through to $H_6(p, Q)$ are given by:

$$H_3(p, Q) = (k_1 - k_2)(p_1 - 1) + k_3(1 - p_1)Q_1, \tag{4.3.6}$$

$$H_4(p, Q) = k_{10}m(p_8 - 1)p_{10}Q_{10}(1 - \frac{p_9}{[e2f]_{tot}}Q_9) + (1 - p_8)Q_8(k_{11} + k_{12}p_5Q_5), \tag{4.3.7}$$

$$H_5(p, Q) = k_{13}(p_9 - 1) + (1 - p_9)(k_{14}Q_9 + k_{15}p_1Q_1Q_9), \tag{4.3.8}$$

$$H_6(p, Q) = k_{16}(p_{10} - 1) + k_{17}(1 - p_{10})Q_{10}, \tag{4.3.9}$$

Dimensionless variables	Dimensionless parameters
$a = k_7\mathcal{E}\mathcal{S}t$	$\epsilon = \mathcal{E}/\mathcal{S}$
$q_1 = Q_1/\mathcal{S}$	$\widehat{[e2f]}_{tot} = [e2f]_{tot}/\mathcal{S}$
$q_2 = Q_2/\mathcal{S}$	$\kappa_1 = k_1/(k_7\mathcal{E}\mathcal{S}^2)$
$q_3 = Q_3/\mathcal{E}$	$\kappa_2 = k_2/(k_7\mathcal{E}\mathcal{S}^2)$
$q_4 = Q_4/\mathcal{E}$	$\kappa_3 = k_3/(k_7\mathcal{E}\mathcal{S})$
$q_5 = Q_5/\mathcal{S}$	$\kappa_4 = k_4/(k_7\mathcal{S})$
$q_6 = Q_6/\mathcal{E}$	$\kappa_5 = k_5/(k_7\mathcal{S}^2)$
$q_7 = Q_7/\mathcal{E}$	$\kappa_6 = k_6/(k_7\mathcal{S}^2)$
$q_8 = Q_8/\mathcal{S}$	$\kappa_8 = k_8/(k_7\mathcal{S})$
$q_9 = Q_9/\mathcal{S}$	$\kappa_9 = k_9/(k_7\mathcal{S})$
$q_{10} = Q_{10}/\mathcal{S}$	$\kappa_{10} = k_{10}/(k_7\mathcal{E}\mathcal{S})$
	$\kappa_{11} = k_{11}/(k_7\mathcal{E}\mathcal{S})$
	$\kappa_{12} = k_{12}/(k_7\mathcal{E})$
	$\kappa_{13} = k_{13}/(k_7\mathcal{E}\mathcal{S}^2)$
	$\kappa_{14} = k_{14}/(k_7\mathcal{E}\mathcal{S})$
	$\kappa_{15} = k_{15}/(k_7\mathcal{E})$
	$\kappa_{16} = k_{16}/(k_7\mathcal{E}\mathcal{S}^2)$
	$\kappa_{17} = k_{17}/(k_7\mathcal{E}\mathcal{S})$

Table 4.2: Dimensionless variables and parameters corresponding.

which are the Hamiltonians associated with synthesis and degradation of CycD (X_1), CycE (X_8), Rb (X_9), and E2F (X_{10}), respectively.

By re-scaling the coordinate-like variables Q_i according to the scaling shown in Table 4.2 and defining the dimensionless time as $a = k_7\mathcal{E}\mathcal{S}t$, the associated Hamilton equations, Eqs. (2.2.9)-(2.2.10)

$$\frac{dq_1}{da} = \kappa_1 - \kappa_2 - \kappa_3 q_1 + \kappa_{15}(1 - p_9)q_1 q_9 \tag{4.3.10}$$

$$\frac{dq_2}{da} = -\kappa_4 p_3 q_2 q_3 + \kappa_5 p_3 q_4 + \kappa_9 p_8 p_6 q_7 q_8 \tag{4.3.11}$$

$$\epsilon\frac{dq_3}{da} = -\kappa_4 p_2 q_2 q_3 + (\kappa_5 p_2 + \kappa_6 p_5)q_4 \tag{4.3.12}$$

$$\epsilon\frac{dq_4}{da} = \kappa_4 q_2 q_3 - (\kappa_5 + \kappa_6)q_4 \tag{4.3.13}$$

$$\frac{dq_5}{da} = \kappa_6 p_3 q_4 - p_8 p_6 q_5 q_6 q_8 + \kappa_8 p_8 p_6 q_7 q_8 + \kappa_{12} q_5 q_8 (1 - p_8) \tag{4.3.14}$$

$$\epsilon\frac{dq_6}{da} = \kappa_9 p_8 p_2 q_7 q_8 - p_8 p_5 q_5 q_6 q_8 + \kappa_8 p_8 p_5 q_7 q_8 \tag{4.3.15}$$

$$\epsilon\frac{dq_7}{da} = -\kappa_9 p_8 q_7 q_8 + p_8 q_5 q_6 q_8 - \kappa_8 p_8 q_7 q_8 \tag{4.3.16}$$

$$\frac{dq_8}{da} = (\kappa_9(p_2p_6 - p_7) + \kappa_8(p_5p_6 - p_7))q_7q_8 + (p_7 - p_5p_6)q_5q_6q_8 +$$
$$+ \kappa_{10}mp_{10}q_{10}\left(1 - \frac{p_9q_9}{\widehat{[e2f]}_{tot}}\right) - \kappa_{11}q_8 - \kappa_{12}p_5q_5q_8 \tag{4.3.17}$$
$$\frac{dq_9}{da} = \kappa_{10}m(1 - p_8)p_{10}\frac{q_9q_{10}}{\widehat{[e2f]}_{tot}} + \kappa_{13} - \kappa_{14}q_9 - \kappa_{15}p_1q_1q_9 \tag{4.3.18}$$
$$\frac{dq_{10}}{da} = \kappa_{10}m(p_8 - 1)q_{10}(1 - \frac{p_9q_9}{\widehat{[e2f]}_{tot}}) + \kappa_{16} - \kappa_{17}q_{10} \tag{4.3.19}$$
$$\frac{dp_1}{da} = -\kappa_3(1 - p_1) - \kappa_{15}(1 - p_9)p_1q_9 \tag{4.3.20}$$
$$\frac{dp_2}{da} = -\kappa_4(p_4 - p_2p_3)q_3 \tag{4.3.21}$$
$$\epsilon\frac{dp_3}{da} = -\kappa_4(p_4 - p_2p_3)q_2 \tag{4.3.22}$$
$$\epsilon\frac{dp_4}{da} = -\kappa_5(p_2p_3 - p_4) - \kappa_6(p_3p_5 - p_4) \tag{4.3.23}$$
$$\frac{dp_5}{da} = -p_8(p_7 - p_5p_6)q_6q_8 - \kappa_{12}(1 - p_8)p_5q_8 \tag{4.3.24}$$
$$\epsilon\frac{dp_6}{da} = -p_8(p_7 - p_5p_6)q_5q_8 \tag{4.3.25}$$
$$\epsilon\frac{dp_7}{da} = -(\kappa_9(p_2p_6 - p_7) + \kappa_8(p_5p_6 - p_7))p_8q_8 \tag{4.3.26}$$
$$\frac{dp_8}{da} = -(\kappa_9(p_2p_6 - p_7) + \kappa_8(p_5p_6 - p_7))p_8q_7 - p_8(p_7 - p_5p_6)q_5q_6$$
$$- (1 - p_8)(\kappa_{11} + \kappa_{12}p_5q_5) \tag{4.3.27}$$
$$\frac{dp_9}{da} = -\kappa_{10}m(1 - p_8)p_{10}\frac{p_9q_{10}}{\widehat{[e2f]}_{tot}} - (1 - p_9)(\kappa_{14} + \kappa_{15}p_1q_1) \tag{4.3.28}$$
$$\frac{dp_{10}}{da} = -\kappa_{10}m(p_8 - 1)p_{10}(1 - \frac{p_9q_9}{\widehat{[e2f]}_{tot}}) - \kappa_{17}(1 - p_{10}) \tag{4.3.29}$$

where $\epsilon = \mathcal{E}/\mathcal{S} \ll 1$ and the re-scaled parameters κ_i are given in Table 4.2. Applying the QSSA to the equations for the momenta p_3, p_4, p_6 and p_7 associated with the fast variables, we obtain:

$$\epsilon\frac{dp_3}{da} = 0 \Rightarrow p_4 = p_2p_3, \quad \epsilon\frac{dp_4}{da} = 0 \Rightarrow p_4 = p_5p_3 \tag{4.3.30}$$
$$\epsilon\frac{dp_6}{da} = 0 \Rightarrow p_7 = p_5p_6, \quad \epsilon\frac{dp_7}{da} = 0 \Rightarrow p_7 = p_2p_6 \tag{4.3.31}$$

which implies that $p_2 = p_5$, which, in turn, yields that $p_8 = 1$ (see Eqs. (4.3.21) and (4.3.24)). Furthermore, the QSSA applied to the equations for the generalised

coordinates associated with the SCF-activating, q_3, Eq. (4.3.12), and the enzyme-active SCF complex, q_7, Eq. (4.3.16), yields:

$$\epsilon\frac{dq_3}{da} = 0 \Rightarrow \kappa_5 q_4 - \kappa_4 q_2 q_3 = -\kappa_6 q_4, \quad \epsilon\frac{dq_6}{da} = 0 \Rightarrow \kappa_8 q_7 - q_5 q_6 = -\kappa_9 q_7, \tag{4.3.32}$$

which implies that $q_2 + q_5 = p_c$. Furthermore, since $q_3 + q_4 = p_{e_1}$ and $q_6 + q_7 = p_{e_2}$ are satisfied, we obtain that:

$$q_4 = \frac{p_{e_1} q_2}{q_2 + \frac{\kappa_5+\kappa_6}{\kappa_4}}, \quad q_7 = \frac{p_{e_2} q_5}{q_5 + (\kappa_8 + \kappa_9)} \tag{4.3.33}$$

Finally, using Eqs. (4.3.30)-(4.3.33), the SCQSSA equations for the stochastic model of the G1/S transition are:

$$\frac{dq_1}{da} = \kappa_1 - \kappa_2 - \kappa_3 q_1 + \kappa_{15}(1 - p_9) q_1 q_9 \tag{4.3.34}$$

$$\frac{dq_5}{da} = \frac{\kappa_6 p_3 p_{e_1}(p_c - q_5)}{(p_c - q_5) + \frac{\kappa_5+\kappa_6}{\kappa_4}} - \frac{\kappa_9 p_8 p_6 p_{e_2} q_5 q_8}{q_5 + (\kappa_8 + \kappa_9)} \tag{4.3.35}$$

$$\frac{dq_8}{da} = \kappa_{10} m p_{10} q_{10} \left(1 - \frac{p_9 q_9}{\widehat{[e2f]}_{tot}}\right) - \kappa_{11} q_8 - \kappa_{12} p_5 q_5 q_8 \tag{4.3.36}$$

$$\frac{dq_9}{da} = \kappa_{10} m (1 - p_8) p_{10} \frac{q_9 q_{10}}{\widehat{[e2f]}_{tot}} + \kappa_{13} - \kappa_{14} q_9 - \kappa_{15} p_1 q_1 q_9 \tag{4.3.37}$$

$$\frac{dq_{10}}{da} = \kappa_{10} m (p_8 - 1) q_{10} (1 - \frac{p_9 q_9}{\widehat{[e2f]}_{tot}}) + \kappa_{16} - \kappa_{17} q_{10} \tag{4.3.38}$$

$$q_2 = p_c - q_5 \tag{4.3.39}$$

$$q_4 = \frac{p_{e_1} q_2}{q_2 + \frac{\kappa_5+\kappa_6}{\kappa_4}}, \quad q_3 + q_4 = p_{e_1} \tag{4.3.40}$$

$$q_7 = \frac{p_{e_2} q_5}{q_5 + (\kappa_8 + \kappa_9)}, \quad q_6 + q_7 = p_{e_2} \tag{4.3.41}$$

$$\frac{dp_1}{da} = -\kappa_3 (1 - p_1) - \kappa_{15}(1 - p_9) p_1 q_9 \tag{4.3.42}$$

$$\frac{dp_9}{da} = -\kappa_{10} m (1 - p_8) p_{10} \frac{p_9 q_{10}}{\widehat{[e2f]}_{tot}} - (1 - p_9)(\kappa_{14} + \kappa_{15} p_1 q_1) \tag{4.3.43}$$

$$\frac{dp_{10}}{da} = -\kappa_{10} m (p_8 - 1) p_{10} (1 - \frac{p_9 q_9}{\widehat{[e2f]}_{tot}}) - \kappa_{17}(1 - p_{10}) \tag{4.3.44}$$

$$p_2 = p_5 \tag{4.3.45}$$

$$p_4 = p_2 p_3 \tag{4.3.46}$$

$$p_7 = p_2 p_6 \tag{4.3.47}$$

If we set $p_i = 1$ in Eqs. (4.3.34)-(4.3.47), we recover the mean-field model proposed in [18]. This limit allows us to determine the parameter values of the stochastic model (see [4] or chapter 2 for details). This equivalence is shown in Table 4.3. The parameter values of the mean-field model [18] are given in Table 4.4

Parameters	Parameters
$k_1 = a_1 * \mathcal{S}$	$k_{11} = b_2$
$k_2 = a_3 * \mathcal{S} * [H]$	$k_{12} = b_3/\mathcal{S}$
$k_3 = a_2$	$k_{13} = d_2 * \mathcal{S}$
$k_5 = J_2 * k_4\mathcal{S} - k_6$	$k_{14} = d_2$
$k_6 = e_1\mathcal{S}/\mathcal{E}$	$k_{15} = d_1/\mathcal{S}$
$k_8 = J_1 * \mathcal{S} - k_9$	$k_{16} = g_1[E2F]_{tot}\mathcal{S}$
$k_9 = e_2/\mathcal{E}$	$k_{17} = g_1$
$k_{10} = b_1$	

Table 4.3: Table showing the equivalence between the parameters of the stochastic model of the G1/S transition (see Table 4.1) and the parameters of the associated mean-field model as formulated by Bedessem & Stephanou [18].

Since we will be interested in the random effects associated to the enzyme-regulated dynamics of SCF, encapsulated in the parameters p_3 and p_6, we have taken $p_i(a) = 1$ for all $i \neq 3, 6$. This corresponds to analysing the marginal distribution integrating out all the stochastic effects associated to all X_i with $i \neq 3, 6$. :

$$\frac{dq_1}{da} = \kappa_1 - \kappa_2 - \kappa_3 q_1 \tag{4.3.48}$$

$$\frac{dq_5}{da} = \frac{\kappa_6 p_3 p_{e_1}(p_c - q_5)}{(p_c - q_5) + \frac{\kappa_5+\kappa_6}{\kappa_4}} - \frac{\kappa_9 p_6 p_{e_2} q_5 q_8}{q_5 + (\kappa_8 + \kappa_9)} \tag{4.3.49}$$

$$\frac{dq_8}{da} = \kappa_{10} m q_{10} \left(1 - \frac{q_9}{\widehat{[e2f]}_{tot}}\right) - \kappa_{11} q_8 - \kappa_{12} q_5 q_8 \tag{4.3.50}$$

$$\frac{dq_9}{da} = \kappa_{13} - \kappa_{14} q_9 - \kappa_{15} q_1 q_9 \tag{4.3.51}$$

$$\frac{dq_{10}}{da} = \kappa_{16} - \kappa_{17} q_{10} \tag{4.3.52}$$

$$q_2 = p_c - q_5 \tag{4.3.53}$$

$$q_4 = \frac{p_{e_1} q_2}{q_2 + \frac{\kappa_5+\kappa_6}{\kappa_4}}, \quad q_3 + q_4 = p_{e_1} \tag{4.3.54}$$

$$q_7 = \frac{p_{e_2} q_5}{q_5 + (\kappa_8 + \kappa_9)}, \quad q_6 + q_7 = p_{e_2} \tag{4.3.55}$$

$$p_3 = \text{cnt.}\, p_6 = \text{cnt.} \tag{4.3.56}$$

Parameter	Value	Reference
a_1	0.51	[18]
a_2	1	[18]
$a_3 H_0$	0.0085	[18]
b_1	0.018	[18]
b_2	0.5	[18]
b_3	1	[18]
d_1	0.2	[18]
d_2	0.1	[18]
e_1	1	[18]
e_2	14	[18]
$m_\star$	10	[224]
$J_3,\ J_4$	0.04	[224]
g_1	0.016	[18]
$[E2F]_{tot}$	1	[18]
$\mathcal{S}$	10	
$\mathcal{E}$	1	
r_{cr}	0.04	

Table 4.4: Parameters values of the mean-field model of the hypoxia regulated G1/S transition proposed by Bedessem & Stephanou [18].

Parameter	Initial condition	Reference
$CycD$	0.1	[18]
SCF	0.9	[18]
Rb	1.0	[18]
$E2F$	0.1	[18]
m	5.0	[18]

Table 4.5: Initial conditions used in simulation system (4.3.48)-(4.3.56) -Figure 4.4

The oxygen dependencies enters the model though the $[H]$ dependent parameter κ_2 (see Table 4.2-4.3).

4.3.5 Stochastic behaviour of the G1/S model

We now proceed to study the behaviour of the stochastic model of the oxygen-regulated G1/S transition. We pay special attention to those aspects in which we observe a departure of the stochastic system from the mean-field behaviour. In particular, we highlight the effects of modifying the relative abundance of SCF-activating and inactivating enzymes, including the ability of inducing oxygen-independent quiescence.

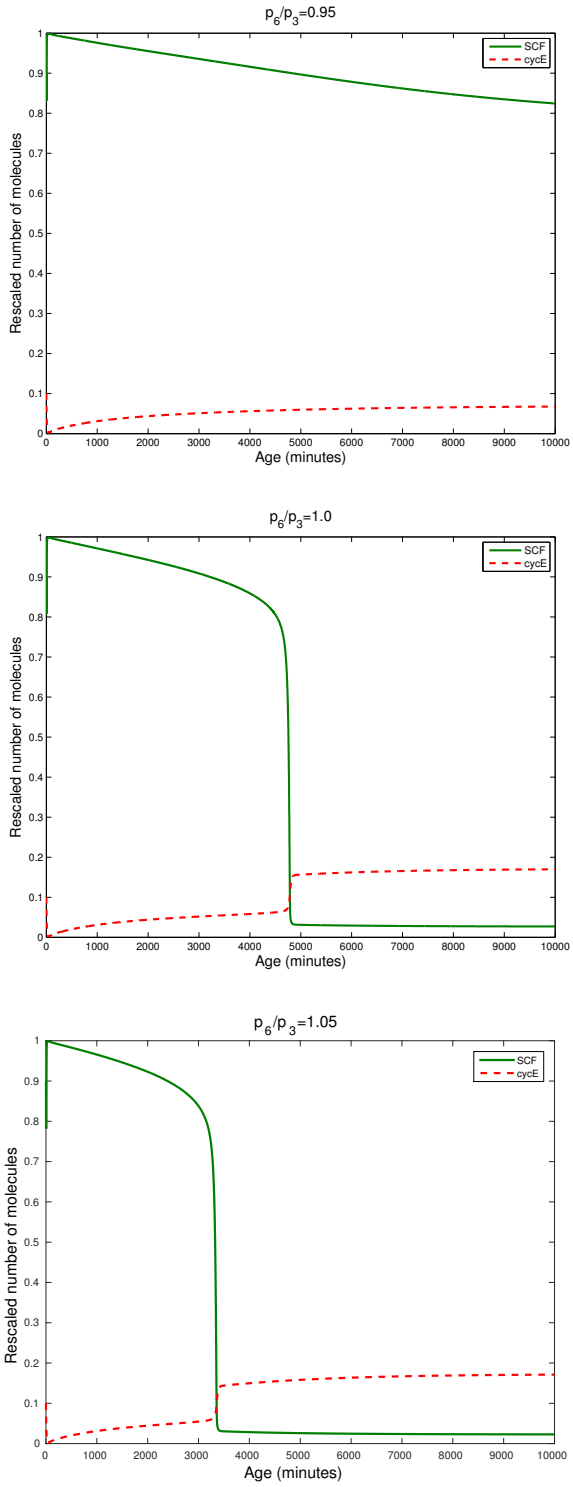

Figure 4.4: Series of plots illustrating how the ratio p_6/p_3, which is associated with the ratio of the number of SCF-inactivating and SCF-activating enzymes, modulates the timing of the G1/S transition. Parameter values as given in Table 4.3. Initial conditions are provided in Table 4.5

The relative abundance of the SCF activating and inactivating enzymes controls the timing of the G1/S transition

In the chapter 2 we have shown that, under SCQSSA conditions, the momenta p_3 and p_6, i.e. the momenta coordinates associated with the SCF-activating and inactivating enzymes, respectively, are determined by the probability distribution of their initial (conserved) number. In particular, if we assume that the initial number of SCF-activating and inactivating enzyme molecules, E_1 and E_2, is distributed over a population of cells following a Poisson distribution with parameter $\mathcal{E}$, we have shown that:

$$p_3 = \frac{e_1}{\mathcal{E}} = p_{e_1},\ p_6 = \frac{e_2}{\mathcal{E}} = p_{e_2}.$$

With this in mind, we can analyse the effect of changing the relative concentration of SCF-activating and inactivating enzymes on the timing of the G1/S transition. Our results are shown in Figs. 4.4 and 4.5. Fig. 4.4 illustrates that, for a fixed oxygen concentration, the G1/S transition is delayed by depriving the system of SCF-activating enzyme: as the ratio $p_3/p_6 = e_1/e_2$ of SCF activating and deactivating enzyme increases, the G1/S transition takes longer to occur. Then, Fig. 4.5 shows that the G1/S transition age $a_{G1/S}(c, p_3, p_6)$ decreases when p_3/p_6 increases. Furthermore, increasing the oxygen concentration c from $c = 0.1$ to $c = 1$ shifts the curve towards lower transition ages $a_{G1/S}(c, p_3, p_6)$. Note that this prediction is beyond the scope of the mean-field limit [18].

Induction of quiescence

In view of the results of Section 4.3.5, we have proceeded to a more thorough analysis of the effect of varying the ratio p_3/p_6, which we recall that, within the SCQSSA, is equal to the ratio between the abundance of SCF-activating and inactivating enzymes, on the behaviour of the SCQSSA system Eqs. (4.3.48)-(4.3.56). In particular, we have investigated the bifurcation diagram of Eqs. (4.3.48)-(4.3.56) with p_3/p_6 as the control parameter. Our results are shown in Fig. 4.6. We observe that, regardless of the value of m, there exists a range of values of the control parameter for which the saddle-node bifurcation, which gives rise to the G1/S transition, does not occur (i.e. only the G1-fixed point is stable). This result implies that depletion of SCF-activating enzyme, or, equivalently, over-expression of SCF-inactivating enzyme can stop cell-cycle progression by locking cells into the so-called G0 state, i.e. quiescence.

These results are confirmed by direct simulation of the stochastic cell-cycle model (Table 4.1) using Gillespie's stochastic simulation algorithm [76], see Fig. 4.7.

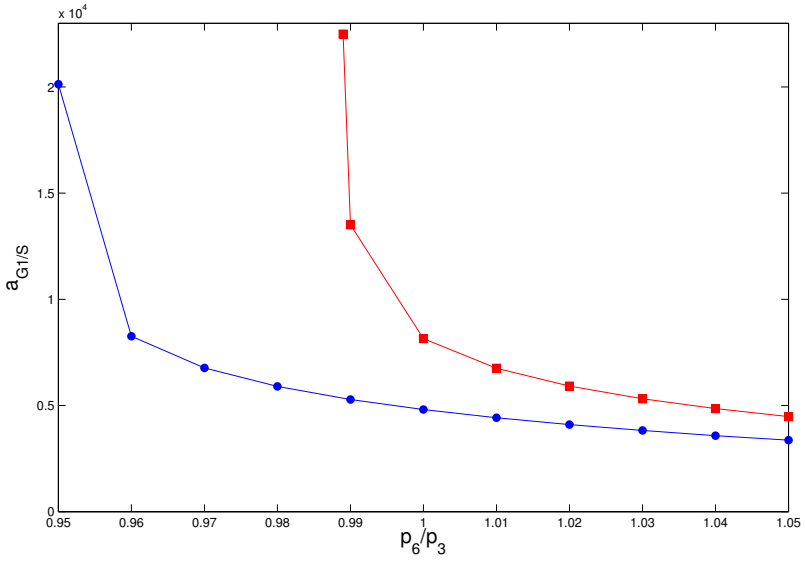

Figure 4.5: Plot showing how the G1/S transition age, $a_{G1/S}(c, p_3, p_6)$, changes as the ratio p_3/p_6, which is determined by the ratio of the (conserved) amounts of SCF activating and inactivating enzymes (chapter 2), varies. We show $a_{G1/S}(c, p_3, p_6)$ for $c = 1$ (blue circles) and $c = 0.1$ (red squares). Parameter values as given in Table 4.3.

4.3.6 Scaling theory of the G1/S transition age

We finish our analysis of the intracellular dynamics by formulating a scaling theory of one of the fundamental quantities in our multi-scale model, namely, the G1/S transition age, $a_{G1/S}(c, p_6, p_3)$, which determines the age-dependent birth rate (see Eq. (4.2.2)). In this section, we will show that, in spite of the complexity of the SCQSSA formulation of the oxygen-dependent cell-cycle progression model (see Eqs. (4.3.48)-(4.3.56)), $a_{G1/S}$ exhibits remarkable regularities with respect to its dependence on the oxygen concentration and the cell-cycle parameters p_6 and p_3. Such regularities hugely simplify our multi-scale methodology.

We can see this regularity in Figure 4.8. Figure 4.8(a) shows $a_{G1/S}$ as a function of the ratio $\left(\frac{c}{c_{cr}(p_6/p_3)} - 1\right)$, for six different values of $\frac{p_6}{p_3} < r_{cr}$, where $r_{cr} = 1.004$ is the critical value. We see that all graphs fall together on a straight line in log-log space, indicating a power-law dependence of $a_{G1/S}$ on $\left(\frac{c}{c_{cr}(p_6/p_3)} - 1\right)$. On the other hand, Figure 4.8(c) shows the dependence of the normalized function $\frac{a_{G1/S}\left(c, \frac{p_6}{p_3}\right)}{a_+(p_6/p_3)}$, on c, for five values $\frac{p_6}{p_3} > r_{cr}$. Here, $a_+(p_6/p_3) = a_{G1/S}(c = 0, p_6/p_3)$. We see that there is good agreement between the five values $\frac{p_6}{p_3}$ for small c, with the disagreement increasing with

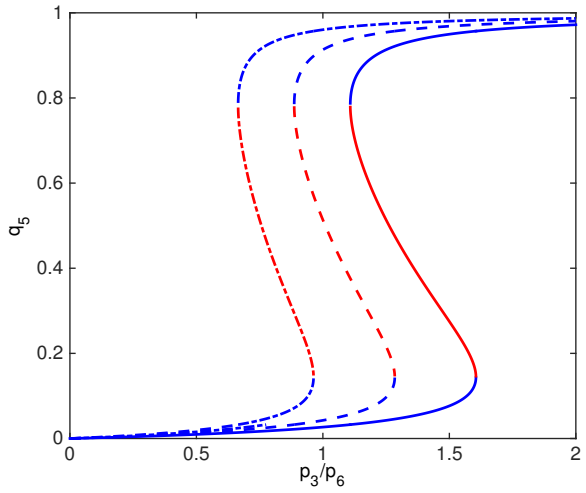

Figure 4.6: This figure shows the bifurcation diagram of the SCQSSA of the stochastic cell-cycle model for different values of the parameter m. The ratio p_3/p_6 is the control parameter. The order parameter is the steady state value of the generalised coordinate associated with active SCF, q_5. Solid line corresponds to $m = 10$, dash lines to $m = 8$ and dotted lines to $m = 6$. Parameter values as give in Table 4.4, $p_i = 1$, $i \neq 3, 6$, $p_c = 1$ and $c = 1$. Blue lines indicate stable steady state and red lines indicate unstable steady state.

increasing c. Thus, a good scaling approximation for $a_{G1/S}$ is given by

$$a_{G1/S}\left(c, \frac{p_6}{p_3}\right) \simeq \begin{cases} a_+\left(\frac{p_6}{p_3}\right) e^{-c/c_0} & \text{if } \frac{p_6}{p_3} > r_{cr} \\ a_-\left(\frac{c}{c_{cr}(p_6/p_3)} - 1\right)^{-\beta} & \text{if } \frac{p_6}{p_3} < r_{cr} \end{cases} \tag{4.3.57}$$

Here, c_0, a_-, and β are constants. According to our analysis of the data presented in Figure 4.8, these constants are given by $c_0 \simeq 1.1$, $a_- \simeq 8.25 \cdot 10^3$ and $\beta \simeq 0.2$. Likewise, $a_+(p_6/p_3)$ is obtained by fitting to the data presented in Figure 4.8(d). The critical oxygen concentration for quiescence c_{cr} can be estimated analytically (with parameter values taken from Table 4.3):

$$c_{cr}\left(\frac{p_6}{p_3}\right) = 1 - \frac{1}{\beta_1} \log\left(\frac{1}{a_3 H_0}\left(a_1 + \frac{a_2 d_2}{d_1 [e2f]_t}\left(1 - \frac{1}{1 - a_0(\frac{p_3}{p_6})^2}\right)\right)\right) \tag{4.3.58}$$

where a_1, a_3, d_1, d_2, $[e2f]_t$, and H_0 are parameters defined in Table 4.3. The parameter a_0 can be estimated as follows. Let $A(c)$ be defined as:

$$A(c) = \left(\frac{p_6}{p_3}\right)^2 \left(1 - \frac{d_2}{(d_2 + d_1 \frac{a_1 - a_3[H]}{a_2})[e2f]_t}\right) \tag{4.3.59}$$

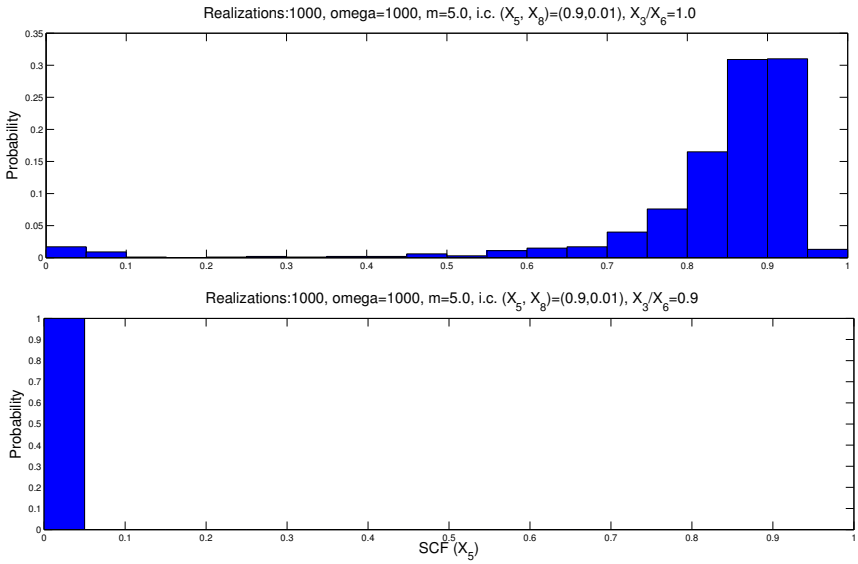

Figure 4.7: Simulation results for the stochastic model of the oxygen-regulated G1/S transition defined by the transition rates given in Table 4.1. We have plotted the probability $P(X_5, T)$, where $T = 100$, with different values of $X_3(\tau = 0)/X_6(\tau = 0)$. 1000 realisations and m=5.0.

where $[H] = a_3 H_0 e^{\beta_1(1-c)}$. $a_0 = A(c_{bif})$, where c_{bif} is the critical value of the oxygen concentration for which the saddle node bifurcation occurs, i.e. the critical value for which the number of real, positive solutions of the equation:

$$e_1(1-x)(J_4+x)(b_2+b_3x) = A(c)e_2b_1m_*[e2f]_t x(1+J_3-x) \tag{4.3.60}$$

goes from 3 to 1. The parameters b_i, e_i, and J_i are defined in Table 4.3

4.4 Cellular scale: Multi-scale Master Equation

We start by summarising the formulation of the multi-scale Master Equation (MSME) for the population dynamics model in terms of an age-structured stochastic process [89]. First, we consider a simple age-dependent birth-and-death process where $n(a,t)$ stands for the number of cells of age a at time t. Both a and t are dimensionless according to the scaling prescribed in Table 4.2. The time variable is $t \to k_7\mathcal{E}\mathcal{S}t$ and a is defined after Eq. (4.3.56). The offspring of such cells with age $a = 0$.

$$P(n, a+\delta a, t+\delta t) = W(n+1,a,t)\delta t P(n+1,a,t) + (1 - W(n,a,t)\delta t)P(n,a,t), \tag{4.4.1}$$

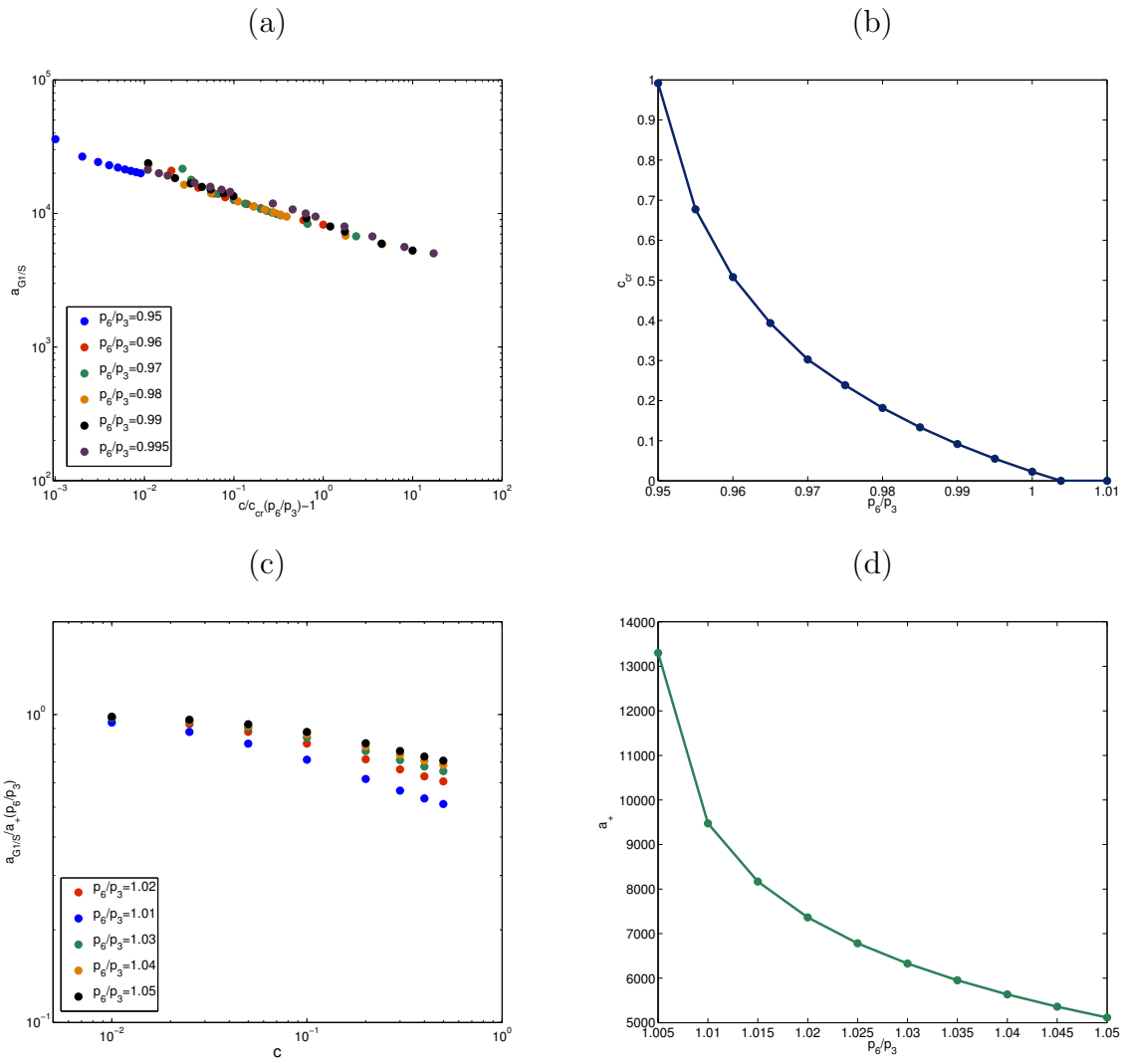

Figure 4.8: Series of plots showing the scaling analysis of the G1/S transition age. Plot (a) shows that below the critical value r_{cr}, which corresponds to the value of the ratio p_6/p_3, above which there is no transition to quiescence (i.e. if $p_6/p_3 > r_{cr}$ the G1/S transition age is finite when $c = 0$), $a_{G1/S}(c, p_6, p_3)$ follows an algebraic decay with a universal p_6/p_3-independent exponent provided that the oxygen, c, is rescaled by the critical oxygen concentration, $c_{cr}(p_6/p_3)$. Plot (c) shows that if, by contrast, $p_6/p_3 > r_{cr}$ $a_{G1/S}(c, p_6, p_3)$ decays exponentially with the oxygen concentration with a characteristic concentration c_0 which, provided p_6/p_3 is larger enough than r_{cr}, is p_6/p_3-independent. Plot (b) shows how c_{cr} varies as p_6/p_3 is changed. Similarly, plot (d) shows how a_+ varies p_6/p_3 changes. Parameter values as given in Table 4.3.

where $W(n(a), a, t) = (\nu + b(a))n(a)$ (see Table 4.6), μ is the (age-independent) death rate, and the age-dependent birth rate, $b(a)$, is given by:

$$b(a) = \begin{cases} 0 \text{ if } q_8(a) < \text{CycE}_T \\ \tau_p^{-1} \text{ if } q_8(a) \geq \text{CycE}_T \end{cases} \tag{4.4.2}$$

where $q_8(a)$ is the generalised coordinate associated with the concentration of CycE which must exceed a threshold value, CycE_T for the cell-cycle to progress beyond the G_1/S transition. Before this transition occurs, cells are not allowed to divide.

Event	Reaction	Transition rate, $W_k(n, a, t)$	r_k
Birth	$n(a) \to n(a) - 1$ $\to n(a = 0) = 2$	$W_1(n, a, t) = b(a)n(a)$	$r_1 = -1$
Death	$n(a) \to n(a) - 1$	$W_2(n, a, t) = \mu n(a)$	$r_2 = -1$

Table 4.6: This table summarises the elementary events involved in the age-dependent birth-and-death process. Cells of age a produce offspring at a rate proportional to the age dependent birth rate, $b(a)$, Eq. (4.4.2). We are assuming that upon cell division both cells are reset to $a = 0$. Therefore, upon proliferation, one cell is removed form the population of age a and two cells are added to the population of age $a = 0$. For simplicity, death is assumed to be age-independent and to occur at a rate proportional to the death rate, μ.

By re-arranging Eq. (4.4.1) and taking the limit $\delta t = \delta a \to 0$, we obtain:

$$\frac{\partial P(n, a, t)}{\partial t} + \frac{\partial P(n, a, t)}{\partial a} = W(n + 1, a, t)P(n + 1, a, t) - W(n, a, t)P(n(a), a, t) \tag{4.4.3}$$

where $W(n, a, t) = W_1(n, a, t) + W_2(n, a, t)$ (see Table 4.6). Eqs. (4.4.3) needs to be supplemented with the appropriate boundary condition at $a = 0$, $P(n_0, a = 0, t)$. We proceed by first considering the number of births that occur within the age group $a = a_j$ during a time interval of length δt. Since we are assuming that our stochastic model is a Markov process where, within each age group, birth and death occur independently and with exponentially distributed waiting times, the number of births, $B(a_j)$, is distributed according to a Poisson distribution:

$$P(B(a_j) = b_j | \delta t) = e^{-b(a_j)n(a_j,t)\delta t} \frac{(b(a_j)n(a_j, t)\delta t)^{b_j}}{b!}$$

The total number of births delivered by the whole population during δt, B, is $B = \sum_{i \in I(t)} B(a_j)$. Its probability density is therefore given by:

$$P(B = b_0) = \sum_{\{b_j\}} \left(\prod_j P_j(B(a_j) = b_j) \right) \delta_{\sum_{j \in I(t)} b_j, b_0} \tag{4.4.4}$$

Since Eq. (4.4.4) is a convolution, using the well-known property of the probability generating function, the generating function associated with $P(B)$, $G_B(p,t)$ is given by [88]:

$$G_B(p,t) = \prod_{j \in I(t)} G_j(p,t),$$

where $G_j(p,t)$ is the generating function associated with $P_j(B(a_j))$:

$$G_j(p,t) = e^{b(a_j)n(a_j)\delta t(p-1)}$$

Therefore, by taking $\delta t = \delta a \to 0$

$$G_B(p,t) = e^{(p-1)\left(\sum_a b(a)n(a)\right)\delta t} \tag{4.4.5}$$

Eq. (4.4.5) determines $P(n_0, a=0, t)$ since $P(n_0, a=0, t) = P(B = n_0/2, t)$ and

$$P(B = b_0, t) = \frac{1}{b_0!} \left. \frac{\partial^{b_0} G_B}{\partial p^{b_0}} \right|_{p=0} \tag{4.4.6}$$

4.4.1 Numerical method

Before proceeding further, we briefly describe the numerical methodology that we use to simulate the stochastic multi-scale model. In essence, the numerical method is an extension of the hybrid stochastic simulation algorithm used in [90] to accommodate the age structure of the cell populations we deal with here [89]. For simplicity, we restrict our description of the algorithm to a homogeneous cell population. Its generalisation to heterogeneous populations composed of a variety of cellular types is straightforward.

Similarly to the procedure described in [89], we start by defining the population vector $\mathcal{N}(t) = \{n_{a_j}(t), j \in \mathcal{J}(t)\}$, where $\mathcal{J}(t)$ is the set of indexes which label all those age groups which, at time t, are represented within the population, i.e. all those age groups such that $n(a = a_j, t) > 0$. Having defined $\mathcal{N}(t)$, we summarise the numerical algorithm:

1. Set initial conditions: $c(t=0) = c_0$, $n(a, t=0) = f(a) \Rightarrow \mathcal{N}(t) = \{f_{a_j}, j \in \mathcal{J}(t=0)\}$, $N(t=0) = \int_0^\infty f(a)da$. We also set the value of the ratio of the SCF-regulating enzymes p_6/p_3.

2. At some later time t, the system is characterised by the quantities $c(t)$, $\mathcal{N}(t)$, $\mathcal{J}(t)$, and $N(t)$

3. Generate two random numbers, z_1 and z_2, uniformly distributed in the interval $(0,1)$

4. Use z_1 to calculate the exponentially distributed waiting time to the next event: $\tau = \frac{1}{a_0(t)} \log \frac{1}{z_1}$ where $a_0(t) = \sum_{j \in \mathcal{J}(t)} \big(W_1(n_{a_j}) + W_2(n_{a_j})\big)$. The rates W_1 and W_2 are given in Table 4.6

5. Update the oxygen concentration at $c(t+\tau)$ by solving the associated ODE Eq. (4.2.1) between $(t, t+\tau)$ taking $c(t)$ as initial condition. We use a 4 stage Runge-Kutta solver

6. Update the age-dependent birth rate for each $j \in \mathcal{J}$, $b(a) = \tau_p^{-1} H\left(a - a_{G1/S}(c, \frac{p_6}{p_3})\right)$. The quantity $a_{G1/S}(c(t+\tau), \frac{p_6}{p_3})$ is given by Eq. (4.3.57)

7. Use z_2 to determine which event occurs (i.e. birth or death within the jth sub-population) at time $t+\tau$: event l occurs with probability

$$\sum_{k=1}^{l} \mathcal{W}_k \leq z_2 a_0(t) < \sum_{k=l+1}^{J} \mathcal{W}_k,$$

   where $J = \mathrm{card}(\mathcal{J}(t))$ and $\mathcal{W}_{2(j-1)+1} = W_1(n_{a_j})$ and $\mathcal{W}_{2(j-1)+2} = W_2(n_{a_j})$

8. If the randomly chosen event is $l = 2(j-1)+1$ (i.e. cell proliferation within age group j), then $n_{a_j+\tau}(t+\tau) = n_{a_j}(t) - 1$, $n_{a_k+\tau}(t+\tau) = n_{a_k}(t)$ for all $k \neq j$, and $n_{a=0}(t+\tau) = n_{a=0}(t) + 2$

9. If the randomly chosen event is $l = 2(j-1)+2$ (i.e. cell death within age group j), then $n_{a_j+\tau}(t+\tau) = n_{a_j}(t) - 1$, $n_{a_k+\tau}(t+\tau) = n_{a_k}(t)$ for all $k \neq j$

10. Finally, we update the set $\mathcal{J}(t+\tau)$, i.e. the set of age groups for which $n_{a_j+\tau}(t+\tau) > 0$

11. Steps 3 to 10 are repeated until some stopping condition (e.g. $t \geq T$) is satisfied

Note that Step 5 does not involve the use a stochastic method of integration of the ODE which rules the time evolution of the oxygen concentration, Eq. (4.2.1). This is due to the fact that, within the time interval $(t, t+\tau]$, the population stays constant, so that Eq. (4.2.1) can be solved by means of a non-stochastic solver.

4.4.2 Steady-state of a homogeneous population: mean-field analysis

Before proceeding further, in order to check the numerical algorithm proposed in Section 4.4.1, we analyse how it compares with results regarding the steady-state of the mean-field limit of a homogeneous (i.e. composed by one cellular type only) population [105]. The mean-field equations associated with the stochastic multi-scale model are:

$$\frac{dc}{dt} = \bar{S} - kN(t)c,$$
$$\frac{\partial n(a,t)}{\partial t} + \frac{\partial n(a,t)}{\partial a} = -(\nu + b(a))n(a,t) \tag{4.4.7}$$

with boundary condition:

$$n(a=0,t) = 2\int b(a)n(a,t)da$$

and birth rate given by:

$$b(a) = \tau_p^{-1}\mathcal{H}\left(a - a_{G1/S}(c, p_6/p_3)\right)$$

with $a_{G1/S}(c, p_6/p_3)$ is given by Eq. (4.3.57)

According to [105], in order to ascertain whether a steady-state solution, i.e. whether the system settles onto an age distribution where the proportion of cells of each age does not change, we seek for a separable solution: $n(a,t) = A(a)T(t)$. Defining $\mu(a) = \nu + b(a)$, we obtain:

$$\frac{1}{T}\frac{dT}{dt} = -\frac{1}{A}\left(\frac{dA}{da} + A\mu(a)\right) = \sigma \tag{4.4.8}$$

with σ =cnt. to be determined. $n(a,t)$ is therefore given by:

$$n(a,t) = A(a=0)\exp\left(\sigma(t-a) - \int_0^a \mu(y)dy\right) \tag{4.4.9}$$

The value of the parameter σ is obtained by means of the characteristic equation obtained by introducing Eq. (4.4.9) with $a = 0$ into the boundary condition:

$$1 = 2\int_0^\infty b(a)\exp\left(-\sigma a - \int_0^a \mu(y)dy\right)da \tag{4.4.10}$$

After some algebra, the characteristic equation Eq. (4.4.10) reads:

$$2\frac{\tau_p^{-1}e^{-(\sigma+\nu)a_{G1/S}}}{\sigma + \nu + \tau_p^{-1}} = 1 \tag{4.4.11}$$

From Eq. (4.4.11) we obtain the condition for the system to be in equilibrium, i.e. $\sigma = 0$. Substituting $\sigma = 0$ in Eq. (4.4.10):

$$R_0 \equiv 2\frac{\tau_p^{-1}e^{-\nu a_{G1/S}}}{\nu + \tau_p^{-1}} = 1 \tag{4.4.12}$$

where R_0 is the average number of offspring per cell at equilibrium: if $R_0 > 1$ the system grows exponentially, $R_0 < 1$ the system dwindles, and if $R_0 = 1$ the population

remains constant. The equilibrium condition $R_0 = 1$ allows us to find the value of $a_{G1/S}$ for which such equilibrium exists:

$$a_{G1/S}(c_\infty, p_6/p_3) = -\frac{1}{\nu}\log\left(\frac{\tau_p(\nu + \tau_p^{-1})}{2}\right) \tag{4.4.13}$$

For this quantity to be positive $\tau_p\nu < 1$ must hold. This condition states that for a steady state be reached, the average waiting time to division after the G1/S transition, τ_p, must be smaller than the average life span of the cell, ν^{-1}. Eq. (4.4.13) determines the stationary value of the oxygen concentration, c_∞.

The long-time dynamics of Eqs. (4.4.7) can therefore be summarised as follows: given the values of τ_p, ν, and the cell-cycle parameters (see Table 4.3), the population evolves and consumes oxygen until, the oxygen concentration reaches a steady value c_∞. At this point, the population of resident cells has settled onto a steady state where its age structure does not change. The total number of cells is also constant and given by (see Eqs. (4.4.7)):

$$N_\infty = \frac{\bar{S}}{kc_\infty} \tag{4.4.14}$$

In order to verify the age-structured SSA proposed in Section 4.4.1, we compare its results with the mean-field predictions, which should be in agreement with the stochastic behaviour of the system for large values of the carrying capacity, N_∞. Results are shown in Fig. 4.9. We observe that, as predicted by our steady-state analysis, the stochastic simulations show how the resident population goes through an initial (oxygen-rich) phase of exponential growth. As the population grows, oxygen is depleted and the resident population eventually saturates onto a number of cells which fluctuates around the mean-field prediction of the carrying capacity (Eq. (4.4.14)).

Further verification of the validity of our numerical methodology is provided in Fig. 4.10. Our mean-field theory predicts that, everything else remaining unchanged, the average steady-state population should increase linearly with the rate of oxygen delivery, S (see Eq. 4.4.14). By contrast, the average equilibrium oxygen concentration does not depend on S, as shown in Eq. (4.4.13), and, consequently, it should stay constant upon increasing the rate of oxygen delivery. Fig. 4.10 shows that our simulations agree with these mean-field predictions.

4.5 Quasi-neutral competition within heterogeneous populations

A problem of fundamental importance in several biological and biomedical contexts is that of a population composed by a heterogeneous mixture of coexisting cellular

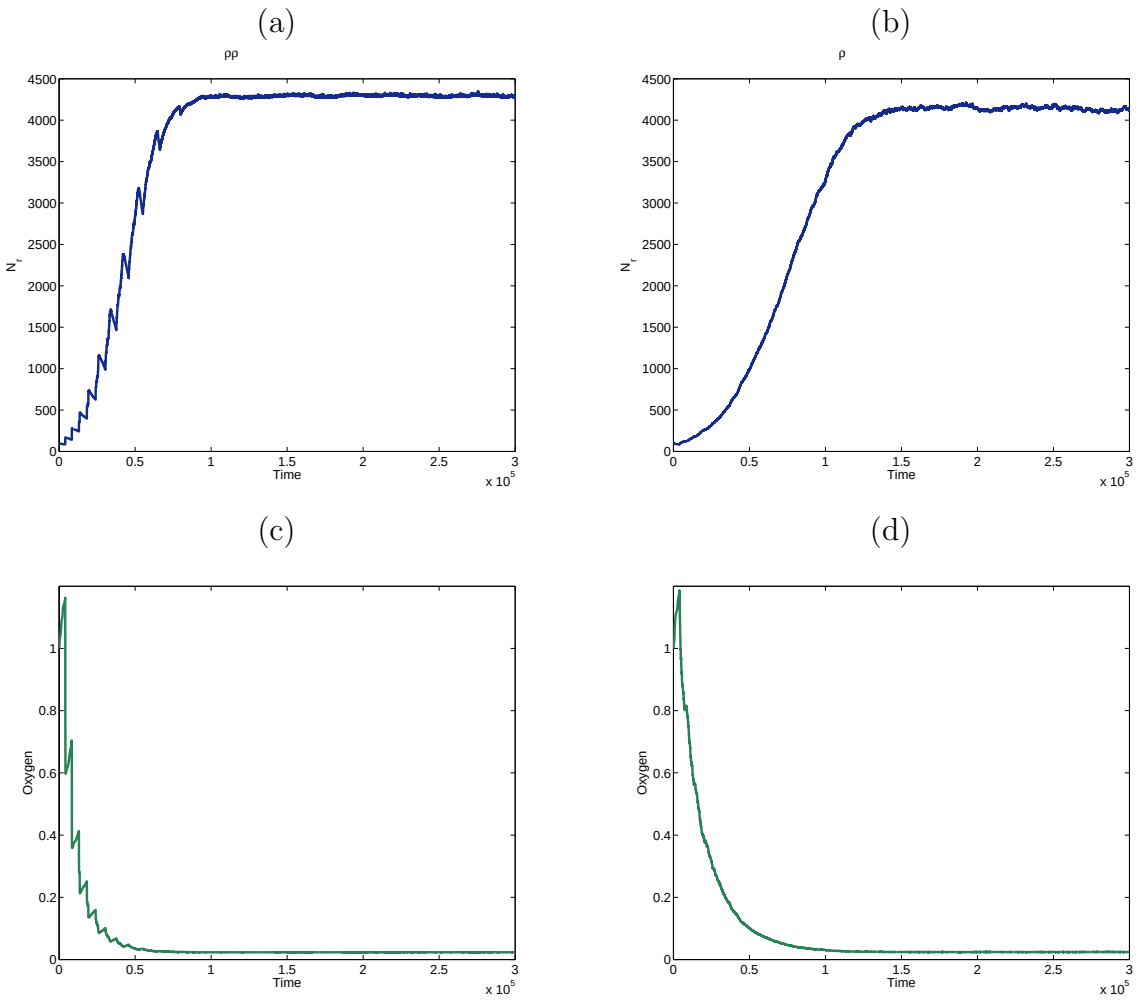

Figure 4.9: Plots showing simulation results of the stochastic multi-scale dynamics of a cell population. These plots show how, in agreement with our steady-state analysis, the population evolves until it reaches a steady-state where the population of resident cells fluctuates around its associated carrying capacity Eq. (4.4.14). Colour code: blue lines show the total resident cell population at time t, $N(t)$ (panels (a) & (b)). Green lines (panels (c) & (d)) show the associated oxygen concentration, $c(t)$. The results shown in this figure correspond to a single realisation of the process. Parameter values: $\nu = 2.4 \cdot 10^{-4}$, $\bar{S} = 1.57 \cdot 10^{-2}$, $k = 1.57 \cdot 10^{-4}$, $\tau_p = 2.4 \cdot 10^{1}$ in panels (a) & (c), and $\tau_p = 2.4 \cdot 10^{3}$ in panels (b) & (d).

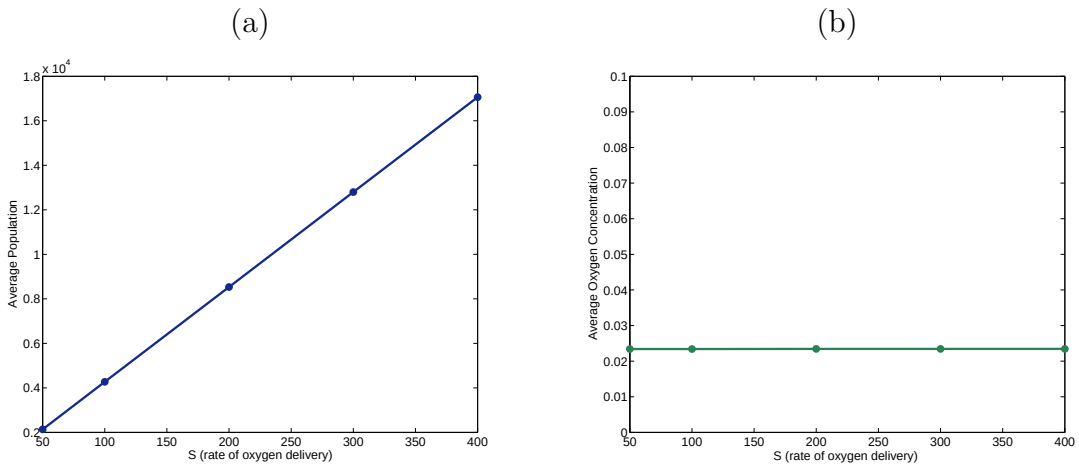

Figure 4.10: Plots showing simulation results of the stochastic multi-scale dynamics of a cell population. These plots show how, in agreement with our steady-state analysis, the average population at equilibrium increases linearly as the rate of oxygen delivery, $\bar{S}$, is changed (plot (a)). Also, in accordance with our mean-field theory, the average, steady-state oxygen concentration remains unchanged as $\bar{S}$ increases. Parameter values: $\nu = 2.4 \cdot 10^{-4}$, $k = 1.57 \cdot 10^{-4}$, $\tau_p = 2.4 \cdot 10^1$ in panels (a) & (c), and $\tau_p = 2.4 \cdot 10^3$ in panels (b) & (d). Average has been performed over 100 realisations.

types. A particularly relevant example of such situation is that of cancer, where heterogeneity within the cancer cell population is assumed to be a major factor in the evolutionary dynamics of cancer as well as the emergence of drug resistance [70, 80, 87, 155]. Within this context, we are interested in (i) exploring the stability of a co-existing heterogeneous population, and (ii) the effects such heterogeneity has on the long-term effects a cell-cycle dependent therapy.

The origins of heterogeneity of cancer cell populations is normally attributed to genetic variability arising from chromosomal instability and increased mutation rate [155]. Our discussion of the model of the G1/S transition (see Section 4.3) suggests a different source of heterogeneity associated with stochastic effects due to intrinsic fluctuations. We have shown, by means of both the SCQSSA analysis and stochastic simulations, that the relative abundance of SCF-regulating enzymes, which is quantified in our analysis by the ratio p_6/p_3 (see Sections 4.3.5, 4.3.6 and chapter 2). In Section 4.3.5 we have shown that the timing of the G1/S transition, and, consequently, the overall birth rate is strongly affected by changes in this quantity. In view, of this we associate heterogeneity to a distribution of the abundance of such enzymes, whereby we associate cell phenotypes with different values of the ratio p_6/p_3. We further assume that this heterogeneity is hereditary, i.e. daughter cells inherit the value of the ratio p_6/p_3 from their mother.

4.5.1 Competition between two sub-populations

To proceed further, we consider the case of the birth-and-death dynamics of a heterogeneous population composed by two sub-populations, $n_1(a,t)$ and $n_2(a,t)$, competing by a common resource, $c(t)$, which regulates the rate of progression of the cell-cycle of each cell type. The stochastic dynamics of the whole population is determined by the associated multi-scale master equation:

$$\begin{aligned}&\frac{\partial P(n_1,n_2,a,t)}{\partial t}+\frac{\partial P(n_1,n_2,a,t)}{\partial a}=\\&=W_1(n_1+1,n_2,a,t)P(n_1+1,n_2,a,t)+W_2(n_1,n_2+1,a,t)P(n_1,n_2+1,a,t)\\&-(W_1(n_1,n_2,a,t)+W_2(n_1,n_2,a,t))P(n_1,n_2,a,t)\end{aligned} \tag{4.5.1}$$

where $W_1(n_1,n_2,a,t)=(\nu_1+b_1(a))n_1(a,t)$ and $W_2(n_1,n_2,a,t)=(\nu_2+b_2(a))n_1(a,t)$, ν_1 and $b_1(a)$ are the (age-independent) death rate and the birth rate of the resident population, and ν_2 and $b_2(a)$ are the (age-independent) death rate and the birth rate of the invader. The quantities $b_1(a)$ and $b_2(a)$ are determined by the (oxygen-dependent) rate of cell-cycle progression of each sub-population:

$$b_1(a)=\tau_{p_1}^{-1}\mathcal{H}\left(a-a_{G1/S}(c,p_{6_1}/p_{3_1})\right), \tag{4.5.2}$$

$$b_2(a)=\tau_{p_2}^{-1}\mathcal{H}\left(a-a_{G1/S}(c,p_{6_2}/p_{3_2})\right) \tag{4.5.3}$$

$a_{G1/S}(c,p_6/p_3)$ is given by Eq. (4.3.57). The concentration of resource (oxygen), $c(t)$, is determined by the following ODE:

$$\frac{dc}{dt}=\bar{S}-(k_1N_1+k_2N_2)c \tag{4.5.4}$$

where $N_i(t)=\int_0^\infty n_i(a,t)da$ for $i=1,2$.

The associated initial conditions are given by:

$$P(n_1,n_2,a,t=0)=\delta(n_1(a,t=0)-n_{0_1}(a))\delta(n_2(a,t=0)-n_{0_2}(a))$$

In the remaining of this Section we will consider two cellular populations, resident and invader. Each of these phenotypes are determined in terms of the values four parameters. The resident cells are characterised by two population-dynamics parameters, namely, the average time to division after the G1/S transition, τ_{p_1}, and the death rate, ν_1. We consider two further parameters, p_{3_1} and p_{6_1}, associated with the cell-cycle progression dynamics of the resident cells (see Section 4.3.4). Similarly, the invader is characterised by the corresponding parameters: τ_{p_2}, ν_2, p_{3_2} and p_{6_2}

4.5.2 Mean-field coexistence versus quasi-neutral stochastic competition

We proceed to analyse the conditions under which two populations are capable of long-term coexistence. In particular, we analyse a scenario in which the mean-field description predicts long term coexistence between within a heterogeneous population leads to mutual exclusion of all strands but one through so-called quasi-neutral stochastic competition [90, 133, 144].

The starting point for our study is the mean-field analysis carried out in Section 4.4.2. According to these results, (mean-field) populations evolve until a concentration of oxygen, c_∞, is reached so that the associated replication number $R_{0_i}(c_\infty) = 1$, $i = 1, 2$. The replication number of either population is given by:

$$R_{0_1} = 2\frac{\tau_{p_1}^{-1} e^{-\nu_1 a_{G1/S_1}(c_\infty, p_{6_1}/p_{3_1})}}{\nu_1 + \tau_{p_1}^{-1}} \text{ and } R_{0_2} = 2\frac{\tau_{p_2}^{-1} e^{-\nu_2 a_{G1/S_2}(c_\infty, p_{6_2}/p_{3_2})}}{\nu_2 + \tau_{p_2}^{-1}}$$

Therefore, our theory predicts that, provided that there exists c_∞ such that:

$$\begin{aligned} a_{G1/S_1}(c_\infty, p_{6_1}/p_{3_1}) &= -\frac{1}{\nu_1}\log\left(\frac{\tau_{p_1}(\nu_1 + \tau_{p_1}^{-1})}{2}\right), \\ a_{G1/S_2}(c_\infty, p_{6_2}/p_{3_2}) &= -\frac{1}{\nu_2}\log\left(\frac{\tau_{p_2}(\nu_2 + \tau_{p_2}^{-1})}{2}\right), \end{aligned} \tag{4.5.5}$$

is satisfied, long-term coexistence ensues, since the whole system (oxygen, resident and invader) is able to evolve to a state where both populations are in equilibrium (in the sense that $R_{0_i}(c_\infty) = 1$ for both populations) with the same concentration of oxygen. Furthermore, the number of resident cells, N_1, and the number of invaders, N_2, satisfy:

$$k_1 N_1 + k_2 N_2 = \frac{\bar{S}}{c_\infty} \tag{4.5.6}$$

Thus, the mean-field theory predicts that there exist a continuous of fixed points. The eventual convergence on to a particular point along the line of fixed points Eq. (4.5.6) depends on the initial conditions. Eq. (4.5.6) can be further simplified by assuming $k_1 = k_2 = k$, in which case $N_1 + N_2 = K$, where $K \equiv \bar{S}/(kc_\infty)$ is the carrying capacity.

This mean-field scenario is the basis for the study of the long-term stochastic dynamics of two populations which satisfy Eqs. (4.5.5), which are equivalent to $R_{0_1} = R_{0_2} = 1$. The reproduction number is the average number of offspring per cell. We know from elementary considerations [88] that the value of such quantity allows us to classify birth-death/branching processes. If $R_0 > 1$ the population grows, on average, exponentially and has a finite probability of eventual survival. In this case, the process is referred to as super-critical. If $R_0 < 1$ the population undergoes

exponential decline (on average) and the extinction probability is equal to 1. The last case, in which $R_0 = 1$, the so-called critical case, the population, on average, stays constant. However, due to effects of noise, extinction occurs with probability 1, with the probability of survival up to time t asymptotically tends to $P_S(t) \sim t^{-1}$ [130]. In our case, both the resident and the invader undergo a critical stochastic dynamics, where, once the steady state has established itself, the population evolves very close to the mean-field line of fixed points $N_1 + N_2 = K$ until fixation of one of the species (and, consequently, extinction of the other) occurs.

In order to numerically check this scenario, we could proceed to estimate the survival probability at time t, $P_S(t)$. However, since this quantity exhibits a fat-tail behaviour, this would be computationally costly. A more efficient method is to resort to the asymptotic study of the extinction time with system size, which in this case can be identified with the carrying capacity, K [100]. Typically, a quasi-neutral competition is associated with an algebraic dependence of the average extinction time of either population, T_E, on the system size, in this case determined by the carrying capacity, K [49, 133, 144]. In Fig. 4.11 we plot simulation results for the competition between two identical populations. In particular, we study how the average extinction time of either population, T_E, varies as the carrying capacity is changed. We observe that this quantity exhibits a linear dependence on the carrying capacity:

$$T_E \sim K, \tag{4.5.7}$$

Our scenario produces the same qualitative results as Lin et al. [144] and Kogan et al. [133] who studied the average extinction time of birth-and-death processes engaged in quasi-neutral competition. In both papers, the average extinction time was reported to depend linearly on system size.

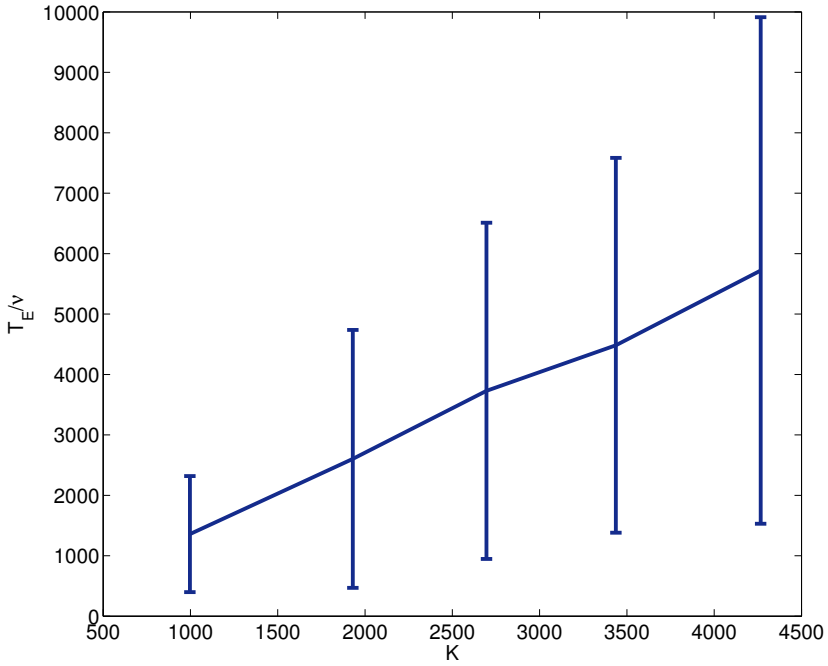

Figure 4.11: Simulation results corresponding to the competition between the sub-populations of a heterogeneous populations. We show how the average extinction time of either population, T_E, varies as the carrying capacity, K, changes. We observe that the dependence is linear. For simplicity, the two sub-populations are assumed to be identical (i.e. with the same characteristic parameter values for both the intracellular dynamics (cell-cycle) and the population-level dynamics (birth and death rates)). The carrying capacity $K = \frac{\bar{S}}{k_1 c_\infty}$ by varying the death rates of both populations. The values of are $\nu = 1.0 \cdot 10^{-4}$, $0.83 \cdot 10^{-4}$, $0.73 \cdot 10^{-4}$, $0.625 \cdot 10^{-4}$, $0.417 \cdot 10^{-4}$, which correspond to $K = 0.9969 \cdot 10^3, 1.9301 \cdot 10^3, 2.6956 \cdot 10^3, 3.4367 \cdot 10^3, 4.2661 \cdot 10^3$, respectively. Averages are done over 500 realisations of the hybrid stochastic model.

4.6 Study of the effects of cell-cycle-dependent therapy

In Section 4.5 we have analysed how the dependence of the cell-cycle progression on the concentration of SCF-activating and SCF-inactivating enzymes allows us to engineer heterogeneous populations where invasion and coexistence may occur. In this Section, we further explore the ability of inducing quiescence by varying the ratio between SCF-activating and SCF-inactivating enzymes, this time in connection with the ability of such populations to withstand the effects of cell-cycle-dependent therapy

[22, 64, 179, 180].

In particular, we consider a scenario where two cellular populations coexist. Initially, one of these populations consists of a set of cells actively progressing through the cell-cycle which have reached a steady state characterised by the mean-field equilibrium Eqs. (4.4.12)-(4.4.14). The second population consists of quiescent cells whose cell-cycle is locked into the G0 phase and therefore do not proliferate. These cells are further assumed to undergo apoptosis at a very slow rate. More specifically, the ratio SCF-activating and SCF-inactivating enzymes in the quiescent cell population is such that, for the steady-state level of oxygen for the active cells (see Eq. (4.4.13)), cells are locked into the G1-fixed point (see Fig. 4.6).

In this Section we show that the presence of a quiescent population within a heterogeneous population may lead to resistance to cell-cycle-dependent therapy. In particular, we show that, whereas such therapies effectively reduce or even eradicate the active cell population, the feedback between the therapy-induced decrease in cell numbers and the associated increase in oxygen availability can yield to the quiescent population to enter the active state and thus regrow the population. In this sense, we claim that the quiescent population has a *stem-cell-like* effect whereby, under the action of therapeutic agent, can repopulate the system [7].

4.6.1 Mean-field analysis

We start our mean field analysis by considering a heterogeneous population composed by cells of two types: type 1 and type 2 cells. Type 1 consists of cells with values of $p_3 \equiv p_{3_1}$ and $p_6 \equiv p_{6_1}$ (see Section 4.3.4) such that cells are actively progressing through the cell-cycle. Type 2 cells are characterised by values of $p_3 \equiv p_{3_2}$ and $p_6 \equiv p_{6_2}$ so that they are locked in G0 (i.e. not cycling). The associated mean-field dynamics are given by:

$$\frac{dc(t)}{dt} = \bar{S} - k_1(N_1 + N_2)c(t), \tag{4.6.1}$$

$$\frac{\partial n_1}{\partial t} + \frac{\partial n_1}{\partial a} = -(\nu_1 + b_1(a))n_1 \tag{4.6.2}$$

$$\frac{\partial n_2}{\partial t} + \frac{\partial n_2}{\partial a} = -\nu_2 n_2 \tag{4.6.3}$$

with boundary conditions:

$$n_1(a=0,t) = 2\int b_1(a)n_1(a,t)da, \quad n_2(a=0,t) = 0.$$

$N_1(t)$ and $N_2(t)$ are the total cell population of type 1 and type 2 cells, respectively:

$$N_1(t) = \int n_1(a,t)da,\ N_2(t) = \int n_2(a,t)da.$$

For simplicity, we assume that both populations consume oxygen at the same rate, k_1. We further assume that $\nu_2 \ll \nu_1$, i.e. type 2 (quiescent) cells die at a much slower rate than type 1 (active) cells. In Section 4.4.2, we have already analysed under which conditions Eqs. (4.6.1)-(4.6.3) reach a steady state:

$$R_{0_1} \equiv 2\frac{\tau_{p_1}^{-1} e^{-\nu_1 a_{G1/S_1}}}{\nu_1 + \tau_{p_1}^{-1}} = 1 \tag{4.6.4}$$

where R_{0_1} is the average number of offspring per cell of type 1 at equilibrium. The associated equilibrium value of a_{G1/S_1} is then given by:

$$a_{G1/S_1}(c_\infty, p_{6_1}/p_{3_1}) = -\frac{1}{\nu_1}\log\left(\frac{(\tau_{p_1}\nu_1 + 1)}{2}\right) \tag{4.6.5}$$

which determines the steady-state value of the oxygen concentration c_∞. At this point, the population of resident cells has settled onto a steady state where its age structure does not change. The total number of cells is also approximately constant and given by:

$$N_{1_\infty} + N_2 \simeq \frac{\bar{S}}{k_1 c_\infty} \tag{4.6.6}$$

where we have used the fact that $\nu_2 \ll \nu_1$. The cell-cycle parameters p_{3_2} and p_{6_2} have been chosen so that, for $c = c_\infty$, $a_{G1/S_2}(c_\infty, p_{6_2}/p_{3_2}) \to \infty$, i.e. type 2 cells are initially locked into G0 (see Fig. 4.6).

Once the population reaches this therapy-free quasi-equilibrium state, we assume that a therapy which only acts on proliferating cells is administered. Examples of such therapies abound in cancer treatment and can take the form of cell-cycle specific drugs or radiotherapy [22, 64, 179, 180]. We characterise the efficiency of the therapy by the so-called survival fraction, F_S, i.e. the percentage of cells which survive the prescribed dose. For example, in radiotherapy F_S is usually taken to be given by the linear quadratic model: $\log F_S = -(\alpha D + \beta D^2)$ where D stands for the radiation dosage expressed in Grays and α and β are cell type-specific parameters. In the present context, we do not specify any particular form of therapy and we simply take $F_S \in [0, 1)$. Initially, the therapy only affects type 1 cells (since type 2 are not proliferating). Therapy affects the birth and death rates of the type 1 population, which now read:

$$b_{T_1}(a) = \tau_{p_1}^{-1} F_S \mathcal{H}(a - a_{G1/S_1}(c, p_{3_1}, p_{6_1})) = F_s b_1(a) \tag{4.6.7}$$

$$\nu_{T_1}(a) = \nu_1 + (1 - F_s)b_1(a) \tag{4.6.8}$$

The resulting mean-field equation is given by:

$$\frac{\partial n_1}{\partial t} + \frac{\partial n_1}{\partial a} = -(\nu_1 + b_1(a))n_1 \tag{4.6.9}$$

$$n_1(a=0,t) = 2F_S \int b_1(a)n_1(a,t)da \tag{4.6.10}$$

The action of the therapeutic agent on the active population initially induces a decline of the population, which, in turn, involves an increase in the available oxygen concentration. The latter has the effect of accelerating the rate of progression of type 1 cells through the cell cycle. In the absence of the quiescent population, eventually both effects would find a balance and the population of active cells would settle onto a new equilibrium characterised by:

$$R_{0_{T_1}} \equiv 2F_S \frac{\tau_{p_1}^{-1} e^{-\nu_1 a_{G1/S_{T_1}}}}{\nu_1 + \tau_{p_1}^{-1}} = 1 \tag{4.6.11}$$

or, equivalently:

$$a_{G1/S_1}(c_{T_{\infty_1}}, p_{3_1}, p_{6_1}) = -\frac{1}{\nu_1}\left(-\log F_S + \log\left(\frac{(\tau_{p_1}\nu_1 + 1)}{2}\right)\right) \tag{4.6.12}$$

where $c_{T_{\infty_1}}$ is the equilibrium oxygen concentration for the type 2 population with therapy. Note that $a_{G1/S_1}(c_{T_{\infty_1}}, p_{3_1}, p_{6_1}) < a_{G1/S_1}(c_\infty, p_{6_1}/p_{3_1})$ and therefore $c_{T_{\infty_1}} > c_\infty$ since $a_{G1/S}$ is a decreasing function of the oxygen concentration. Re-oxygenation during cell-cycle dependent therapy, in particular, radiotherapy, has been predicted by other models [124].

Consider now the effect of this process on the type 2 cell population which is initially quiescent. We know that hypoxia-induced arrest of the cell cycle is reversible [5, 18], i.e. upon increase of the concentration of oxygen quiescent cells may re-enter the cell cycle and become proliferating. Re-entry of quiescent cells into the cell cycle is predicated upon a sufficient increase in the oxygen contraction: $c > c_{H_2}(p_{3_2}, p_{6_2})$, where the critical oxygen concentration for type 2 cells, c_{H_2}, depends on the momenta p_{3_2} and p_{6_2} or, equivalently, on the concentration of SCF-activating and SCF-inactivating enzymes. Taking this property into account, one can devise a scenario in which $c_{T_{\infty_1}} > c_{H_2}(p_{3_2}, p_{6_2}) > c_\infty$, i.e the initial oxygen concentration is such that type 2 cells are quiescent, but, as the therapy is administered and proceeds to act upon the type 1 cells, the oxygen concentration increases until it reaches its critical re-entry concentration. At this point, type 2 cells abandon quiescence and become active and competition between type 1 and type 2 cells ensues.

In order to assess the long-time behaviour of the system, we first study the equilibrium of the type 2 cell population upon re-entry into cell-cycle progression. Its mean-field dynamics is given by:

$$\frac{\partial n_2}{\partial t} + \frac{\partial n_2}{\partial a} = -(\nu_2 + b_2(a))n_1 \tag{4.6.13}$$

$$n_2(a=0,t) = 2F_S \int b_2(a) n_2(a,t) da \tag{4.6.14}$$

where $b_2(a) = \tau_{p_2}^{-1}\mathcal{H}(a - a_{G1/S_2}(c, p_{3_2}, p_{6_2}))$ and c is determined by Eq. (4.6.1). Recall that, upon re-entering cell-cycle progression, type 2 cells are no longer immune to the therapy. Although in general the survival fraction is type-dependent, for simplicity we assume that F_S has the same value for both cell types. The equilibrium condition is once again given in terms of the associated reproduction number, i.e. $R_{0_{T_2}} = 1$ which yields:

$$a_{G1/S_2}(c_{T_{\infty_2}}, p_{3_2}, p_{6_2}) = -\frac{1}{\nu_2}\left(-\log F_S + \log\left(\frac{(\tau_{p_2}\nu_2 + 1)}{2}\right)\right) \tag{4.6.15}$$

Since $\nu_2 \ll \nu_1$, we have that $a_{G1/S_2}(c_{T_{\infty_2}}, p_{3_2}, p_{6_2}) \gg a_{G1/S_1}(c_{T_{\infty_1}}, p_{3_1}, p_{6_1})$ (see Eqs. (4.6.12) and (4.6.15)). The latter inequality implies that the equilibrium oxygen concentration for type 2 cell, $c_{T_{\infty_2}}$, is such that $c_{T_{\infty_2}} < c_{T_{\infty_1}}$. It is easy to argue that, in these conditions, the type 2 population out-competes the type 1 cells: for $c_{T_{\infty_2}} < c < c_{T_{\infty_1}}$, the growth rate of type 1 cells is positive whereas the growth rate of the type 2 cell population is negative (see Eq. (4.4.11)). This implies that, upon application of therapy and provided that $c_{T_{\infty_1}} > c_{H_2}(p_{3_2}, p_{6_2}) > c_\infty$ is satisfied, the type 1 population declines and it is replaced by the type 2 population.

4.6.2 Critical dosage

In order to gain some degree of control over the behaviour described in the previous section, it is useful to provide an estimate of the critical dosage above which therapy-induced re-oxygenation is capable of activating quiescent cells. We characterise the therapy dose by means of the critical survival fraction, F_{S_C}. Recall that the characteristic equation for the oxygen-dependent growth rate, $\sigma_1(c)$, of the population of active cells is given by:

$$2F_S \frac{\tau_{p_1}^{-1} e^{-(\sigma_1+\nu_1)a_{G1/S_1}(c)}}{\sigma_1 + \nu_1 + \tau_{p_1}^{-1}} = 1 \tag{4.6.16}$$

In order to activate the quiescent population the oxygen concentration must raise above the critical value $c_{H_2}(p_{3_2}, p_{6_2})$. For the oxygen concentration to grow above this threshold $\sigma_1(c_{H_2}) < 0$ so that the active cell population continues to decline thus allowing the oxygen concentration to keep on raising. Therefore the critical value F_{S_C} is such that $\sigma_1(c_{H_2}) = 0$, i.e.

$$F_{S_C} = \frac{\nu_1 + \tau_{p_1}^{-1}}{2\tau_{p_1}^{-1} e^{-\nu_1 a_{G1/S_1}(c_{H_2}(p_{3_2}, p_{6_2})}} \tag{4.6.17}$$

If $F_S < F_{S_C}$ the decrease in the active cell population is enough to provide enough oxygen for the quiescent population to become active.

This analysis implies that in heterogeneous populations which include quiescent subpopulations, the effect of cell-cycle-dependent therapy does not eradicate the population. Rather the following two scenarios are possible. If $c_{H_2}(p_{3_2}, p_{6_2}) > c_{T_{\infty_1}}$, type 2 cells do not become activated and become eventually extinct, and the type 1 cells settle onto the steady state prescribed by Eq. (4.6.12). If, by contrast, $c_{T_{\infty_1}} > c_{H_2}(p_{3_2}, p_{6_2}) > c_\infty$ is satisfied, type 2 cells out-compete type 1 cells and the system, composed entirely of type 2 cells, settles onto the steady state prescribed by Eq. (4.6.15). In this sense, quiescent cells have *stem-cell-like behaviour*, in the sense that they can repopulate the system. In this second scenario, therapy is not completely without virtue since therapy drives the system to be taken over by a slower-cycling (less aggressive) phenotype.

4.6.3 Simulation results

In order to check the accuracy of the mean-field analysis carried out in Section 4.6.2 regarding the critical survival fraction for rescue from quiescence. We start by showing (Fig. 4.12) two typical realisations of the stochastic population dynamics which illustrate the rescue mechanism. In this simulations, we first let the active population settle on to its steady state. We then apply a sustained therapy with constant survival fraction. A more aggressive treatment ($F_S = 0.6$ in Fig. 4.12) greatly affects the active population: the amount of active cells killed by the therapy induces re-oxygenation of the population above the critical oxygen level for activation of the quiescent population whereupon the quiescent cells become proliferating. In Figs. 4.12(a) & (c), we show that upon activation of the quiescent population, a competition between both populations ensues, which eventually leads to extinction of the active population. A less aggressive therapy ($F_S = 0.7$ in Fig. 4.12) also induces death of the active population and re-oxygenation. However, in this case, the latter is not intense enough to induce activation of the quiescent cells (see Fig. 4.12(d)) and therefore the active cells will repopulate the system as the quiescent population stays on its course to eventual extinction, as shown in Fig. 4.12(b).

Fig. 4.13 shows simulation results for the variation of probability of fixation of the quiescent population as the survival fraction of the therapy, F_S changes. Our simulation results show qualitative agreement with our mean-field theory (see Sections 4.6.1 & 4.6.2): as the survival fraction increases (i.e. the therapy becomes less efficient), the probability of fixation abruptly decreases from almost certainty of fixation to almost certainty of extinction. We observe that our mean-field theoretical predicts a critical value for F_S slightly smaller than the observed when fluctuations due to finite size effects are present. However, we observe that, as the carrying capacity of the system is increased, the critical value of F_S converges to the mean-field value.

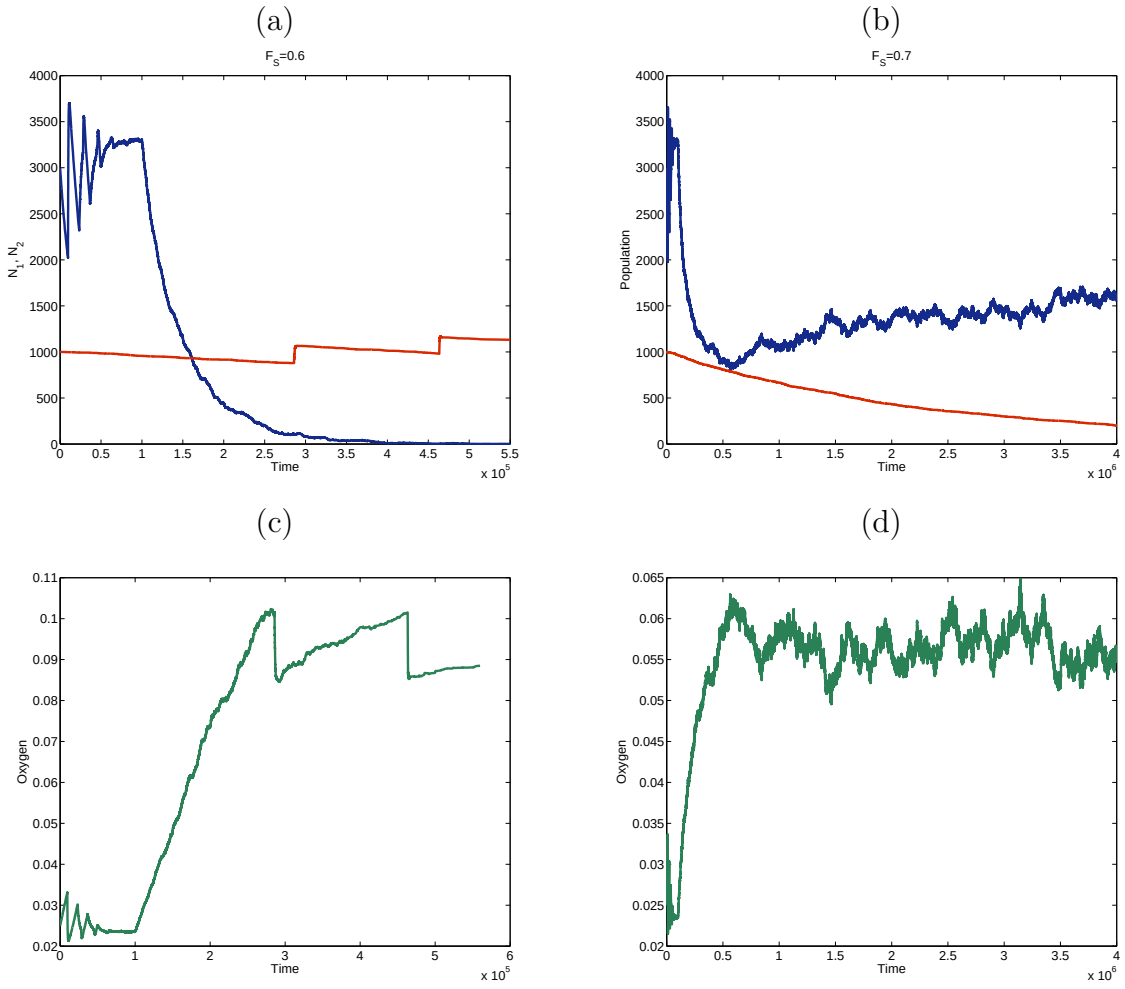

Figure 4.12: Stochastic simulation results showing typical realisations associated with rescue of quiescence cells (plots (a) & (c)) and recovery of the proliferating population (plots (b) & (d)) upon application of a cell-cycle dependent therapy. The efficiency of the therapy is characterised by the survival fraction, F_S. Quiescence rescue is achieved when the survival fraction is set to a value which falls below the critical threshold, Eq. (4.6.17). If $F_S < F_{S_C}$ (plots (a) & (c)), the cell killing triggered by the therapy is enough to re-oxygenate the population above the activation threshold of the quiescent cells. By contrast, if $F_S > F_{S_C}$ (plots (b) & (d)), re-oxygenation is not enough to rescue latent cells from quiescence. Parameter values: $\nu_1 = 4.167 \cdot 10^{-5}$, $\nu_1 = 4.167 \cdot 10^{-7}$, $\tau_{p_1} = \tau_{p_2} = 2.1 \cdot 10^{-3}$, $\frac{p6_1}{p3_1} = 1$, $\frac{p6_2}{p3_2} = 0.989$. The subindex "1" corresponds to the active population whilst the subindex "2" denotes quantities associated with the quiescent population. The critical oxygen (as defined in Sections 4.3.5 & 4.3.6) is $c_{cr_1} = 0.023$ for the active cells and $c_{cr_2} = 0.1$ for the quiescent cells. Colour code: blue (red) lines correspond to the time evolution of the total number of proliferating (quiescent) cells and green lines, to the time evolution of the oxygen concentration

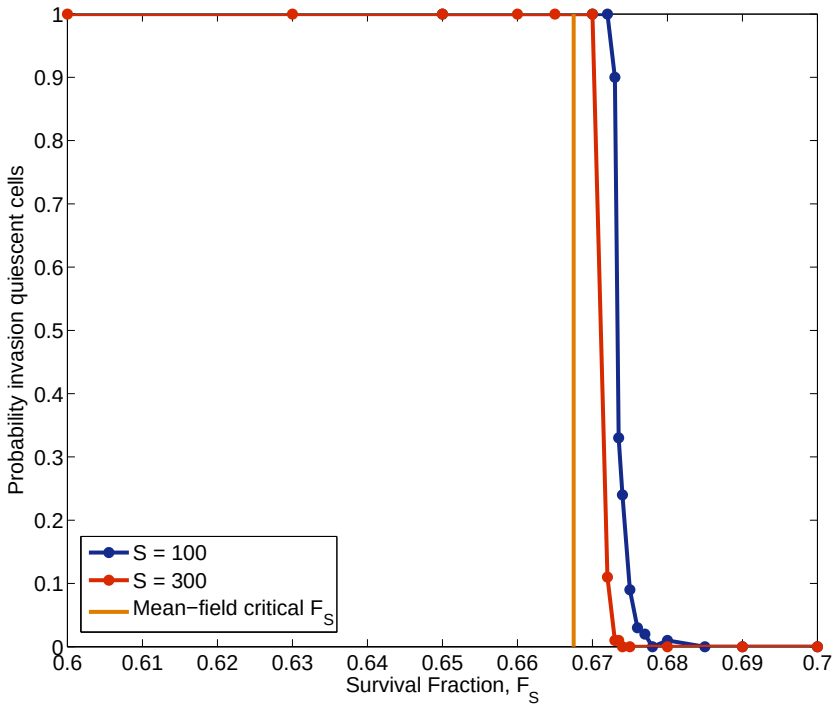

Figure 4.13: This figure shows stochastic simulation results regarding the variation of the probability of fixation of the quiescence population varies the efficiency of a cell-cycle dependent therapy changes. The efficiency of the therapy is measured in terms of the survival fraction F_S. The orange vertical line represents the mean-field, theoretical critical survival fraction (Eq. 4.6.17). We observe that as the carrying capacity of the system increases, which in these simulations is achieved by increasing the rate of oxygen supply, S, the results of the stochastic simulations tend towards the mean-field prediction. Parameter values: $\nu_1 = 4.167 \cdot 10^{-5}$, $\nu_1 = 4.167 \cdot 10^{-7}$, $\tau_{p_1} = \tau_{p_2} = 2.1 \cdot 10^{-3}$, $\frac{p_{6_1}}{p_{3_1}} = 1$, $\frac{p_{6_1}}{p_{3_1}} = 0.989$. The subindex "1" corresponds to the active population whilst the subindex "2" denotes quantities associated with the quiescent population. The critical oxygen (as defined in Sections 4.3.5 & 4.3.6) is $c_{cr_1} = 0.023$ for the active cells and $c_{cr_2} = 0.1$ for the quiescent cells. Each data point corresponds to the average over 500 realisations of the stochastic population dynamics.

Chapter 5

Coarse-graining and hybrid methods for efficient simulation of stochastic multi-scale models of tumour growth

5.1 Introduction

Cells behaviour within tissues respond to a number of stimuli. Their behaviour result from a complex network of interactions between genes and gene products which ultimately regulates gene expression. Such systems of gene regulation are often modelled as non-linear, high-dimensional dynamical systems whose structure has been molded in the course of biological evolution. In addition to such intracellular complex dynamics, cells are also influenced by intricate interactions between different components of the biological systems at all levels, from complex signalling pathways and gene regulatory networks to complex non-local effects where perturbations at whole-tissue level [6, 45, 115, 149, 168, 170, 180, 187]. These and other factors contribute towards a highly complex dynamics in biological tissues which is an emergent property of all the layers involved. To tackle such complexity, a number multi-scale models of biological systems, particularly in the context of tumour growth, have been developed [6, 34, 39, 42, 45, 52, 115, 116, 147, 149, 170, 168, 176, 180, 181, 186, 187, 197, 211, 218, 219, 232].

Many current multi-scale models of tumour growth formulated so far are individual-based, i.e. cells are individually resolved and their response to different types of cues (chemical, mechanical, etc.) is explicitly described by models of cell behaviour of varying levels of complexity [6, 42, 45, 115, 116, 168, 176, 180, 187, 211]. Further to the individual-based approach to multi-scale modelling of biological cell populations, we have recently introduced new stochastic models that allow to analyse the effects of fluctuations, both at the intracellular level (intrinsic noise in signalling pathways and

gene regulatory networks) and at the level of the birth-and-death dynamics of cells [89], chapter 4.

Multi-scale approaches have been shown to have both strengths and limitations. Among the latter, it prominently features the computational intensity of these models. The level of detail they involve implies that large scale simulations are computationally costly, which limits the scope of such models. In order to simulate growth in a wider range of conditions, along with model development, algorithms and analytic methods must be developed that enable us for more efficient analysis and simulation of such models. The formulation of hybrid methods for multi-scale models of the growth of tumour [127, 128, 129] is one such development. The basis of hybrid methodologies is to use models at different resolutions in different regions of the simulation domain, whereby cells (or other structures such as vessels in models of angiogenesis) are individually resolved in some region of interest. Away from such region, the system is described by a lower-resolution, coarse-grained model, obtained for example by means of homogenisation methods [38, 152, 172, 173, 174, 200]. Such homogenised model describes the system at a reduced level of detail but with the benefit of a much smaller computational cost. The challenges involved in these hybrid methodologies include defining criteria to identify the different domains, derive coarse-grained models consistent with their individual-based counterparts, and formulate the appropriate boundary conditions between the individual-based and coarse-grained regions.

A similar situation arises in a different area in which fair progress has been made: stochastic reaction-diffusion systems. Such systems are also costly to simulate using standard methods (i.e. variations of the Gillespie method [21, 57, 209]), so it is often necessary to resort to hybrid methods [156]. The rationale for a hybrid method is that noise levels, roughly associated with the local population or number of particles, is not uniform over the whole system, resulting in regions where fluctuations have more severe effects than in others. An archetypic example of this situation is the propagation of fronts such as travelling waves [28, 32, 41, 156]. In such systems, the population behind the propagating front approaches the carrying capacity of the system. If the carrying capacity is large enough, fluctuations in the region behind the front will be relatively small, so that the system may be described by the mean-field limit of the system. By contrast, at the front and ahead of it fluctuations dominate system behaviour and therefore the full stochastic description is needed. Such inhomogeneities in the level of noise have been exploited to formulate hybrid simulation methods. According to this methodology, the mean-field limit of the system is used in low-noise regions which are then coupled to the full stochastic dynamics describing the high-noise regions. The coupling between both descriptions is achieved by means of appropriately defined boundary conditions at the interface(s) between mean-field and stochastic regions [60, 62, 98, 156, 189, 206, 214, 235].

In this chapter, we extend and further develop the hybrid method formulated by

[206] for stochastic reaction-diffusion systems to stochastic multi-scale models of tumour growth. Such models [89], chapter 4 consider fluctuations regarding both number of cells (*population* noise) and the intracellular (cell-cycle) dynamics (*structure* noise), and consequently any attempt to formulate a hybrid method for such systems must find a way to accommodate both types of noise. Structure noise is associated with noise at the intracellular level and it manifests itself in fluctuations of the birth rate. We show in our analysis that this source of noise is at least as important as the population noise on the behaviour of the system. In particular, we show that the speed of propagation of travelling wave solutions is heavily affected by birth rate fluctuations at the leading edge of the front. More specifically, when a model in which the intracellular dynamics is coarse-grained (i.e. fluctuations of the birth rate are averaged out) is considered, the speed of the travelling wave front is over-estimated by a rather significant percentage. However, when the coarse-grained mean-field model is coupled to the full stochastic multi-scale population-dynamical model, the deviation travelling wave speed is very much rectified and a much more accurate result is obtained. This result demonstrates the usefulness of such hybrid approaches: they can recover accurately the behaviour predicted by the more detailed models whilst, by averaging out some of those details in regions where they are not necessary, their computational performance is much improved.

5.2 Summary of the stochastic multi-scale model

The model presented here is closely related to that presented in chapter 4, the main difference being the introduction of spatial heterogeneities. This model intends to describe the growth of cellular populations in a spatially heterogeneous environment under the restriction of finite amount of available resources (in this case, oxygen $c(t, x)$) supplied at a finite rate, $\bar{S}(t, x)$.

The general approach to the stochastic population dynamics used here is a natural generalisation of the standard continuous-time birth-and-death Markov process and its description via a Master Equation [68]. In chapter 4 showed that the consideration of the multi-scale structure of the system, i.e. the inclusion of the physiological structure associated with the cell-cycle variables, can be accounted by an age-structure within the population: the birth rate depends on the age of cell (i.e. time elapsed since last division) which determines, through the corresponding cell-cycle model, the cell-cycle status of the corresponding cells.

We summarise the different sub-models involved in the formulation of the stochastic multi-scale model. For a detailed discussion of a non-spatial version of the model we refer the reader to 4. Here, we emphasise the new elements introduced by considering spatially extended systems.

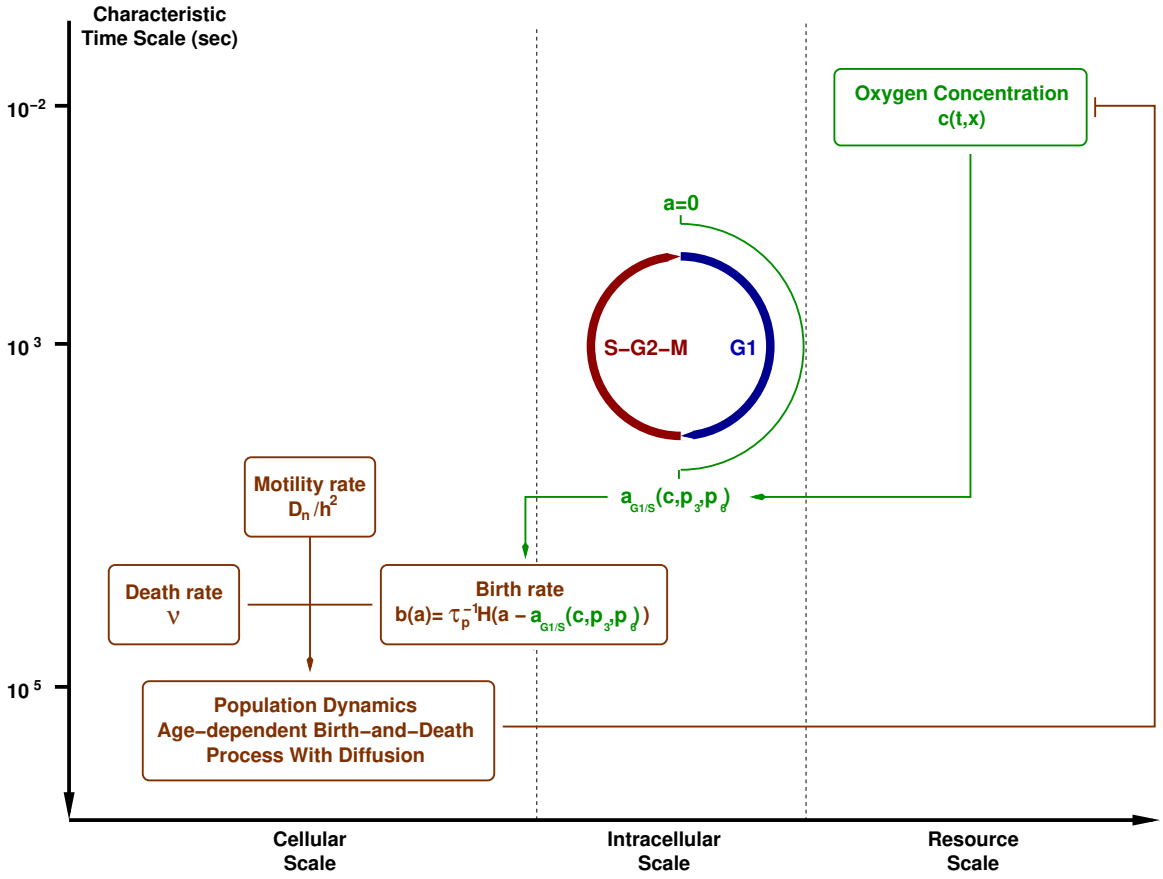

Figure 5.1: Schematic representation of the different elements that compose our multi-scale model. This scheme is an extension of Fig. 4.1, adding a spatial component to the model.

5.2.1 General setting

Our model couples partial differential equation (PDE), continuum models for diffusible substances, which drive individual cell behaviour, with a spatially discrete cell population dynamics described by a reaction-diffusion Master Equation (RDME) [21, 90, 113, 205, 209]. The scheme that we are using is a simple extension of the Chemical Master Equation (CME), where the space is discretised into a lattice. Each lattice site is associated to a compartment and the population within each compartment is assumed to be homogeneous (well-mixed) with reaction rates modelled according to the (local) law of mass action: reaction rates depend on the population within the corresponding compartment only. Diffusion is modelled by means of continuous-time random walk on the lattice.

Regarding the coupling between the diffusible substances (in this particular case, oxygen) and the birth-and-death dynamics, we assume that all the cells within a compartment are exposed to the same concentration and, therefore, they all respond identically to their stimuli. From the numerical point of view, we will assume that the grid on which we solve the PDEs is the same as the lattice which sustains the stochastic population dynamics. Since we primarily focus on one dimensional numerical experiments, PDEs are solved using a finite-difference discretation and an explicit Euler or a four-stage Runge-Kutta method.

We must note that the RDME approach has been recently criticised as it has been shown that, except in one dimension, it does not converge to a continuum reaction-diffusion PDE [112]. A convergent RDME scheme has been recently proposed [113], although at this point we limit ourselves to the classical RDME scheme.

5.2.2 Resource layer: dynamics of diffusible substances

The evolution of the concentration of oxygen, $c(t,x)$, (*resource scale* see Fig. 5.1) is modelled by:

$$\frac{\partial c}{\partial t} = D_c \frac{\partial^2 c}{\partial x^2} - kc \sum_{x_i \in \mathcal{L}} N(t,x_i)\delta(x-x_i) + \bar{S}(t,x) - k_2 c, \tag{5.2.1}$$

where $\mathcal{L}$ is the lattice defined in Section 5.2.1 (see Fig. 5.2), and $N(t,x_i)$, $i = 1,\ldots,N_{\mathcal{L}}$, is the number of cells in compartment i at time t. Note that, in general, $N(t,x_i)$ is a stochastic process, and, therefore, in principle Eq. (5.2.1) should be treated as a stochastic differential equation [104]. $\bar{S}(t,x)$ is a source that accounts for oxygen delivery to the system. D_c is the oxygen diffusion coefficient, k is the oxygen consumption rate, and k_2 is a oxygen decay rate.

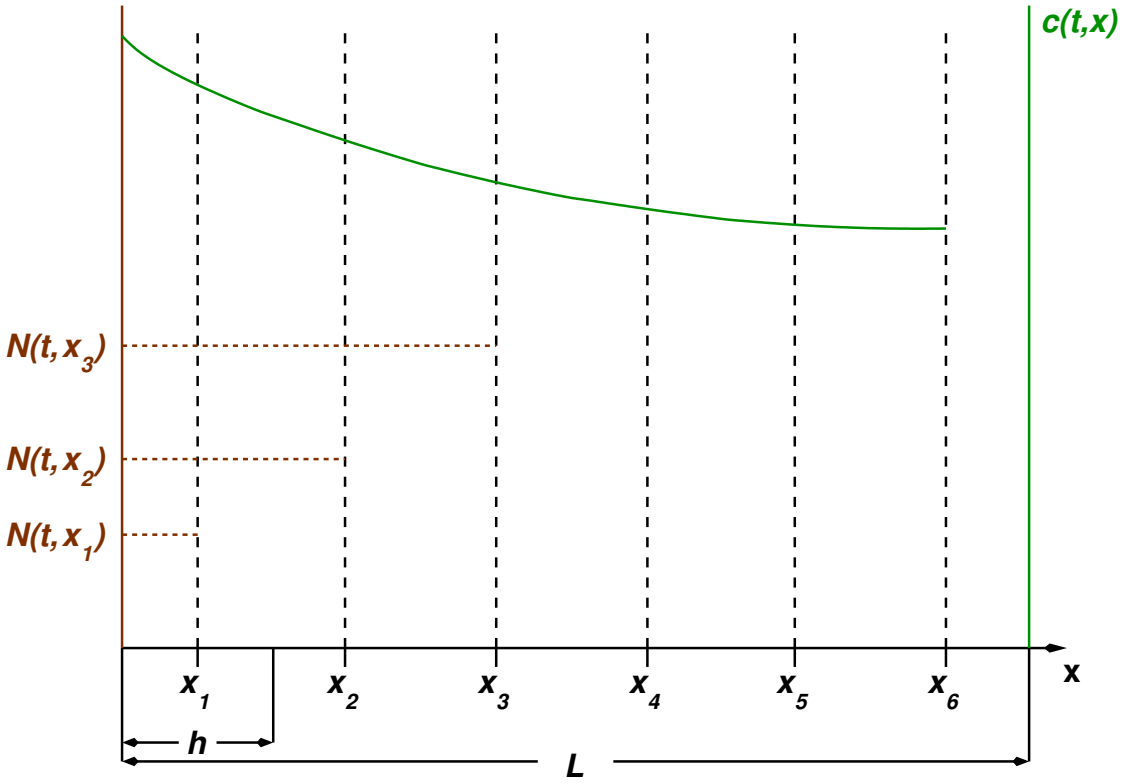

Figure 5.2: Representation of the setting of our model. Diffusible substances (e.g. oxygen), $c(t,x)$, is modelled as a continuous field described by a reaction-diffusion PDE, it is represented by green solid line. The birth-and-death dynamics with diffusion of the cell population is modelled by means of a RDME on a lattice $\mathcal{L}$. Each vertex of the lattice, $x_i \in \mathcal{L}$, is associated to a compartment of voxel within which the population is assumed to be well-mixed and its stochastic dynamics ruled by a *local* law of mass action. L is the total length of the system and h is the lattice spacing, so that $L = N_{\mathcal{L}} h$ where $N_{\mathcal{L}} = \text{card}(\mathcal{L})$. Here $N(t,x_i)$ depict the number of cells in compartment i and it is calculated as $N(t,x_i) = \int_0^\infty n(t,a,x_i)da$, with $n(t,a,x_i)$ being the number of cells of age a at time t and compartment x_i.

5.2.3 Intracellular layer: oxygen-dependent birth rate

The intracellular scale in the present model is the same as for the model in chapter 4 (see chapter 4, section 4.3).

5.2.4 Cellular scale: Age-structured birth-and-death with diffusion

Consider the random variable $n(t, a, x_j)$, i.e the number of cells of age a in position x_j at time t. Age is defined as the time elapsed since last division. Let us further define the random vector $\mathcal{N}(t, a) = (n(t, a, x_1), \ldots, n(t, a, x_{N_\mathcal{L}}))$ where $N_\mathcal{L} = \text{card}(\mathcal{L})$. An age-dependent Master Equation can be written for the birth-and-death with diffusion process described in Table 5.1, which is an extension of the age-dependent birth-and-death process formulated in chapter 4 to account for the effects of cell diffusion. Chapter 4 have shown that the evolution on each characteristic curve or *genealogy* (see Fig. 5.3) is independent and, therefore, the following equality holds on each characteristic curve:

$$P(\mathcal{N}, t + \delta t, a + \delta a) = \sum_{j=1}^{N_\mathcal{L}} \sum_{i=1}^{z+2} W_i(\mathcal{N} - \mathcal{R}_i, t, a, x_j)\delta t P(\mathcal{N} - \mathcal{R}_i, t, a) + \left(1 - \sum_{i=1}^{4} W_i(\mathcal{N}, t, a, x_j)\delta t\right) P(\mathcal{N}, t, a) \tag{5.2.2}$$

where $\delta a = \delta t$, z is the coordination number of the lattice $\mathcal{L}$, and $\mathcal{R}_i = (r_{i_1}, \ldots, r_{i_{N_\mathcal{L}}})$ with W_i and r_{i_j} are given in Table 5.1. Re-arranging terms and taking the limit $\delta t \to 0$, we obtain:

$$\frac{\partial P(\mathcal{N}, t, a)}{\partial t} + \frac{\partial P(\mathcal{N}, t, a)}{\partial a} = = \sum_{j=1}^{N_\mathcal{L}} \sum_{i=1}^{z+2} (W_i(\mathcal{N} - \mathcal{R}_i, t, a, x_j)P(\mathcal{N} - \mathcal{R}_i, t, a) - W_i(\mathcal{N}, t, a, x_j)P(\mathcal{N}, t, a)) \tag{5.2.3}$$

A cornerstone in our model is the age-dependent birth rate, $b(a)$, defined in Table 5.1, since it constitutes the coupling between the three layers that compose our multi-scale model: nutrient, intracellular, and cellular layer. In Section 5.2.3, we have discussed a model in which we consider that cell division is divided into parts: a regulated one culminating in the G1/S transition, characterised by the oxygen-dependent MFPT, $a_{G1/S}$, Eq. (4.3.57), and an unregulated one characterised by an average duration, τ_p^{-1}. This model can be described by an age-dependent birth rate:

$$b(a) = \tau_p^{-1}\mathcal{H}(a - a_{G1/s}(c, p_6/p_3)) \tag{5.2.4}$$

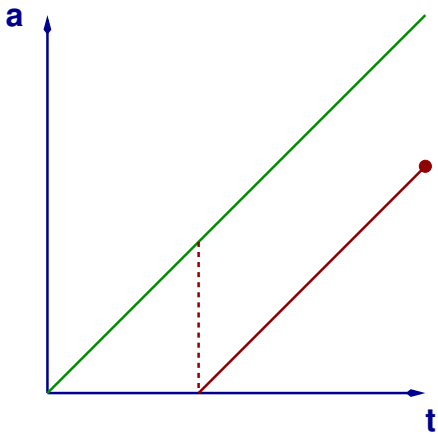

Figure 5.3: This plot shows a schematic representation of the characteristic curves, $a = t + a_0$, corresponding to our age-structured stochastic dynamics and the emergence of new genealogies (red line) when a birth occurs (indicated by the red dashed line) within a previously existing one. Genealogies terminate when the corresponding population becomes extinct (indicated by the red point).

where $\mathcal{H}(\cdot)$ is Heaviside's step function and $a_{G1/S}$ is given by Eq. (4.3.57). Eq. (5.2.4) can be interpreted as follows: cell division cannot occur in cells younger than the oxygen regulated age $a_{G1/S}$. Cells that have aged beyond $a_{G1/S}$ undergo cell division at a constant rate τ_p^{-1}.

5.2.5 Linking scales together

The connections between different time-scales describe in Fig. 5.1 is given by coupling the different sub-models so that the global behaviour of the system arises as an emergent property of this linking:

1. The coupling between the intracellular and the cellular layers takes place through the age-dependent birth rate, Eq. (5.2.4).

2. The intracellular layer and the resource layer are coupled through the oxygen-dependence MFPT to the G1/S transition, given by Eq. (4.3.57).

3. Finally, the resource layer is coupled to the cellular layer, via Eq. (5.2.1), where the cell population regulates the concentration of oxygen, where N is,

$$N(t, x_j) = \int_0^\infty n(t, a, x_j) da. \tag{5.2.5}$$

Event	Reaction	$W_k(n,t,a,x_j)$	r_k
Birth	$n(t,a,x_j) \to n(t,a,x_j) - 1$ $\varnothing \to n(t,a=0,x_j) = 2$	$W_1 = b(a)n(t,a,x_j)$	$r_{1_j} = -1$, $r_{1_k} = 0,\ k \neq j$
Death	$n(t,a,x_j) \to n(t,a,x_j) - 1$	$W_2 = \nu n(t,a,x_j)$	$r_{2_j} = -1$, $r_{1_k} = 0,\ k \neq j$
Diffusion	$n(t,a,x_j) \to n(t,a,x_j) - 1$ $n(t,a,x_{j\pm1}) \to n(t,a,x_{j\pm1}) + 1$	$W_{2+k} = \frac{D_n}{h^2} n(t,a,x_j)$ $k = 1,\dots,z$	$r_{2+k_j} = -1$, $r_{2+k_l} = 1,\ x_l \in \langle x_j \rangle$

Table 5.1: This table shows the details regarding the rates and stoichiometric matrix associated with the birth-and-death with diffusion process. This process is a straightforward generalisation of the age-dependent birth-death-process formulated in chapter 4. Here $b(a)$ is the age-dependent birth rate, ν is the death rate (which, for simplicity, we assume to be age-independent), and D_n is the diffusion coefficient of the cells. h is the lattice spacing defined in Fig. 5.2. Furthermore, $\langle x_j \rangle$ stands for the set of neighbours of x_j in $\mathcal{L}$, and z is the so-called coordination number, i.e. the number of neighbours of a node: $z = \mathrm{card}(\langle x_j \rangle)$.

5.3 Separation of time scales and coarse-graining of the age structure

In this section we analyse the system regarding the separation of time scales in the system. This analysis requires to make assumptions involving typical key parameter values, particularly the oxygen diffusion coefficient, D_c, the cell diffusion coefficient, D_n, and the average cell life expectancy, ν^{-1}. These assumptions are consistent with typical values of these parameters reported in the literature.

We start our analysis by considering the mean-field (deterministic) limit of our model, where the different time scales arise in a more intuitive way. We will then generalise our analysis to the full stochastic system using the Poisson representation [17, 121, 137], rather than the Master Equation representation Eq. (5.2.3). In both cases, we will show that provided that $\nu^{-1} \gg \tau_n \gg \tau_c$, where $\tau_c = h^2/D_c$ and $\tau_n = h^2/D_n$, is satisfied, it is possible to approximate the age-structured system by a coarse-grained version of it where the age distribution within the population reaches a quasi-steady state that can be explicitly calculated. This allows for a huge simplification of the model and the formulation of efficient hybrid numerical schemes.

5.3.1 Mean-field model

The mean-field limit of our stochastic model is a straightforward generalisation of the one obtained in chapter 4 for the non-spatial model:

$$\frac{\partial c}{\partial t} = D_c \frac{\partial^2 c}{\partial x^2} - kN(t,x)c + \bar{S}(t,x) - k_2 c, N(t,x) = \int_0^\infty n(t,a,x)da, \qquad (5.3.1)$$

$$\frac{\partial n}{\partial t} + \frac{\partial n}{\partial a} = D_n \frac{\partial^2 n}{\partial x^2} - (b(a) + \nu) n(t, a, x), \tag{5.3.2}$$

$$n(t, a = 0, x) = 2 \int_0^\infty b(a) n(t, a, x) da, \tag{5.3.3}$$

with no-flux boundary conditions at the boundaries of the domain and $b(a)$ is given by Eq. (4.3.57). We first proceed to express the system in dimensionless units: $\tau = \nu t$, $\alpha = \nu a$, $x \to x/h$, and $c \to c/c_0$, where c_0 is characteristic scale of the oxygen concentration. Eqs. (5.3.1)-(5.3.3) now read:

$$\epsilon_1 \frac{\partial c}{\partial \tau} = \frac{\partial^2 c}{\partial x^2} - \kappa N(\tau, x) c + \mathcal{S}(\tau, x) - \kappa_2 c, N(\tau, x) = \nu^{-1} \int_0^\infty n(\tau, \alpha, x) d\alpha, \tag{5.3.4}$$

$$\epsilon_1 \left(\frac{\partial n}{\partial \tau} + \frac{\partial n}{\partial \alpha} \right) = \epsilon_2 \frac{\partial^2 n}{\partial x^2} - (\tau_c b(\alpha) + \epsilon_1) n(\tau, \alpha, x), \tag{5.3.5}$$

$$n(\tau, \alpha = 0, x) = 2\nu^{-1} \int_0^\infty b(\alpha) n(\tau, \alpha, x) d\alpha, \tag{5.3.6}$$

with $\epsilon_1 = \tau_c \nu \ll 1$, $\epsilon_2 = \tau_c / \tau_n = D_n / D_c \ll 1$, $\kappa = \tau_c k$, and $\mathcal{S} = \tau_c \bar{S} / c_0$.

Under the assumption that $\epsilon_1 \ll 1$, $\epsilon_2 \ll 1$, and $\epsilon_2 \ll \epsilon_1$ hold, we now show that there are three different regimes: a regime that corresponds to the very early evolution, where the oxygen distribution evolves under a constant-in-time population until it reaches a quasi-equilibrium state, an intermediate regime where the only evolution is associated to the local evolution of the age-distribution (no cell diffusion) until the age-distribution reaches a quasi-steady state equilibrium, and a third regime, which corresponds to the long-time evolution of the system, where both cell diffusion and population birth-and-death occur, only that the latter corresponds to the quasi-steady state age-distribution.

Early evolution

Consider the following time and age re-scaling: $T = \epsilon_1^{-1} \tau$ and $A = \epsilon_1^{-1} \alpha$. Under this re-scaling the left hand sides of Eqs. (5.3.4) and (5.3.5) become $O(1)$. However, the two terms on the right hand side of Eq. (5.3.5) stay $O(\epsilon_2)$ and $O(\epsilon_1)$. Therefore, at the lowest order, i.e. $O(\epsilon_1^0)$, $n(T, A, x) \simeq cnt.$, i.e. $n(T, A, x) \simeq n(T = 0, A, x)$. Therefore,

$$\frac{\partial c}{\partial T} = \frac{\partial^2 c}{\partial x^2} - \kappa N(x) c + \mathcal{S}(T, x) - k_2 c, \; N(x) = \tau_c \int_0^\infty n(T = 0, A, x) dA, \tag{5.3.7}$$

that is the oxygen concentration evolves against a background of constant population, until it reaches a quasi-equilibrium oxygen distribution.

Intermediate regime

This regime does not involve any re-scaling. We only need to recall that $\epsilon_2 \ll \epsilon_1$ and $\epsilon_1 \ll 1$. Under this assumptions, one can neglect $O(\epsilon_2)$-cell diffusion in Eq. (5.3.5), with all the remaining terms of $O(\epsilon_1)$. Similarly, we can neglect the $O(\epsilon_1)$-left hand side of Eq. (5.3.4) compared to the $O(1)$ right hand side. The resulting approximation reads:

$$0 = \frac{\partial^2 c}{\partial x^2} - \kappa N(\tau, x)c + \mathcal{S}(\tau, x) - \kappa_2 c, N(\tau, x) = \nu^{-1} \int_0^\infty n(\tau, \alpha, x) d\alpha, \tag{5.3.8}$$

$$\frac{\partial n}{\partial \tau} + \frac{\partial n}{\partial \alpha} = -(\nu^{-1} b(\alpha) + 1) n(\tau, \alpha, x), \tag{5.3.9}$$

$$n(\tau, \alpha = 0, x) = 2\nu^{-1} \int_0^\infty b(\alpha) n(\tau, \alpha, x) d\alpha, \tag{5.3.10}$$

this means the population evolves in a purely local fashion, with no diffusion, where within each compartment the age-distribution evolves towards equilibrium with a quasi-steady state oxygen distribution. This local quasi-equilibrium age-distribution has been studied and described in chapter 4.

Long-time behaviour

Consider the re-scaling $\sigma = \frac{\epsilon_2}{\epsilon_1}\tau$ and $\gamma = \frac{\epsilon_2}{\epsilon_1}\alpha$. Under this re-scaling, the left had sides of both Eqs. (5.3.4) and (5.3.5) become $O(\epsilon_2)$. Since, the right hand side of Eq. (5.3.4) remains $O(1)$, the approximation is:

$$0 = \frac{\partial^2 c}{\partial x^2} - \kappa N(\sigma, x)c + \mathcal{S}(\sigma, x) - \kappa_2 c, N(\sigma, x) = \nu^{-1} \frac{\epsilon_1}{\epsilon_2} \int_0^\infty n(\sigma, \gamma, x) d\gamma, \tag{5.3.11}$$

$$\frac{\partial n}{\partial \sigma} + \frac{\partial n}{\partial \gamma} = \frac{\partial^2 n}{\partial x^2} - \frac{\epsilon_1}{\epsilon_2}(\nu^{-1} b(\gamma) + 1) n(\sigma, \gamma, x), \tag{5.3.12}$$

$$n(\sigma, \gamma = 0, x) = 2\nu^{-1} \frac{\epsilon_1}{\epsilon_2} \int_0^\infty b(\gamma) n(\sigma, \gamma, x) d\gamma, \tag{5.3.13}$$

Since $\epsilon_2 \ll \epsilon_1$, Eqs. (5.3.12) and (5.3.13) imply that the local birth-and-death process, which drives the evolution of the age-distribution of the population, is much faster than the spatial spread of the cells. In other words, the local age-distribution reaches a quasi-equilibrium state against the background of a quasi-steady state distribution of oxygen. This property suggests that the long term evolution of the system can be described by a coarse-grained (age-independent) system where the local birth-and-death dynamics is determined by the (oxygen-dependent) net growth rate, $\lambda_n(c)$. This quantity can be obtained from the local equilibrium age distribution in a straightforward way, as we have shown in chapter 4.

To make this statement more precise, consider a separable solution of Eqs. (5.3.12) and (5.3.13) in one dimension:

$$n(\sigma, \gamma, x) = \Sigma(\sigma)\Gamma(\gamma)X(x), \tag{5.3.14}$$

and assume the oxygen concentration to be a constant. This solution is characterised by two set of eigenvalues, $\lambda_D(k)$, which are associated to cell diffusion and which, for no-flow boundary conditions in one dimension, are given by $\lambda_D(k) = -k^2\frac{\pi^2}{L^2}$, $k = 0, 1, 2, \ldots$ with L being the length of the domain measured in units of h, i.e. the lattice spacing. The second set of eigenvalues, $\lambda_n(c)$, are associated to the local birth-and-death dynamics. If $b(a)$ is given by Eq. (5.2.4), $\lambda_{n_k}(c)$ are the solutions of the following characteristic equation [105]:

$$2\frac{\epsilon_1}{\epsilon_2}(\tau_p\nu)^{-1}\frac{e^{-\left(\lambda_{n_k}+\lambda_D(k)+\frac{\epsilon_1}{\epsilon_2}\right)\gamma_{G1/S}}}{\lambda_{n_k}+\lambda_D(k)+\frac{1}{\epsilon_2}(\epsilon_1+\tau_c\tau_p^{-1})} = 1. \tag{5.3.15}$$

where $\gamma_{G1/S}$ is a function of c. Now for each k we may solve for λ_{n_k} in terms of $\lambda_D(k)$, allowing for a full expansion of the solution in terms of Fourier modes. That is, we extract the Fourier coefficients a_k, b_k from the Fourier expansion of the initial condition and we construct the associated solution as

$$n(\sigma, \alpha, x) = \Sigma(0)\Gamma(0)\sum_{k=0}^{\infty} e^{\lambda_{n_k}\sigma}\exp\left(\lambda_D(k)\gamma - (\epsilon_{\mathbf{1}}/\epsilon_{\mathbf{2}} + \lambda_{n_k})\gamma - \frac{\epsilon_{\mathbf{1}}}{\nu\epsilon_{\mathbf{2}}}\int_0^{\gamma} b(\tau)\,d\tau\right)\cdot$$
$$\cdot\,(a_k\sin(k\pi x/L) + b_k\cos(k\pi x/L)) \tag{5.3.16}$$

Consider now the (unique) solution of Eq. (5.3.15) with $\lambda_D(k) = 0$, x_0. Then $\lambda_{n_k} = x_0 - k^2\frac{\pi^2}{L^2}$. Clearly the slowest mode would be the one for $k = 0$. From Eq. (5.3.15) and since $\epsilon_2 \ll \epsilon_1$, many modes have nearly the same time decay rate, being roughly the one dictated by λ_{n_0}. This accumulation of modes around the one associated to the equilibrium age-structure distribution justifies that the local age-distribution reaches a quasi-equilibrium state against the background of a quasi-steady state distribution of oxygen.

Coarse-grained mean-field description

In view of the above analysis, particularly the results of Sections 5.3.1 and 5.3.1, we formulate a coarse-grained limit of Eqs. (5.3.4)-(5.3.6), where the local age-distribution is assumed to be in quasi-equilibrium with the quasi-steady distribution of oxygen:

$$0 = \frac{\partial^2 c}{\partial x^2} - \kappa n_{cg}(\sigma, x)c + \mathcal{S}(\sigma, x) - \kappa_2 c, \tag{5.3.17}$$

$$\frac{\partial n_{cg}}{\partial \sigma} = \frac{\partial^2 n_{cg}}{\partial x^2} + \lambda_n(c)n_{cg}, \tag{5.3.18}$$

$$2\frac{\epsilon_1}{\epsilon_2}(\tau_p\nu)^{-1}\frac{e^{-\left(\lambda_n+\frac{\epsilon_1}{\epsilon_2}\right)\gamma_{G1/S}}}{\lambda_n+\frac{1}{\epsilon_2}(\epsilon_1+\tau_c\tau_p^{-1})}=1. \tag{5.3.19}$$

This description is valid from time $\sigma = O(1)$ onwards. It will fail to describe the earlier evolution of the system, where the local age-distribution of the population has not had time to reach equilibrium.

5.3.2 Stochastic system

We now proceed with multiple time scale analysis of the full stochastic system. As in the case of the mean-field analysis carried out in Section 5.3.1, our aim here is to try and find regimes where the stochastic system defined in Section 5.2.4 can be approximated by simpler versions that are more amenable to analysis and efficient numerical simulation. In particular, we will show that, under the same hypothesis as in Section 5.3.1 regarding time scales, it is possible to coarse-grain the system so that the local (i.e. within each compartment) age-distribution of the population can be assumed to have reached quasi-equilibrium.

We start by reformulating Eq. (5.2.3) in terms of the Poisson representation [17, 79, 121, 137]:

$$\begin{aligned} n(t,a,x_j) &= n(t=0,a-t,x_j) - Y\left(\int_0^t (b(a(t))+\nu)n(t,a(t),x_j)dt\right) + \\ &+ \sum_{x_l\in\langle x_j\rangle}\left(Y\left(\tau_n^{-1}\int_0^t n(t,a(t),x_l)dt\right) - Y\left(\tau_n^{-1}\int_0^t n(t,a(t),x_j)dt\right)\right), \end{aligned} \tag{5.3.20}$$

$$n(t,a=0,x_j) = 2Y\left(\int_0^\infty b(a)n(t,a,x_j)da\right) \tag{5.3.21}$$

where $a(t)$ is the equation of the characteristic curve (see Fig. 5.3) and $Y(\lambda) \sim$ Poisson(λ), i.e. $Y(\lambda)$ is a random number sampled from a Poisson distribution with parameter λ. By writing the system in terms of the dimensionless variables $\tau = \nu t$ and $\alpha = \nu a$:

$$\begin{aligned} \epsilon_1\frac{\partial c}{\partial \tau} &= \frac{\partial^2 c}{\partial x^2} - \kappa c\sum_{x_l\in\mathcal{L}} N(\tau,x_l)\delta(x-x_l) + \mathcal{S}(\tau,x) - \kappa_2 c, \\ N(\tau,x_j) &= \nu^{-1}\int_0^\infty n(\tau,\alpha,x_j)d\alpha, \end{aligned} \tag{5.3.22}$$

$$n(\tau,\alpha,x_j) = n(\tau=0,\alpha-\tau,x_j) - Y\left(\epsilon_1^{-1}\int_0^\tau (\tau_c b(\alpha(t))+\epsilon_1)n(t,\alpha(t),x_j)dt\right)$$

$$+\sum_{x_l\in\langle x_j\rangle}\left(Y\left(\epsilon_1^{-1}\epsilon_2\int_0^{\tau}n(t,\alpha(t),x_l)dt\right)-Y\left(\epsilon_1^{-1}\epsilon_2\int_0^{\tau}n(t,\alpha(t),x_j)dt\right)\right), \quad (5.3.23)$$

$$n(\tau,\alpha=0,x_j)=2Y\left(\epsilon_1^{-1}\int_0^{\infty}\tau_c b(\alpha)n(\tau,\alpha,x_j)d\alpha\right)$$

Under the same assumptions regarding time scales, i.e. $\epsilon_1 \ll 1$, $\epsilon_2 \ll 1$, and $\epsilon_2 \ll \epsilon_1$, we now show that the stochastic system exhibits exactly the same three regimes as its mean-field counterpart, namely, early evolution, where the oxygen distribution evolves under a constant-in-time population until it reaches a quasi-equilibrium state, an intermediate stage where the local age-distribution evolves (with no cell diffusion) until it reaches a quasi-steady state equilibrium, and a third regime, associated with the long-time behaviour, where both cell diffusion and population birth-and-death occur with the latter determined the quasi-steady state age-distribution.

Early evolution

Consider the re-scaling: $T=\epsilon_1^{-1}\tau$ and $A=\epsilon_1^{-1}\alpha$. Under this change of variables, both the right and left hand sides of Eq. (5.3.22) are now $O(1)$. The stochastic evolution of the population become:

$$n(T,A,x_j)=n(T=0,A-T,x_j)-Y\left(\epsilon_1\int_0^{T}(\nu^{-1}b(A(t))+1)n(T,A(t),x_j)dt\right)$$
$$+\sum_{x_l\in\langle x_j\rangle}\left(Y\left(\epsilon_2\int_0^{T}n(t,A(t),x_l)dt\right)-Y\left(\epsilon_2\int_0^{T}n(t,A(t),x_j)dt\right)\right), \quad (5.3.24)$$
$$n(T,A=0,x_j)=2Y\left(\epsilon_1^{-1}\int_0^{\infty}\nu^{-1}b(A)n(T,A,x_j)dA\right)$$

Taking into account that, upon re-scaling the waiting times associated to both diffusion and birth and death are very large, one can assume that $n(T,A,x_j)=n(T=0,A-T,x_j)+O(\epsilon_1)$. So that at the lowest order, i.e. $O(\epsilon_1^0)$, $n(T,A,x_j)$ remains constant, $n(T,A,x_j)\simeq n(T=0,A-T,x_j)$ [17, 121], so that:

$$\begin{aligned}\frac{\partial c}{\partial T}&=\frac{\partial^2 c}{\partial x^2}-\kappa c\sum_{x_l\in\mathcal{L}}N(x)\delta(x-x_l)+\mathcal{S}(T,x)-\kappa_2 c,\\ N(x)&=\nu^{-1}\epsilon_1\int_0^{\infty}n(T=0,A-\mathbf{T},x)dA\end{aligned} \quad (5.3.25)$$

Intermediate regime

Since $\epsilon_2 \ll 1$, to the lowest order, Eqs. (5.3.22) and (5.3.23) can be approximated by [17, 121]:

$$
\begin{aligned}
0 &= \frac{\partial^2 c}{\partial x^2} - \kappa c \sum_{x_l \in \langle x_j \rangle} N(\tau, x) \delta(x - x_l) + \mathcal{S}(\tau, x) - \kappa_2 c, \\
N(\tau, x_j) &= \nu^{-1} \int_0^\infty n(\tau, \alpha, x_j) d\alpha,
\end{aligned}
\tag{5.3.26}
$$

$$
\begin{aligned}
n(\tau, \alpha, x_j) &= n(\tau = 0, \alpha - \tau, x_j) - Y \left(\int_0^\tau (\nu^{-1} b(\alpha(t)) + 1) n(t, \alpha(t), x_j) dt \right) \\
n(\tau, \alpha = 0, x_j) &= 2Y \left(\nu^{-1} \int_0^\infty b(\alpha) n(\tau, \alpha, x_j) d\alpha \right)
\end{aligned}
\tag{5.3.27}
$$

Eqs. (5.3.26) and (5.3.27) imply that, during this intermediate dynamics, cell do not diffuse and the population dynamics is purely local against the background of a quasi-steady state distribution of oxygen. This evolution during this stage of the dynamics drives the local age-distribution towards local equilibrium.

Long-time behaviour

We finish our analysis by, once again, considering the following re-scaling of the time and age variables: $\sigma = \frac{\epsilon_2}{\epsilon_1}\tau$ and $\gamma = \frac{\epsilon_2}{\epsilon_1}\alpha$. Under this change of variables and recalling that $\frac{\epsilon_1}{\epsilon_2} \gg 1$, Eqs. (5.3.22) and (5.3.23) transform into:

$$
\begin{aligned}
0 &= \frac{\partial^2 c}{\partial x^2} - \kappa c \sum_{x_l \in \langle x_j \rangle} N(\sigma, x_j) \delta(x - x_l) + \mathcal{S}(\sigma, x) - \kappa_2 c, \\
N(\sigma, x_j) &= \nu^{-1} \frac{\epsilon_1}{\epsilon_2} \int_0^\infty n(\sigma, \gamma, x_j) d\gamma
\end{aligned}
\tag{5.3.28}
$$

$$
\begin{aligned}
n(\sigma, \gamma, x_j) &= n(\sigma = 0, \gamma - \sigma, x_j) - Y \left(\frac{\epsilon_1}{\epsilon_2} \int_0^\sigma (\nu^{-1} b(\gamma(t)) + 1) n(t, \gamma(t), x_j) dt \right) + \\
&+ \sum_{x_l \in \langle x_j \rangle} \left(Y \left(\int_0^\sigma n(t, \gamma(t), x_l) dt \right) - Y \left(\int_0^\sigma n(t, \gamma(t), x_j) dt \right) \right), \\
n(\sigma, \gamma = 0, x_j) &= 2Y \left(\frac{\epsilon_1}{\epsilon_2} \int_0^\infty \nu^{-1} b(\gamma) n(\sigma, \gamma, x_j) d\gamma \right)
\end{aligned}
\tag{5.3.29}
$$

where we have neglected terms of $O(\epsilon_2)$.

Eqs. (5.3.28) and (5.3.29) are the basis for the formulation of our coarse-grained model. Eq. (5.3.29) imply that the rate at which the events associated with the local

birth-and-death dynamics fire up at a rate which is of order $O(\frac{\epsilon_1}{\epsilon_2}) \gg 1$, whereas diffusion occurs at a rate of order $O(1)$. This property implies that, between diffusion events and as long as such separation of time scales is large enough, the local age-distribution evolves through the birth-and-death dynamics, unperturbed by the diffusion part of the process, until it settles down on to quasi-equilibrium [36, 37].

Stochastic coarse-grained model

On the basis of the argument we have put forward in Section 5.3.2, we propose a coarse-grained model of the stochastic evolution Eqs. (5.3.22)-(5.3.23). This coarse-graining strategy consists of integrating out the age structure taking and formulating the stochastic birth-and-death dynamics in terms of the total local population only. This is done by using the fact that age-distribution is in quasi-equilibrium, and therefore is no longer valid in the early evolution of the system. In order to proceed with this programme, we first consider the number of new cells at time σ and position x_j, $n(\sigma, \gamma = 0, x_j)$. According to Eqs. (5.2.4) and (5.3.29), we can write:

$$n(\sigma, \gamma = 0, x_j) = 2Y \left(\frac{\epsilon_1}{\epsilon_2} (\nu \tau_p)^{-1} \int_{\gamma_{G1/S}}^{\infty} n(\sigma, \gamma, x_j) d\gamma \right) = 2Y \left(\frac{\epsilon_1}{\epsilon_2} B N(\sigma, x_j) \right), \tag{5.3.30}$$

where the coarse-grained birth rate is given by:

$$B = (\nu \tau_p)^{-1} \frac{\int_{\gamma_{G1/S}}^{\infty} n(\sigma, \gamma, x_j) d\gamma}{\int_0^{\infty} n(\sigma, \gamma, x_j) d\gamma}. \tag{5.3.31}$$

In a general setting, the quantity B should be considered as a function of time. However, under the conditions discussed in Section 5.3.2, where the age-distribution is in quasi-equilibrium, B is time independent. This is a simple consequence of the fact that at equilibrium, the ratio between the population younger than $\gamma_{G1/S}$ and the population older than $\gamma_{G1/S}$ is, on average, time independent [105].

Using the quasi-equilibrium condition, the (constant) fraction of the population younger than $\gamma_{G1/S}$ and the population older than $\gamma_{G1/S}$ can be estimated with regard to the probability of survival to age γ, $P_S(\gamma)$, which is given by:

$$P_S(\gamma, \lambda_n) \propto e^{-\lambda_n \gamma - \frac{\epsilon_1}{\epsilon_2} \left(\gamma + (\tau_p \nu)^{-1} (\gamma - \gamma_{G1/S}) \mathcal{H}(\gamma - \gamma_{G1/S}) \right)} \tag{5.3.32}$$

where λ_n is the mean-field growth rate, given by the characteristic equation (Eq. (5.3.15)), and $\mathcal{H}(\gamma)$ is Heaviside's step function [105]. At equilibrium, $P_S(\gamma, x_j)$ provides the proportion of the total population at compartment x_j of age γ. Therefore the ratio in Eq. (5.3.31) can be calculated from Eq. (5.3.32), so that:

$$B = (\nu\tau_p)^{-1}\frac{\left(\lambda_n + \frac{\epsilon_1}{\epsilon_2}\right)e^{-\frac{\epsilon_1}{\epsilon_2}\gamma_{G1/S}}}{\lambda_n + \frac{\epsilon_1}{\epsilon_2} + (\tau_p\nu)^{-1}\frac{\epsilon_1}{\epsilon_2}\left(1 - e^{-\frac{\epsilon_1}{\epsilon_2}\gamma_{G1/S}}\right)}. \tag{5.3.33}$$

Eq. (5.3.33) allows us to write a coarse-grained stochastic evolution which is given by:

$$\begin{aligned} 0 &= \frac{\partial^2 c}{\partial x^2} - \kappa c \sum_{x_l \in \langle x_j \rangle} N(\sigma, x_j)\delta(x - x_l) + \mathcal{S}(\sigma, x) - \kappa_2 c, \\ N(\sigma, x_j) &= \nu^{-1}\frac{\epsilon_1}{\epsilon_2}\int_0^\infty n(\sigma, \gamma, x_j)d\gamma, \end{aligned} \tag{5.3.34}$$

$$\begin{aligned} N_{cg}(\sigma, x_j) = N_{cg}(\sigma = 0, x_j) + Y\left(\frac{\epsilon_1}{\epsilon_2}B\int_0^\sigma N_{cg}(t, x_j)dt\right) - Y\left(\frac{\epsilon_1}{\epsilon_2}\int_0^\sigma N_{cg}(t, x_j)dt\right) + \\ + \sum_{x_l \in \langle x_j \rangle}\left(Y\left(\int_0^\sigma N_{cg}(t, x_l)dt\right) - Y\left(\int_0^\sigma N_{cg}(t, x_j)dt\right)\right), \end{aligned} \tag{5.3.35}$$

with B given by Eq. (5.3.33) taking into account that $\gamma_{G1/S} = \gamma_{G1/S}(c)$, i.e. it is a function of c given by Eq. (4.3.57).

5.4 Hybrid method for stochastic multi-scale models of tumour growth

We now proceed to describe the hybrid algorithm for stochastic multi-scale models For simplicity, we focus our discussion to the case of a single interface in one dimension. The formulation of our hybrid methodology follows closely that of [206]. We consider an interface between the mean-field and stochastic domains based on the number of total number cells: the interface, I, is located in the last compartment such that its total population is larger than a threshold, Θ:

$$N(t, x_I) = \int_0^\infty n(t, a, x_I)da > \Theta. \tag{5.4.1}$$

Since the description of the dynamics at the interface compartment is mixed, i.e. partly stochastic and partly mean-field, we impose that Θ be large enough compared to system size, so that both descriptions accurately account for the dynamics of the system. In order to increase the computational efficiency of our hybrid algorithm, we use the coarse-grained mean-field description coupled to the full age-structured stochastic model. We therefore need to provide specific rules for how age is introduced when cells are moved from the mean-field portion of the domain to the stochastic one.

Hybrid algorithm

We first provide a general overview of the algorithm. The parts that need more detailed discussion are dealt with later on.

1. Set Θ.

2. Set initial condition. We chose as an initial condition:

$$N(t, x_i) = KH(x_I - x_i),\ c(t, x_i) = c_\infty = cnt.$$

   where K is the carrying capacity and c_∞ is the associated equilibrium oxygen concentration. The age-distribution of the interface compartment, whose population dynamics is described by means of the stochastic model, is set to the equilibrium distribution Eq. (5.3.32). This choice is motivated by the fact that at the interface compartment both descriptions, i.e. the coarse-grained mean-field and the age-dependent stochastic process must hold.

3. Set time step as the waiting time to next stochastic event using the age-dependent Gillespie method (chapter 4).

4. Update the population within the stochastic domain according to the age-dependent Gillespie method (chapter 4).

5. Solve the PDEs for the coarse-grained mean-field population (over the mean-field domain) and the oxygen concentration (over the whole domain) in the interval $[t, t + \tau)$. The PDE for the oxygen is solved in the whole domain, mean-field plus stochastic parts, coupled to the coarse-grained population PDE and the stochastic population model, respectively.

6. Renormalise the number of cells in the interface compartment so that it is an integer.

7. Recalculate the position of the interface compartment.

8. Iterate 3-7 until some stopping condition is satisfied.

5.4.1 Coupling the mean-field and the stochastic models at the interface: fluxes, reactions and age-structure at the interface

This section provides details of how the mean-field and stochastic domains are coupled. Our procedure follows closely that presented in [206]. We currently provide the specific changes introduced to deal with age structure within the interface and beyond.

Recall that the interface compartment is considered as belonging to both the mean-field and the stochastic domains, so that the density of cells (associated with the mean-field description) is given by $n_{cg}(t, x_I) = \frac{N(t,x_I)}{h}$. Within the interface compartment, the population has age-structure and the birth-and-death dynamics is determined by the stochastic dynamics. The diffusive fluxes affecting it are considered exactly as in [206]: diffusion between the interface compartment and its stochastic neighbour are modelled using the usual diffusion transition rates:

$$\begin{aligned} W_{n_{x_I}-1,n_{x_I+1}+1|n_{x_I},n_{x_I+1}} &= \frac{D}{h^2} n(a,t,x_I), \\ W_{n_{x_I}+1,n_{x_I+1}-1|n_{x_I},n_{x_I+1}} &= \frac{D}{h^2} n(a,t,x_I+1), \end{aligned} \tag{5.4.2}$$

where, for simplicity, we have used the notation $n_{x_I} = n(a, t, x_I)$. The diffusive fluxes to and from the last mean-field compartment need to be slightly modified with respect to the ones proposed in [206] in order to accommodate the age-structure of the interface population. The flux, $J_{I,I-1}$, from the interface compartment, x_I, into the last mean-field compartment, x_{I-1}, simply involves integrating out the age and using $n_{cg}(t, x_I) = \frac{N(t,x_I)}{h}$:

$$J_{I,I-1} = \frac{D_s}{h^2} \left(n_{cg}(t, x_I) - n_{cg}(t, x_{I-1}) \right) \tag{5.4.3}$$

The flux from compartments x_{I-1} into x_I modelled deterministically with $n_{cg}(t, x_I)$:

$$n_{cg}(t + \tau, x_I) = n_{cg}(t, x_I) + \tau \frac{D_s}{h^2} \left(n_{cg}(t, x_I) - n_{cg}(t, x_{I-1}) \right). \tag{5.4.4}$$

We now need address two issues: cells entering the interface compartment must be assigned an age and the number of cells must be an integer. In order to deal with these, we first renormalise the number of cells using the same procedure as in [206]. This procedure involves the consideration of the fractional part of the population probabilistically: we consider it as one minus the probability of regularising the interface population by removing its fractional part. In this case the excess of mass is moved to and distributed over the mean-field domain. Otherwise, the necessary amount of mass is evenly taken from the mean-field part and a whole cell is added to the interface. Upon renormalisation, we need to assign an age to the the cell being removed or added to the interface. In the case of removal, this age is sampled from the age-structure distribution at the interface and one cell is removed from that age group. In the case of addition, the age of the added cell is sampled from the age-structure equilibrium distribution given by (5.3.32) and one cell is added to that age group.

5.4.2 Moving the interface

After completing the previous set of operations we must assess if the current interface position, held fixed through steps *3-6* of the hybrid algorithm, is consistent with

the updated state of the system. If this is not the case then we shall relocate the interface according to the updated state of the system before we resume with step *3*. Let us specify how to do this. First we check if the interface condition (5.4.1) continues to be satisfied at the interface compartment. If this is not the case (population at the current interface location dropped below Θ), we displace the interface one compartment to the left and check if the interface condition is met with this new choice of interface. If this happens to be true we stick with this new choice. If not we repeat this procedure until a compartment satisfying the interface condition is met, and then we displace the interface there. Incidentally we may find that we reach the left end of our spatial domain without fulfilling the previous criterion. In that case the whole spatial domain shall be described using the stochastic model on the next time step. However, this did not happen in any of our simulations -note that we are describing an invasion process.

Assume now that the interface condition (5.4.1) continues to be satisfied at the current interface compartment. What we do in this case is to check if the next compartment to the right does also satisfy this condition. In such a case we must shift the interface location one slot to the right and repeat this check (thus enlarging the mean field domain), until we make sure that we have relocated the interface so that its rightmost neighbour does not satisfy the interface condition.

The previous set of rules tells us how to position the interface after the state of the system is updated. If the interface experiences a net displacement then the mean field and stochastic regions are redefined. To be consistent with that we have to switch carefully between both descriptions at those voxels that changed from one domain to the other. If the interface moves to the right then we assign values to $N(t,x)$ at those locations in which it was not previously defined simply by integrating out the age variable. The procedure is subtler if the interface moves left, as we have to provide an age structure to those compartments entering the stochastic region from scratch. In the simple case of the interface moving a single voxel to the left, we proceed as follows: (i) we convert population identity to cell number at new interface's site -this will probably yield a non-integer cell number, (ii) we round the previous cell number into an integer value using the same mass transfer rules given in the previous paragraph, (iii) we assign an age structure to the resulting population by sampling the equilibrium age distribution (5.3.32) as many times as cells sit in the new interface compartment. Larger displacements are handled recursively by iterating unit displacements as we have just explained.

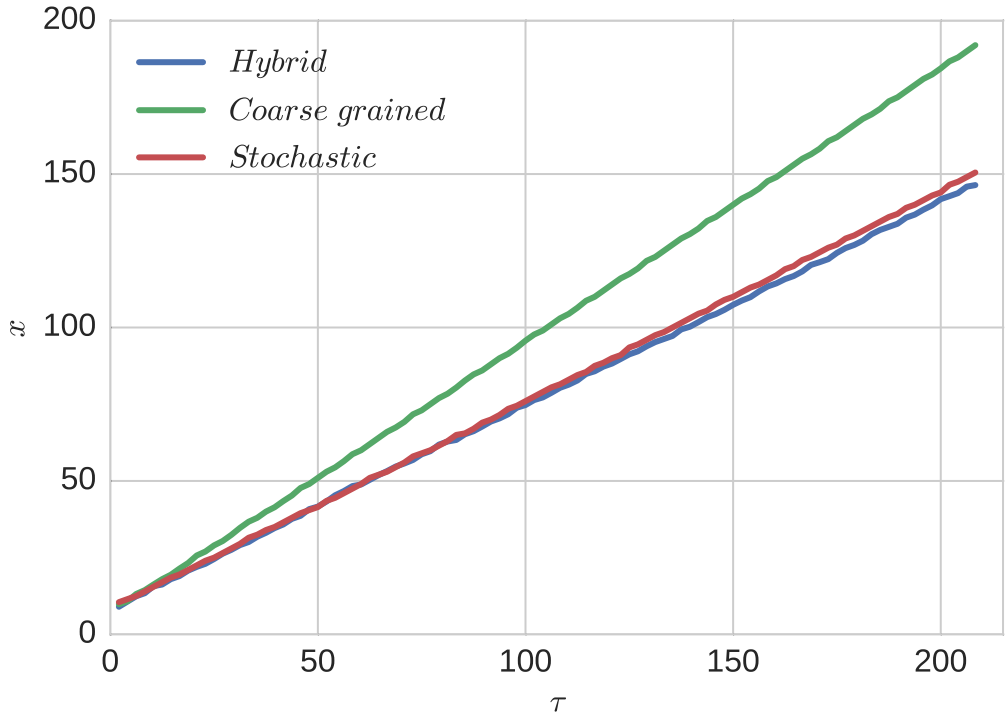

Figure 5.4: Plot showing the time evolution of the average front position for the three models: the coarse-grained mean-field model (green line), hybrid model (blue line), and stochastic model (red line). Results shown for the hybrid and stochastic models correspond to an average over 100 and 40 realisations respectively. $\Theta = 2000$. For other parameter values see Section 5.5. Position calculation: average of the positions x where the population is greater than 0 y smaller than K- 100

5.5 Assessing the accuracy of the coarse-grained and hybrid descriptions: travelling wave solutions

We now proceed to assess the accuracy of the coarse-grained mean-field and hybrid approximations by comparing them to the full stochastic simulations, which we take as our benchmark. We focus our analysis on the case where the system exhibit travelling wave behaviour. This regime has been used as a prototype to test a number of hybrid approaches in reaction-diffusion systems [206, 214]. Furthermore, travelling waves are a setting of particular interest regarding tumour modelling, as it has been used to describe of growth and invasion in several cancer models [69, 210]. In order to carry out a quantitative comparison between the predictions of the three models, we consider two quantities: the average position of the front of the travelling wave as a function of time, $X(\tau)$, and the average speed of the travelling wave.

We start our discussion by comparing the (average) position of the wave front as a function of time. Fig. 5.4 shows that, for all three models, the system exhibits travelling wave behaviour as the position of the wave front is a linear function of time, i.e. their speeds are constants. However, we appreciate that, whereas agreement between the results of the stochastic and hybrid models is rather good, an important departure exists between the results of the coarse-grained mean-field model and the stochastic and hybrid models.

This discrepancy is analysed in more a quantitative way in the results shown in Fig. 5.5, where we compare the travelling wave velocity measured in the coarse-grained mean-field simulation, v_{cg}, the stochastic model simulations, v, and the hybrid method simulations, v_h. We observe that whereas relative difference between v and v_h is typically of the order of a 5%, the relative difference between v_h and v_{cg} is of the order of a 30%. Before addressing this difference, we have checked the robustness of the wave speed v_h with respect to variations in Θ. Our results, see Figure 5.6, show that, as long as Θ is of the order of magnitude of the carrying capacity, K, v_h is rather insensitive to changes in Θ.

The rather substantial difference observed in the wave speeds and how the hybrid model rectifies this variation need to be explained, since fluctuations in the $N(t, x_j)$ do not seem to play a sufficiently significant role .In order to address these issues, we need to look beyond purely *demographic* noise, i.e. fluctuations of $N(t, x_j)$, and look into fluctuations associated with the age distribution of the population, or, in other words, fluctuations associated with the intracellular, cell-division dynamics. Recall that our coarse-grained approach is predicated upon the hypothesis that the age distribution of the system be in equilibrium (See Sections 5.3.1 and 5.3.2), given by Eq. (5.3.32). Under this hypothesis the growth rate of the population is given by Eq. (5.3.19), and the

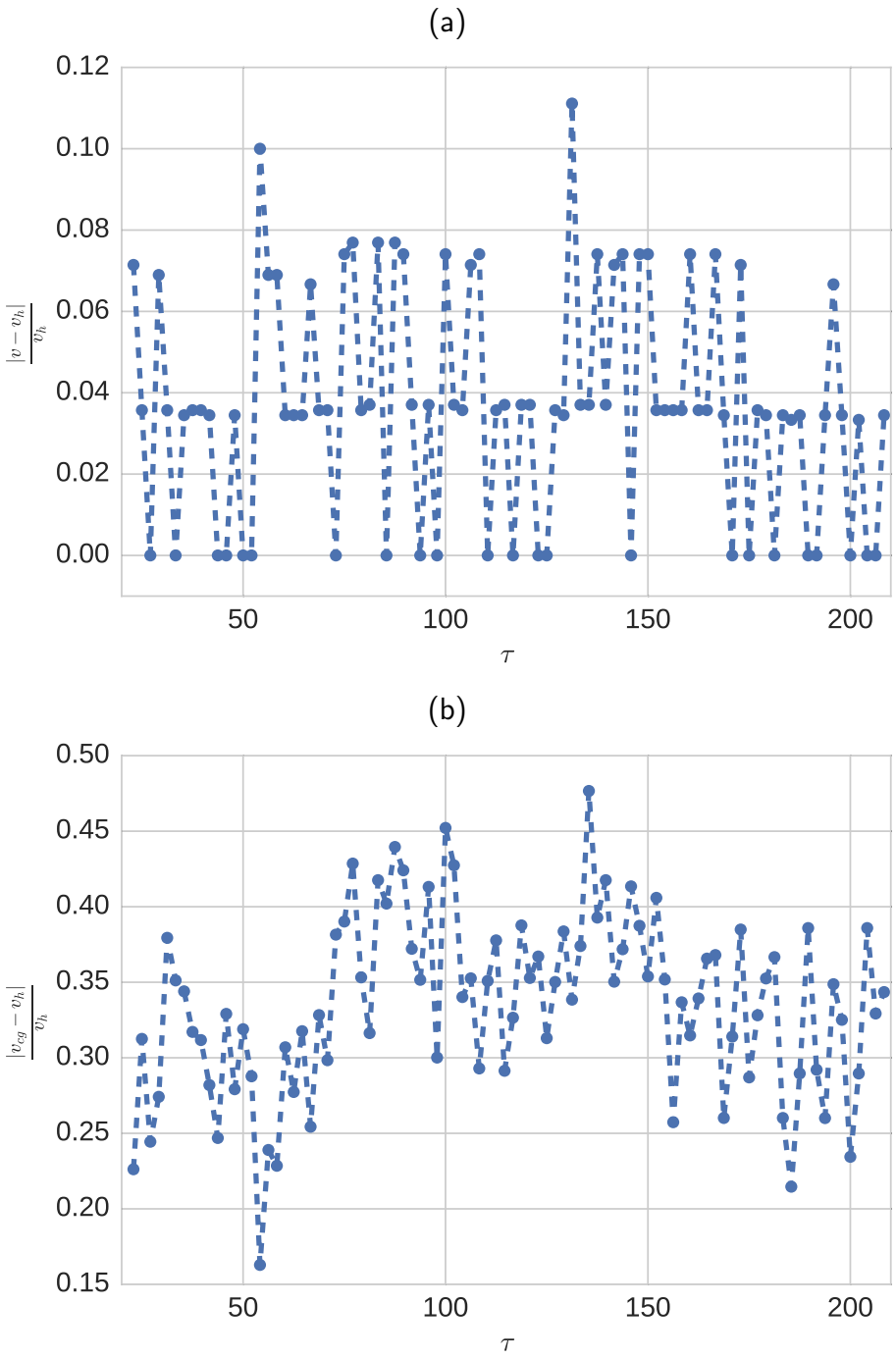

Figure 5.5: Results shown for the hybrid and stochastic models correspond to an average over 100 and 40 realisations respectively. $\Theta = 2000$. For other parameter values see Section 5.5. Velocity calculation: from Fig 5.4 data, subtracting two positions and diving by the elapsed time between both.

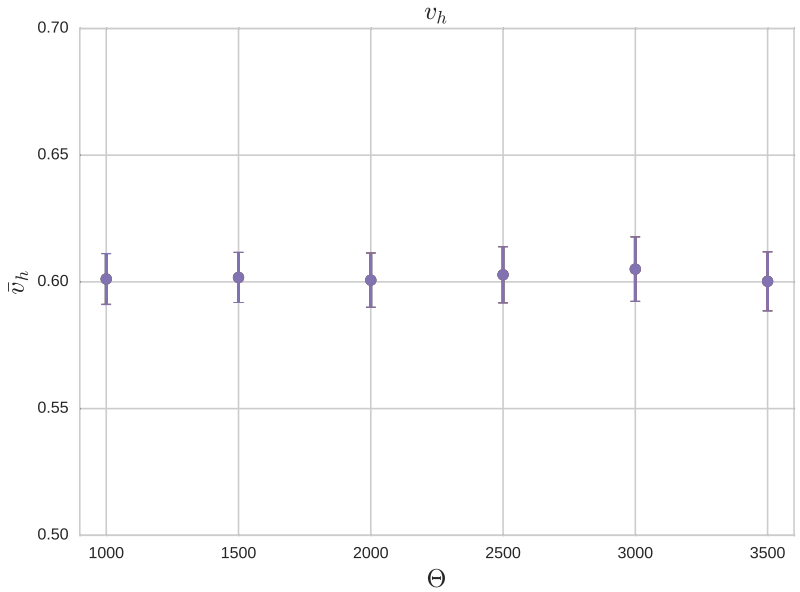

Figure 5.6: Comparison of the velocity average of 100 realisations of hybrid simulation with different threshold $\Theta = 1000$, 1500, 2000, 2500, 3000 and 3500. Error bars correspond to standard error of the mean.

birth rate, whose general expression is Eq. (5.3.31), is given by Eq. (5.3.33). Departure of the empirically measured birth rate (i.e. using Eq. (5.3.31)) from its equilibrium value is a signature of non-equilibrium fluctuations of the age structure and, therefore, of the intracellular cell-division dynamics. It also heralds failure of the coarse-grained approximation to accurately describe the dynamics of the system.

To assess the accuracy of the assumption that the age structure of the population is in equilibrium, we have ran simulations of the full stochastic model and compare the empirical birth rate, Eq. (5.3.31), with equilibrium birth rate, Eq. (5.3.33). Results are shown in Fig. 5.7 where we plot the time evolution of probability distribution function (PDF) of the empirical birth rate, as obtained from simulation of the full stochastic multi-scale model. We can see that behind the wave the front (Fig. 5.7(a), (b) and (c)) where cell numbers approach the carrying capacity of the system, the empirical birth rate is reasonably approximated by the equilibrium birth rate. However, closer to and, crucially, ahead of the front, the empirical birth rate exhibits huge fluctuations both above and below the equilibrium birth rate. The latter implies that the age-structure of the population within the compartments located at the edge of wave is strongly off-equilibrium (Fig. 5.7(d), (e) and (f)) his observation explains the reason for the disparity of the wave velocities the coarse-grained mean-field and the stochastic models: the speed of propagation of a travelling wave is critically affected by the behaviour of the region close to the absorbing boundary, just at the edge of wave front. In the

case of our stochastic front, the equilibrium birth rate completely fails to describe the population dynamics in that region, and therefore the speed of the front is determined by stochastic effects associated to non-equilibrium fluctuations of the age distribution. By contrast, when the hybrid model is considered, the coarse-grained mean-field model deals only with the part of the system that is (approximately) in equilibrium. The part of the system whose age distribution is off-equilibrium, i.e. the population at the edge of the wave, is modelled by the full stochastic age-structured model, which provides the actual value of the birth rate. This fact also explains why the hybrid model provides a much more accurate description of the behaviour of the system.

Parameter values

The parameter values associated to the population dynamics are taken from chapter 4: $\nu = 0.0000416667$ min^{-1} and $\tau_p = 480$ min. Estimates for the oxygen diffusion coefficient and the cell diffusion coefficient are $D_c = 10^{-3}$ mm^2/sec and $D_n = 10^{-7}$ mm^2/sec, respectively [176, 194]. The rates of oxygen supply and oxygen consumption are taken to be $S = 1.57 \cdot 10^{-2}$ μM/sec and $k = 1.57 \cdot 10^{-4}$ sec^{-1} (chapter 4). Furthermore, unless otherwise stated, the oxygen decay rate, k_2 is taken so that $\frac{\mathcal{S}}{\kappa_2} = O(1)$. Finally, the carrying capacity, K, is given by:

$$K = \frac{\mathcal{S}}{\kappa c_\infty} \tag{5.5.1}$$

where c_∞ is given by the (unique) solution of:

$$\alpha_{G1/S}(c_\infty, p_6/p_3) = -\log\left(\frac{\tau_p \nu + 1}{2}\right) \tag{5.5.2}$$

with $\alpha_{G1/S}(c_\infty, p_6/p_3)$ is given by Eq. (4.3.57), where we take $p_6/p_3 = 1$.

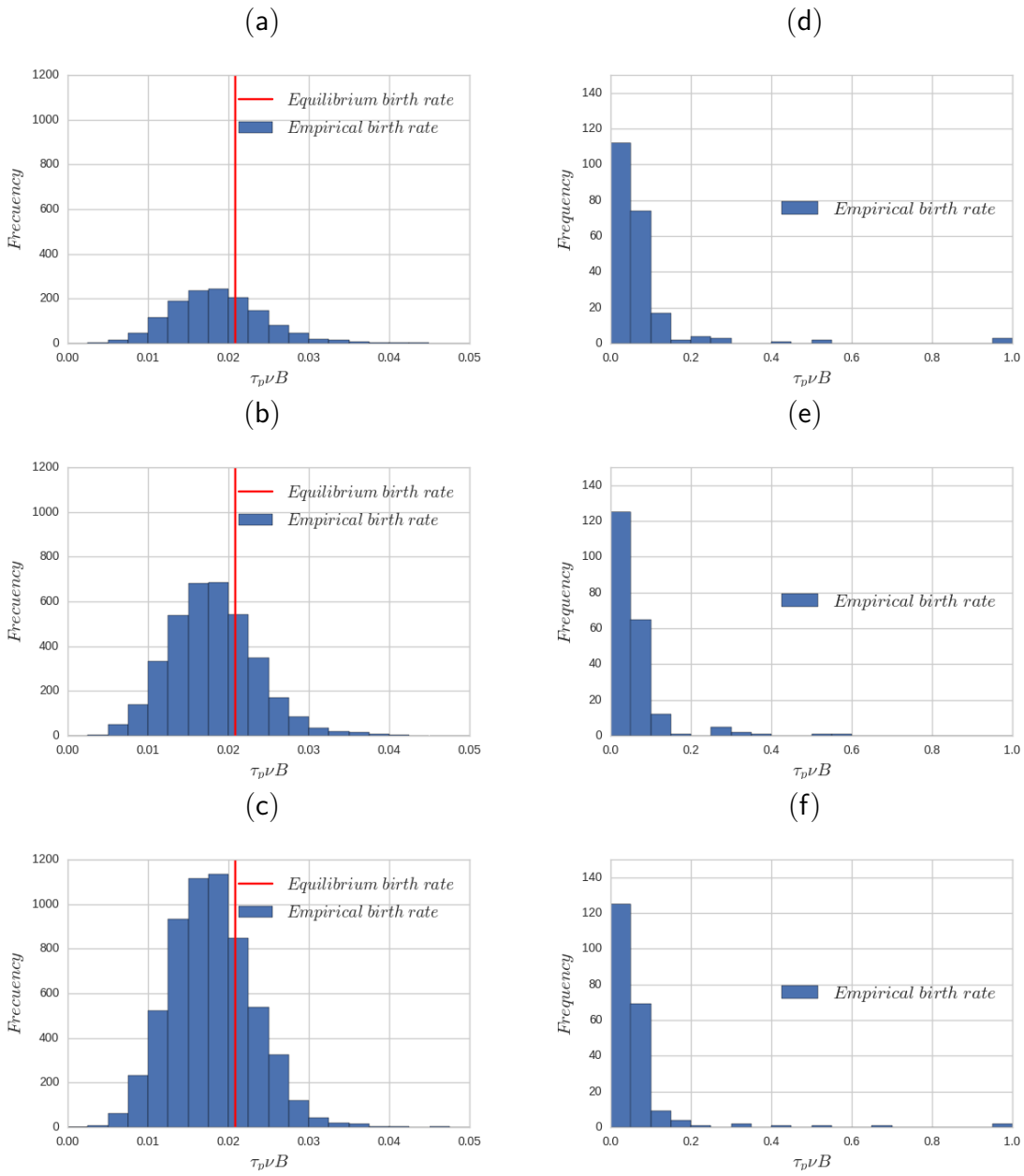

Figure 5.7: Plots showing the time evolution of probability distribution function of the birth rate as obtained from simulation of the full stochastic multi-scale model. We show three snapshots (time increasing from top to down) for the region at the behind the interface (left column) and ahead of the interface (right column). These results show that behind the interface the distribution of the empirical birth rate, calculated using Eq. (5.3.31), is centered around the equilibrium birth rate, Eq. (5.3.33), vertical red line. By contrast, ahead of the interface the birth rate distribution is much broader. Therefore, whereas behind the interface the equilibrium birth rate is a good approximation, this is not the case ahead of the interface. $\Theta = 2000$. For other parameter values see Section 5.5.

Chapter 6

Conclusions & Discussion

6.1 Intracellular level

6.1.1 Intracellular noise and the SCQSSA

By means of the semi-classical quasi-steady state approximation, Section 2.2, we have analysed stochastic effects affecting the onset of bi-stability in cell regulatory systems. Our theory shows that there exists a conserved momentum coordinate associated to each conserved chemical species. In the case of the enzyme-catalysed bistable system, Section 2.3, there are three such conserved momenta, associated to each of the conserved chemical species, i.e. Cdh1 and its activating and inhibiting enzymes.

According to the SCQSSA analysis of [4], the maximum rate achieved by an enzymatic reaction, V_{max}, predicted by the mean-field theory [123] is renormalised by a factor which equals the value of the (constant) momentum coordinate p_i associated to the conserved enzyme: $V_{max}^{(SC)} = p_{e_j} p_i V_{max}$ where $V_{max}^{(SC)}$ is the maximum rate predicted by the SCQSSA. As a consequence of this parameter renormalisation, we have shown that variation in the value of the conserved momenta can trigger bifurcations leading to the onset of bistable behaviour beyond the predictions of the mean-field limit, i.e. for values of parameters where the mean-field limit predicts the system to be mono-stable, the SCQSSA predicts bi-stability, and vice versa (see Figs. 2.2).

Furthermore, we have established that the value of the constant momenta is actually determined by the probability distribution of the associated conserved chemical species, and, ultimately, by the number of molecules of these species (see Eqs. (2.3.22)). Therefore, our theory establishes that the numbers of molecules of the conserved species are order parameters whose variation should trigger (or cancel) bistable behaviour in the associated systems. This prediction is fully confirmed by direct numerical simulation using the stochastic simulation algorithm (see Figs. 2.3, 2.4). Quantitative comparison between the predictions of our asymptotic analysis and the simulation results (see Fig. 2.5) shows that our theoretical approach slightly underestimates the critical value for

the bistable enzyme-regulated system.

Our results allow us to propose a means of controlling cell function. For example, regarding the enzyme-catalysed bistable model analysed in Section 2.3, varying the number of molecules of the three conserved chemical species (Cdh1 and the associated activating and inhibiting enzymes) enables us to lock the system into either of the G_1 or the S-G_2-M stable fixed points or to drive the system into its bistable regime where random fluctuations will trigger switching between these two states. This could be accomplished by ectopically increasing the synthesis of the corresponding molecule or by targeting the enzymes with enzyme-targeted drugs [188, 202].

This result allows us to explore strategies, for example, in the field of combination therapies in cancer treatment. Cellular quiescence is a major factor in resistance to unspecific therapies, such as chemo- and radio-therapy, which target proliferating cells. Bi-stability is central to control cell-cycle progression and to regulate the exit from quiescence, with enzyme catalysis (usually accounted for by (mean-field) Michaelis-Menten, quasi-steady state dynamics) being ubiquitously involved [18, 140, 234, 233]. Our findings will allow us to formulate combination strategies in which chemo- or radio-therapy are combined with a strategy aimed at driving cancer cells into proliferation or quiescence depending on the phase of the treatment cycle. Evaluation of the viability and efficiency of such combination requires the formulation of multi-scale models [6, 89].

Our approach differs from previous work, such as Dykman et al.[53] in a significant aspect, namely, whilst their aim is to estimate the rate of noise-induced transition between metastable states in systems exhibiting multi-stability, the purpose of our analysis is to ascertain whether noise can alter the multi-stability status of the system. Dykman et al.[53] do not address such issue.

Eqs. (2.3.14)-(2.3.17) are derived from a semi-classical approximation of the Master Equation (or its equivalent description in terms or the generating function PDE). This approximation yields a set Hamilton equations (Eqs. (8)-(9)) whose solutions are the optimal fluctuation paths and, as such, they describe fluctuation-induced phenomena which cannot be accounted for by the mean-field approximation. One of the best known examples of this is exit problems from meta-stable states in noisy systems (e.g. extinctions), where the semi-classical approximation provides the optimal escape path from which information such as mean-first passage time or waiting time for extinction can be obtained (see, for example, references [14, 56, 126]). Furthermore, Eqs. (2.3.14)-(2.3.17) are derived from the general Hamilton equations, Eqs. (8)-(9), by means of an approximation based on separation of time scales, not on any mean-field assumption.

A closely related subject to that analysed in this chapter is that of noise-induced bifurcations [67]. Such phenomenon has been studied in biological systems where the mean-field limit does not predict bistability, such as the so-called enzymatic futile

cycles [193] where noise associated to the number of enzymes induce bistability. In the absence of this source of noise, the system does not exhibit bistable behaviour. We have not dealt with such noise-induced phenomena in the present chapter, in the sense that the system analysed in this paper is such that their mean-field limit exhibits bistability. We leave the interesting issue of whether our SCQSSA framework can be used to analyse noise-induced bifurcation phenomena for future research.

6.1.2 Escape from oscillatory steady states

We have shown that, within the rare event theory framework, escape problems from a stable limit cycle can be accurately characterised. The success of the method, in comparison with alternatives, relies on the fact that the Freidlin-Wentzell action is not a local property of the dynamical landscape but of the whole escape trajectory.

For sufficiently large system sizes, we have shown that MAP theory accurately predicts escape trajectories and the escape time distribution. The method has also revealed properties of the escape trajectory, such as the tangent exit of the MAP from the stable limit cycle and tangent entry into the basin of attraction of the stable fixed point, as well as the dependence of the entry and exit points on the parameters of the system.

MAP predictions, whilst better than previously used methods, were less successful in determining the exit angle from the stable limit cycle. A deeper analysis of the exit angle could be carried out through a relaxation of the Laplace condition, i.e. the reduction to an integral along a single optimal path, by further exploring the distribution of suboptimal paths. Additionally, in the absence of a unique point (the saddle) separating the basins of attraction, novel research into the calculation of the prefactor [25] should be extended.

Eventually, the details of the dynamical landscape will be determined by concrete biological systems. For this reason, future work plans include the application of action minimization to stochastic excitable transitions in type II neurons, where rare event theory will prove its predictive power.

6.2 Stochastic multi-scale modelling of cellular populations

6.2.1 Population level: heterogeneous systems

In this chapter, we have presented and studied a stochastic multi-scale model of a heterogeneous, resource-limited cell population. This model accounts for a stochastic intracellular dynamics (in this particular case, a model of the oxygen-regulated

G1/S transition) and an age-structured birth-and-death process for the cell population dynamics. Both compartments are coupled by (i) a model for the time variation of resource (oxygen) abundance which regulates the rate of cell-cycle progression, and (ii) a model of the age-dependent birth rate which carries out the coupling between the intracellular and the cellular compartments (see Fig. 4.1 for a schematic representation of the model and Section 4.2 for a summary of the model formulation).

Our analysis of the stochastic dynamics of the oxygen-regulated G1/S transition, which is a generalisation of the mean-field model presented in [18], has revealed a number of previously unreported properties related to the presence of fluctuations. In particular, the optimal path theory and the quasi-steady state approximation allows us to explore the effect of the SCF-regulating enzymes on the timing of the G1/S transition. The relative abundance of SCF-activating and inhibiting enzymes regulates the rate at which cells reach the G1/S transition: excess of SCF-activating enzyme can delay the transition and even rendering the cell quiescent regardless of oxygen concentration beyond the predictions of the mean-field model (see Sections 4.3.5 & 4.3.5). Furthermore, we have shown that the effects on timing of the G1/S transition of the relative abundance of SCF-activating enzyme give rise to a scaling form dependence of the age to the transition, $a_{G1/S}$, whereby this quantity is a function of $a_{G1/S}(c, p_6/p_3)$ which takes the form of Eq. (4.3.57) (see Section 4.3.6). Taken together, these results imply that stochasticity in the intracellular dynamics naturally generates variability within the population: an otherwise homogeneous population presents a distribution of birth rates induced by variability in the relative abundance of SCF-activating enzyme within the population of cells.

This variation in the duration of the cell-cycle allows us to analyse the dynamics of a stochastic heterogeneous population under resource limitation conditions. To this end, we consider populations formed by sub-populations of cells characterised by differing relative abundance of SCF-activating and inhibiting enzymes. We further assume that this heterogeneity is heritable (i.e. daughter cells inherited the ratio of SCF-regulating enzymes from their mother). In this scenario, we have shown sub-populations within heterogeneous population engage in quasi-neutral competition: sub-populations of cells get extinct in an average time which is of the order of the carrying capacity of the system (see Section 4.5.2). In the context of modelling cancer cells populations, where heterogeneity is a main contributor to the complex dynamics of cancer [10, 11, 80, 87, 155], this result is of relevance since it allows us to estimate the rate at which sub-populations or clones disappear from the tumour. The fact that this rate is proportional to the inverse of the carrying capacity reveals a highly dynamical scenario where clones are quickly decaying and being replaced within the tumour. This can have a profound impact in a variety of evolutionary phenomena such as emergence of drug resistant phenotypes. From the modelling perspective, we should note that quasi-neutral competition is a purely stochastic scenario: the mean-field limit predicts coexistence between the corresponding cell types.

We have further explored the issue of emergence of drug resistant cell types by analysing a case study in which a quiescent population can be rescued from latency by the application of a cell-cycle dependent therapy. Examples of such therapies are radiotherapy or cytotoxic drugs designed to target cells in specific stages of cell cycle progression [179]. In the particular example analysed in Section 4.6, we have shown that in mixed population composed by active (proliferating) and quiescent cells, if the drug is not efficient enough (characterised in terms of its associated survival fraction, F_S), quiescent cells are rescued from latency and eventually reach fixation within the population, i.e. the activated quiescent cells out-compete the original active cells until the latter population becomes extinct [7]. It is noteworthy the fact that in this process of quiescence rescue the original cancer population is replaced by a much more resistant population as the activated quiescent cells are less sensitive to the therapy than the original active cells.

Our results show that the methods and models presented in this paper are of great potential importance for the analysis of the complex dynamics of heterogeneous populations under resource limitation, in particular for the study of emergence of drug resistance in heterogeneous cancer cell populations. Several important issues have been left out of the present work. A major contributor to heterogeneity within a cancer cell population is spatial heterogeneity [10, 80] which is closely related to micro-environmental heterogeneity. A further issue which should be analysed in depth concerns the scaling properties of the age to the G1/S transition (see Section 4.3.6), in particular whether this is a general property of the cell-cycle dynamics or rather a specific attribute of the stochastic model presented here. A thorough analysis of these issues falls beyond the scope of the present paper and are left for future research.

6.3 Population level: spatially heterogenous systems

The development of hybrid methodologies is a current field of current interest in both multi-scale modelling and stochastic reaction-diffusion systems, particularly regarding their applications to model biological systems. In this paper, we have proposed a hybrid methodology for a stochastic multi-scale model of tumour growth, i.e. a population-dynamical model which accounts for the effects of intrinsic noise affecting both the number of cells and the intracellular dynamics, associated in our model to cell proliferation (cell cycle). In order to formulate this method, we have developed an asymptotic theory which, taking into account the hierarchy of characteristic time scales and their separation, allows us to formulate a coarse-grained approximation for both the full stochastic model and its mean-field limit. This coarse-grained approximation involves averaging out the age-structure (which accounts for the multi-scale nature of the model) by assuming that the age distribution of the population settles

onto equilibrium very fast compared with the time scales associated with cell motility.

Our hybrid model consists of coupling the coarse-grained mean-field model to the full stochastic simulation. By doing so, we are neglecting noise in both cell numbers (population) and their birth rates (structure). This means that, in addition to the issues that arise in stochastic-reaction diffusion systems, we need to account for the age-structure of the population when attempting to couple both descriptions. In this case, we exploit the nature of our coarse-graining strategy, namely, the fact that in the mean-field region the age-distribution is in equilibrium, of which we know its explicit form. This very much simplifies the coupling between both regimes, as upon transference of cells from the mean-field to the stochastic regime we just to sample the equilibrium age distribution.

In order to check the accuracy of both the coarse-grained and the hybrid approximations, we have chosen to study a particular situation of interest in many biological problems, including tumour growth: the propagation of travelling waves. By taking as a benchmark the solution of the full stochastic model by means of the age-structured Gillespie algorithm previously formulated in chapter 4, we have been able to test both approaches for their accuracy in reproducing the behaviour of the moving front in terms of its position and velocity. The first observation we make is that the travelling wave velocity predicted by the mean-field coarse-grained model (where fluctuations in both population and birth rate are averaged out and thus not considered) is way off the benchmark. In fact, inaccuracies are larger than those expected from fluctuations in cell numbers alone. In view of this, we have investigated whether spatially-heterogeneous fluctuations of the birth rate are responsible for these discrepancies. Indeed, we have found that whereas such fluctuations have a modest effect behind the interface (i.e. in the mean-field region), noise associated to the birth rate is much larger ahead of the interface (i.e. in the stochastic region). The hybrid method, by incorporating the appropriate model of the birth rate in the different regions, leads to a much more faithful description of the dynamics of the full system than the coarse-grained limit alone.

We have thus formulated a method that extends the remit of existing hybrid methods for stochastic reaction-diffusion systems. A number of possible lines of improvement are shared with hybrid methods for reaction-diffusion systems: consistent ways to set the position of the interface (e.g. based on quantification of the local fluctuations), use of a convergent version of the Master Equation rather the regular reaction-diffusion Master Equation, whose mean-field limit only converges to the associated reaction diffusion PDE in 1D [113], and extension to finite-element or unstructured meshes [57], among others. Other extensions of the current method are specific to the presence of structure variables, which reflect the multi-scale nature of the system. In particular, we need to explore the inclusion of more general structure variables (size, physiological, etc.) [44, 177, 178], for which the coarse-graining is likely to be more challenging. All these issues will be the subject matter of future research.

Our method has the additional merit of allowing us to explore the effects of intracellular noise, i.e. fluctuations in the birth rate associated with an out-of-equilibrium age distribution, on collective properties such as the speed of the travelling wave. We have showed that the interplay between population and structure noise results in large fluctuations of the birth rate in the region at the leading edge of front, which cannot be accounted for by the coarse-grained model. Such fluctuations have non-trivial effects of the speed of the wave. This leads us to conclude that the consideration of birth-rate fluctuations is necessary for a quantitatively accurate description of invasive phenomena such as tumour progression.

Annex

Appendix A

Minimun Action Path: numeric algorithm

To calculate numerically the minimum of (3.4.2), we discretise the continuous path φ_τ in N straight segments (equally spaced over time, $\Delta t = \tau/N$, where τ is the total path time). Let $\{\phi_0, \phi_1, ..., \phi_N\}$ the positions of the borders of that segments. The expresion of (3.4.2), after this approximation, results:

$$\mathcal{S}(\varphi_\tau) = \frac{1}{2}\sum_{i=1}^{N}\sum_{j=1}^{2}\frac{(\dot{\varphi}_i^j - f_i^j)^2}{D_i^j}, \tag{A.0.1}$$

where f_i^j and D_i^j are the j-component of the deterministic field (3.4.3) and the diagonal diffusion tensor (3.4.4), respectively, evaluated in the centre of i-th segment $(\phi_{i-1} + \phi_i)/2$, and $\dot{\varphi} = (\phi_i - \phi_{i-1})/\Delta t$ the velocity. If the total time (τ), the initial position (ϕ_0) and final position (ϕ_N) are fixed, (A.0.1) can be minimised by means of quasi-Newtonian method, using the analytic expression for the derivative of the action on the j-th direction in each ϕ_n:

$$\begin{aligned}\frac{\partial \mathcal{S}}{\partial \phi_n^j} = \frac{\dot{\varphi}_n^j - f_n^j}{D_n^j} - \frac{\dot{\varphi}_{n+1}^j - f_{n+1}^j}{D_{n+1}^j} - \frac{\Delta t}{2}\sum_{k=1}^{2}\Bigg[\frac{\dot{\varphi}_{n+1}^k - f_{n+1}^k}{D_{n+1}^k}f_{j,n+1}^{\prime k} + \\ + \frac{\dot{\varphi}_n^k - f_n^k}{D_n^k}f_{j,n}^{\prime k} + \frac{(D')_{j,n+1}^k}{2(D^2)_{j,n+1}^k}(\dot{\varphi}_{n+1}^k - f_{n+1}^k)^2 + \frac{(D')_{j,n}^k}{2(D^2)_{j,n}^k}(\dot{\varphi}_n^k - f_n^k)^2\Bigg]\end{aligned} \tag{A.0.2}$$

where $f_{n,j}^{\prime k}$ and $D_{n,j}^{\prime k}$ are the derivative in the j direction of the k-th component of the deterministic field (3.4.3) and the diffusion tensor (3.4.4), respectively, of the n-th segment. The misimisation of (3.4.3) (2x(N-2) freedom degrees) is solved using L-BFGS algorithm [61, 65], obtain a minimum of the action S_τ for a certain τ. For obtaining the minimal action, we use a custom made line search method over S_τ.

Appendix B

Publications

B.1 Published Papers

Roberto de la Cruz, Pilar Guerrero, Fabian Spill, Tomás Alarcón, *Stochastic multi-scale models of competition within heterogeneous cellular populations: Simulation methods and mean-field analysis*, Journal of Theoretical Biology 407, 161-183 (2016).

Roberto de la Cruz, Pilar Guerrero, Fabian Spill, Tomás Alarcón, *The effects of intrinsic noise on the behaviour of bistable cell regulatory systems under quasi-steady state conditions*, The Journal of Chemical Physics 143, 074105 (2015).

B.2 Submitted Papers

Roberto de la Cruz, Rubén Pérez-Carrasco, Pilar Guerrero, Tomás Alarcón, Karen Page, *Prediction of rare stochastic switching in presence of limit cycles follow an action minimisation*, submitted to Physical Review Letters.

Roberto de la Cruz, Pilar Guerrero, Juan Calvo, Tomás Alarcón, *Coarse-graining and hybrid methods for efficient simulation of stochastic multi-scale models of tumour growth*, submitted to Journal Computational Physics.

Bibliography

[1] Mark J Ablowitz and A S Fokas. *Complex variables. Introduction and applications*. Cambridge University Press, Cambridge, UK, 2003.

[2] Murat Acar, Jerome T Mettetal, and Alexander van Oudenaarden. Stochastic switching as survival strategy in fluctuating environments. *Nature Gen.*, 40:471–475, 2008.

[3] Bissan Al-Lazikani, Udai Banerji, and Paul Workman. Combinatorial drug therapy for cancer in the post-genomic era. *Nat. Biotechnology*, 30:679–692, 2012.

[4] Tomás Alarcón. Stochastic quasi-steady state approximations for asymptotic solutions of the Chemical Master Equation. *J. Phys. Chem.*, 140:184109, 2014.

[5] Tomás Alarcón, Helen M Byrne, and Philip K Maini. A mathematical model of the effects of hypoxia on the cell-cycle of normal and cancer cells. *J. theor. Biol.*, 229:395–411, 2004.

[6] Tomás Alarcón, Helen M Byrne, and Philip K Maini. A multiple scale model of tumour growth. *Multiscale Model. Sim.*, 3:440–475, 2005.

[7] Tomás Alarcón and Henrik Jeldtoft Jensen. Quiescence: A mechanism for escaping the effects of drug on cell populations. *J. R. Soc. Interface*, 8:99–106, 2010.

[8] Tomás Alarcón and Karen M Page. Mathematical models of the VEGF receptor and its role in cancer therapy. *J. R. Soc. Interface*, 4:283–304, 2007.

[9] Bruce Alberts, Alexander Johnson, Julian Lewis, Martin Raff, Keith Roberts, and Peter Walter. *Molecular Biology of the Cell*. Garland Publishing Inc., New York, 4th edition, 2002.

[10] A R A Anderson, A M Weaver, P T Cummings, and V Quaranta. Tumor morphology and phenotypic evolution driven by selective pressure from the microenvironment. *Cell*, 127:905–915, 2006.

[11] Alexander R A Anderson and Vitto Quaranta. Integrative mathematical oncology. *Nature Rev. Cancer*, 8:763–773, 2008.

[12] David F Anderson and Thomas G Kurtz. *Stochastic analysis of biochemical systems*. Springer, New York, NY, 2015.

[13] Michael Assaf and Baruch Meerson. Spectral formulation and WKB approximation for rare-event statistics in reaction systems. *Phys. Rev. E*, 74:41115, 2006.

[14] Michael Assaf, Baruch Meerson, and Pavel V Sasorov. Large fluctuations in stochastic population dynamics: Momentum space calculations. *J. Stat. Mech.*, page P07018, 2010.

[15] Michael Assaf, Elijah Roberts, and Zaida Luthey-Schulten. Determining the stability of genetic switches: explicitly accounting for mRNA noise. *Physical review letters*, 106(24):248102, 2011.

[16] Gabor Balazsi, Alexander van Oudenaarden, and James J Collins. Cellular decision making and biological noise: from microbes to mammals. *Cell*, 144:910–925, 2011.

[17] Karen Ball, Thomas G Kurtz, Lea Popovic, and Greg Rempala. Asymptotic analysis of multi-scale approximations to reaction networks. *Ann. App. Prob.*, 16:1925–1961, 2006.

[18] Baptiste Bedessem and Angelique Stephanou. A mathematical model of HIF-1-α-mediated response to hypoxia on the G1/S transition. *Math. Biosci.*, 248:31–39, 2014.

[19] Nils Berglund. Noise-Induced Phase Slips, Log-Periodic Oscillations, and the Gumbel Distribution. *Markov Processes Relat. Fields*, 22(3):467–505, 2016.

[20] Nils Berglund and Barbara Gentz. On the Noise-Induced Passage through an Unstable Periodic Orbit II: General Case. *SIAM Journal on Mathematical Analysis*, 46(1):310–352, 2014.

[21] D Bernstein. Simulating mesoscopic reaction-diffusion systems using the gillespie algorithm. *Physical Review E*, 71:041103, 2005.

[22] F Billy and J Clairambault. Designing proliferating cell population models with functional targets for control by anti-cancer drugs. *Discrete and Continuous Dynamical Systems - Series B*, 18:865–889, 2013.

[23] Katarina Bodova, David Paydarfar, and Daniel B Forger. Characterizing spiking in noisy type {II} neurons. *Journal of Theoretical Biology*, 365:40–54, 2015.

[24] D B Botkin, J F Janak, and J R Wallis. Some ecological consequences of a computer model of forest growth. *J. Ecol.*, 60:849–873, 1972.

[25] Freddy Bouchet and Julien Reygner. Generalisation of the Eyring-Kramers transition rate formula to irreversible diffusion processes. *Ann. Henri Poincare*, 17:3499–3532, 2016.

[26] Paul C Bressloff. *Stochastic processes in cell biology.* Springer-Verlag, Berlin, Germany., 2014.

[27] Paul C Bressloff and Jay M Newby. Path integrals and large deviations in stochastic hybrid systems. *Phys. Rev. E*, 89:42701, 2014.

[28] H P Breuer, W Huber, and F Petruccione. Fluctuation effects on wave propagation in a reaction-diffusion process. *Physica D: Nonlinear Phenomena*, 73:259–273, 1994.

[29] George E Briggs and John B S Haldane. A note on the kinetics of enzyme action. *Biochem. J.*, 19:338–339, 1925.

[30] Robert G Bristow and Richard P Hill. Hypoxia, DNA repair and genetic instability. *Nature Rev. Cancer*, 8:180–192, 2008.

[31] Maria Bruna, S Jonathan Chapman, and Matthew J Smith. Model reduction for slow-fast stochastic systems with metastable behaviour. *J. Chem. Phys.*, 140:174107, 2014.

[32] E Brunet and B Derrida. Effect of microscopic noise on front propagation. *Journal of Statistical Physics*, 103:269–282, 2001.

[33] Kevin Burrage, Tianhai Tian, and Pamela Burrage. A multi-scaled approach for simulating chemical reaction systems. *Progr. Biophys. Mol. Biol.*, 85:217–234, 2004.

[34] Helen M Byrne. Dissecting cancer through mathematics: From the cell to the animal model. *Nature Rev. Cancer*, 10:221–230, 2010.

[35] Long Cai, Chiraj K Dalal, and Michael B Elowitz. Frequency-modulated nuclear localisation bursts coordinate gene regulation. *Nature*, 455:485–490, 2008.

[36] Yang Cao, Daniel T Gillespie, and Linda R Petzold. Multiscale stochastic simulation algorithm with stochastic partial equilibrium assumption for chemically reacting systems. *J. Comp. Phys.*, 206:395–411, 2005.

[37] Yang Cao, Daniel T Gillespie, and Linda R Petzold. The slow-scale stochastic simulation algorithm. *J. Chem. Phys.*, 122:14116, 2005.

[38] S J Chapman, R J Shipley, and R Jawad. Multiscale modeling of fluid transport in tumors. *Bulletin of Mathematical Biology*, 70:2334–2357, 2008.

[39] R H Chisholm, T Lorenzi, A Lorz, A K Larsen, L N de Almedia, A Escargueil, and J Clairambault. Tumor morphology and phenotypic evolution driven by selective pressure from the microenvironment. *Cancer Res.*, 75:930–939, 2015.

[40] Olivier Cinquin and Jaques Demongeot. High-dimensional switches and the modeling of cellular differentiation. *J. theor. Biol.*, 233:391–411, 2005.

[41] J G Conlon and C R Doering. On travelling waves for the stochastic fisher–kolmogorov–petrovsky–piscunov equation. *Journal of statistical physics*, 120:421–477, 2005.

[42] K Curtius, W D Hazelton, J Jeon, and E G Luebeck. A Multiscale Model Evaluates Screening for Neoplasia in Barrett's Esophagus. *PLoS Comput. Biol.*, 11:e1004272, 2015.

[43] K. Danesh, R. Durrett, L. Havrilesky, and E. Myers. A branching process model of ovarian cancer. *J. Theor. Biol.*, 314:10–15, 2012.

[44] A M de Roos. *A Gentle Introduction to Physiologically Structured Population Modelsl*. Springer US, Boston, MA, 1997.

[45] Z Deisboeck, Z Wang, P Macklin, and V Cristini. Multi-scale cancer modeling. *Annu. Rev. Biomed. Eng.*, 13:127–155, 2011.

[46] Ronald Dickman and Ronaldo Vidigal. Path integrals and perturbation theory for stochastic processes. *Brazilian J. Phys.*, 33:73–93, 2003.

[47] J J DiStefano. *Dynamic Systems Biology Modeling and Simulation*. Elsevier Science, 2015.

[48] Susanne Ditlevsen and Priscilla Greenwood. The Morris–Lecar neuron model embeds a leaky integrate-and-fire model. *Journal of Mathematical Biology*, 67(2):239–259, 2013.

[49] C R Doering, K V Sargsyan, and L M Sander. Extinction Times for Birth-Death Processes: Exact Results, Continuum Asymptotics, and the Failure of the Fokker–Planck Approximation. *Multiscale Model. Sim.*, 3:283–299, 2005.

[50] Éva Dóka and Gábor Lente. Stochastic mapping of the Michaelis-Menten mechanism. *J. Chem. Phys.*, 136:54111, 2012.

[51] D Drasdo and S Hoehme. A single-cell based modeling of tumor growth in vitro: Monolayers and spheroids. *Phys Biol*, 2:133–147, 2005.

[52] R Durrett. Cancer modeling: A personal perspective. *Noticies of the AMS*, 60:304–309, 2013.

[53] Mark I Dykman, Eugenia Mori, John Ross, and P M Hunt. Large fluctuations and optimal paths in chemical kinectics. *J. Chem. Phys.*, 100(8):5735–5750, 1994.

[54] Weinan E, Di Liu, and Eric Vanden-Eijnden. Nested stochastic simulation algorithms for chemical kinetic systems with multiple time scales. *J. Comp. Phys.*, 221:158–170, 2007.

[55] Avigdor Eldar and Michael B Elowitz. Functional roles of noise in genetic circuits. *Nature*, 467:167–173, 2010.

[56] Vlad Elgart and Alex Kamenev. Rare events in reaction-diffusion systems. *Phys. Rev. E*, 70:41106, 2004.

[57] S Engblom, L Ferm, A Hellander, and P Lötstedt. Simulation of stochastic reaction-diffusion processes on unstructured meshes. *SIAM Journal on Scientific Computing*, 31:1774–1797, 2009.

[58] James E Ferrel and Wen Xiong. Bistability in cell signalling: How to make continuous processes discontinuous, and reversible processes irreversible. *Chaos*, 11:227–236, 2001.

[59] Richard P Feynman and Albert R Hibbs. *Quantum Mechanics and Path Integrals*. Dover Publications, Mineola, NY, USA, 2010.

[60] M B Flegg, S J Chapman, and R Erban. Two regime method for optimizing stochastic reaction-diffusion simulations. *J. R. Soc. Interface*, 9:859–868, 2012.

[61] R Fletcher. *Practical Methods of Optimization*. Wiley, 2000.

[62] B Franz, M B Flegg, S J Chapman, and R Erban. Multiscale reaction-diffusion algorithms: PDE assisted brownian dynamics. *SIAM J. Appl. Math.*, 73:1224–1247, 2013.

[63] Mark I Freidlin and Alexander D Wentzell. *Random perturbations of dynamical systems*. Springer-Verlag, New York, NY, USA., 1998.

[64] P Gabriel, S P Garbett, V Quaranta, D R Tyson, and G F Webb. The contribution of age structure to cell population responses to targeted therapeutics. *J. Theor. Biol.*, 311:19–27, 2012.

[65] M Galassi et al. *GNU Scientific Library Reference Manual - Third Edition*. Network Theory Ltd., 2009.

[66] J Galle, M Loeffler, and D Drasdo. Modelling the effect of deregulated proliferation and apoptosis on the growth dynamics of epithelial cell populations in vitro. *Biophys J*, 88:62–75, 2005.

[67] Jordi García-Ojalvo and José María Sancho. *Noise in spatially-extended systems*. Springer-Verlag, 1999.

[68] Crispin W Gardiner. *Stochatic methods*. Springer-Verlag, Berlin, Germany, 2009.

[69] R A Gatenby and E T Gawlinski. A reaction-diffusion model of cancer invasion. *Cancer Res.*, 56:5745–5753, 1996.

[70] Robert A Gatenby and Thomas L Vincent. Application of quantitative models from population biology and evolutionary game theory to tumor therapeutic strategies. *Mol. Cancer Ther.*, 2:919–927, 2003.

[71] Claude Gerard and Albert Goldbeter. Temporal self-organisation of the cyclin/CDK network driving the mammalian cell cycle. *Proc. Natl. Acad. Sci.*, 106:21643–21648, 2009.

[72] Claude Gerard and Albert Goldbeter. A skeleton model for the network of cyclin-dependent kinases driving the mammalian cell cycle. *Interface Focus*, 1:24–35, 2011.

[73] Claude Gerard and Albert Goldbeter. From quiescence to proliferation: Cdk oscillations drive mammalian cell-cycle. *Frontiers in Physiology*, 3:413, 2012.

[74] Claude Gerard and Albert Goldbeter. The balance between cell cycle arrest and cell proliferation: control by extracellular matrix and by conatct inhibition. *Interface Focus*, 4:20130075, 2014.

[75] Claudeand Gerard, John J Tyson, Damien Coudreuse, and Bela Novak. Cell cycle control by a minimal cdk network. *PLoS Comput. Biol.*, 11:e1004056, 2015.

[76] Daniel T. Gillespie. A general method for numerically simulating the stochastic time evolution of coupled chemical reactions. *Journal of Computational Physics*, 22(4):403–434, 1976.

[77] Daniel T Gillespie. Exact stochastic simulation of coupled chemical reactions. *The journal of physical chemistry*, 81:2340–2361, 1977.

[78] Daniel T. Gillespie. The chemical Langevin equation. *The Journal of Chemical Physics*, 113(1):297, 2000.

[79] Daniel T Gillespie. Approximate accelerated stochastic simulation of chemically reacting systems. *J. Chem. Phys.*, 155:1716–1733, 2001.

[80] R J Gillies, D Verduzco, and R Gatenby. Evolutionary dynamics of carcinogenesis and why targeted therapy does not work. *Nature Rev. Cancer*, 12:487–493, 2012.

[81] N Goda, S J Dozier, and R S Johnson. HIF-1 in Cell Cycle Regulation, Apoptosis, and Tumor Progression. *Antioxidants & Redox Signaling*, 5:467–473, 2003.

[82] Albert Goldbeter. A Model for Circadian Oscillations in the Drosophila Period Protein (PER). *Proceedings of the Royal Society of London B: Biological Sciences*, 261(1362):319–324, 1995.

[83] Albert Goldbeter. *Biochemical oscillations and cellular rhythms : the molecular bases of periodic and chaotic behaviour*. Cambridge University Press, Cambridge, New York, 1996.

[84] Nigel Goldenfeld. *Lectures on phase transitions and the renormalisation group*. Perseus Books Publishing, Reading, Mass., USA, 1992.

[85] D Gonze, J Halloy, and P Gaspard. Biochemical clocks and molecular noise: Theoretical study of robustness factors. *J. Chem. Phys.*, 116:10997–11010, 2002.

[86] T.I. Goonewardene, H.M. Sowter, and A.L. Harris. Hypoxia-induced pathways in breast cancer. *Micros. Res. Tech.*, 59:41–48, 2002.

[87] M Greaves and C C Maley. Clonal evolution in cancer. *Nature*, 481:306–313, 2012.

[88] Geoffrey R Grimmett and David R Stirzaker. *Probability and random processes*. Oxford University Press, 2001.

[89] Pilar Guerrero and Tomás Alarcón. Stochastic multi-scale modelling of cell populations: Asymptotic and numerical methods. *Math. Model. Nat. Phen.*, 10:64–93, 2015.

[90] Pilar Guerrero, Helen M Byrne, Philip K Maini, and Tomás Alarcón. From invasion to latency: Intracellular noise and cell motility as key controls of the competition between resource-limited cellular populations. *J. Math. Biol.*, 72:123–156, 2016.

[91] Douglas Hanahan and Robert A Weinberg. The Hallmarks of Cancer. *Cell*, 100:57–70, 2000.

[92] Douglas Hanahan and Robert A Weinberg. Hallmarks of Cancer: The Next Generation. *Cell*, 144:646–674, 2011.

[93] P.E. Hand and B.E. Griffith. Adaptative multiscale model for simulatin cardiac conduction. *Proc. Natl. Acad. Sci.*, 107:14603–14608, 2010.

[94] A.L. Harris. Hypoxia – a key regulatory factor in tumour growth. *Nat. Rev. Cancer*, 2:38–47, 2002.

[95] J.F. Harris, A.F. Chambers, V Ling, and R.P. Hill. Dynamic heterogeneity: characterization of two cell lines derived from experimental lung metastases of mouse KHT fibrosarcoma. *Invasion Metastasis*, 7:217–229, 1987.

[96] Eric L Haseltine and James B Rawlings. Approximate simulation of coupled fast and slow reactions for stochastic chemical kinetics. *J. Chem. Phys.*, 117:6959–6969, 2002.

[97] H Hatzikirou, L Brusch, C Schaller, M Simon, and A Deutsch. Prediction of traveling front behavior in a lattice-gas cellular automaton model for tumor invasion. *Comput. Math. Appl.*, 59:2326–2339, 2010.

[98] A Hellander, Hellander S, and P Lotstedt. Coupled mesoscopic and microscopic simulation of reaction-diffusion processes in mixed dimensions. *Multiscale Model. Sim.*, 10:585–611, 2012.

[99] S.D. Hester, J.M. Belmonte, J.S. Gens, S.G. Clendenon, and J.A. Glazier. A multi-cell, multi-scale model of vertebrate segmentation and somite formation. *PLoS Comput. Biol.*, 7:e1002155, 2011.

[100] J Hidalgo, S Pigolotti, and M A Muñoz. Stochasticity enhances the gaining of bet-hedging strategies in contact-process-like dynamics. *Phys. Rev. E*, 91:032114, 2015.

[101] R.P. Hill, A.F. Chambers, V Ling, and J.F. Harris. Dynamic heterogeneity: rapid generation of metastatic variants in mouse B16 melanoma cells. *Science*, 224:998–1001, 1984.

[102] P Hitczenko and G S Medvedev. The Poincare map of randomly perturbed periodic motion. *J. Nonlin. Sci.*, 23:835–861, 2013.

[103] M Hockel, K Schlenger, B Aral, M Mitze, U Schaffer, and P Vaupel. Association between Tumor Hypoxia and Malignant Progression in Advanced Cancer of the Uterine Cervix. *Cancer Res.*, 56:4509–4515, 1996.

[104] H Holden, B Øksendal, J Uboe, and T Zhang. *Stochastic partial differential equations. A modeling, white noise functional approach.* Springer, New York, NY, USA., 2010.

[105] Frank C Hoppensteadt. *Mathematical theories of populations: demographics, genetics and epidemics.* Society for Industrial and Applied Mathematics, 1975.

[106] Sui Huang. The molecular and mathematical basis of Wadington's epigenetic landscape: a framework for post-Darwinian biolgy? *BioEssays*, 34:149–157, 2012.

[107] M E Hubbi, D M Gilkes, H Hua, Kshitiz, I Ahmed, and G L Semenza. Cyclin-dependent kinases regulate lysosomal degradation of hypoxia-inducible factor 1a to promote cell-cycle progression. *Proc. Natl. Acad. Sci.*, 111:E3325–E3334, 2014.

[108] T.J. Hudson et al. International network of cancer genome projects. *Nature*, 464:993–998, 2010.

[109] A Hunt and C Wissel. The simulation of the movement of fish schools. *J. Theor. Biol.*, 156:365–385, 1992.

[110] A Hunt and C Wissel. The simulation of fish schools in comparison with experimental data. *Ecol. Model.*, 75–76:135–146, 1994.

[111] Y Inada and K Kawachi. Order and flexibility in the motion of fish schools. *J. Theor. Biol.*, 214:371–387, 2002.

[112] S A Isaacson. The reaction-diffusion master equation as an asymptotic approximation of diffusion to a small target. *SIAM Journal on Applied Mathematics*, 70:77–111, 2009.

[113] S A Isaacson. A convergent reaction-diffusion master equation. *J. Chem. Phys.*, 139:054101, 2013.

[114] Johannes Jaeger and Nick Monk. Bioattractors: dynamical systems theory and the evolution of regulatory processes. *J. Physiol.*, 592:2267–2281, 2014.

[115] N Jagiella, B Muller, M Muller, I E Vignon-Clementel, and D Drasdo. Inferring Growth Control Mechanisms in Growing Multi-cellular Spheroids of NSCLC Cells from Spatial-Temporal Image Data. *PLoS Comput. Biol.*, 12:e1004412, 2016.

[116] Y Jiang, J Pjesivac-Grbovic, C Cantrell, and J.P. Freyer. A multiscale model for avascular tumor growth. *Biophys. J.*, 89:3884–3894, 2005.

[117] Yang Jiao and Salvatore Torquato. Emergent behaviours from a cellular automaton model for invasive tumour growth in heterogeneous microenvironments. *PLoS Comput. Biol.*, 7:e1002314, 2011.

[118] Mads Kaern, Timothy C Elston, William J Blake, and James J Collins. Stochasticity in gene expression: from theories to phenotypes. *Nature Rev. Gen.*, 6:451–464, 2005.

[119] Tibor Kalmar, Chea Lim, Penelope Hayward, Silvia Munoz-Descalzo, Jennifer Nichols, Jordi Garcia-Ojalvo, and Alfonso Martinez-Arias. Regulated fluctuations in Nanog expression mediate cell fate decisions in embryonic stem cells. *PLoS Biol.*, 7:e1000149, 2009.

[120] N G Van Kampen. *Stochastic processes in Physics and Chemistry*. Elsevier, The Netherlands, 2007.

[121] Hye-Won Kang and Thomas G Kurtz. Separation of time-scales and model reduction for stochastic reaction networks. *The Annals of Applied Probability*, 23(2):529–583, 2013.

[122] Stuart A Kauffman. *The origins of order*. Oxford University Press, New York, U.S.A., 1993.

[123] James Keener and James Sneyd. *Mathematical physiology*. Springer-Verlag, New York, NY, USA, 1998.

[124] H Kempf, M Bleicher, and M Meyer-Hermann. Spatio-temporal dynamics of hypoxia during radiotherapy. *PLoS One*, 10:e0133357, 2015.

[125] Thomas B Kepler and Timothy C Elston. Stochasticity in transcriptional regulation: origins, consequences, and mathematical representations. *Biophys. J.*, 81:3116–3136, 2001.

[126] M Khasin and M I Dykman. Extinction Rate Fragility in Population Dynamics. *Phys. Rev. Lett.*, 103:68101, 2009.

[127] Y J Kim and H G Othmer. A hybrid model of tumour-stromal interactions in breast cancer. *Bull. Math. Biol.*, 5:1304–1350, 2013.

[128] Y J Kim and H G Othmer. Hybrid models of cell and tissue dynamics in tumor growth. *Math. Biosci. Eng.*, 17:1141–1156, 2014.

[129] Y J Kim, M A Stolarska, and H G Othmer. A hybrid model for tumor spheroid growth in vitro I: Theoretical development and early results. *Math. Mod. Meth. Appl. Sci.*, 17:1773–1798, 2007.

[130] Marek Kimmel and David E Axelrod. *Branching processes in Biology*. Springer-Verlag, New York, U.S.A., 2002.

[131] Hiroaki Kitano. Cancer as robust system: implications for anticancer therapy. *Nat. Rev. Cancer*, 4:227–235, 2004.

[132] S Kizaka-Kondoh, M Inoue, H Harada, and M Hiraoka. Tumor hypoxia: a target for selective cancer therapy. *Cancer Sci.*, 94:1021–1028, 2003.

[133] 0 Kogan, M Khasin, B Meerson, D Schneider, and C R Myers. Two-strain competition in quasineutral stochastic disease dynamics. *Phys. Rev. E*, 90:042149, 2014.

[134] M Koshiji, Y Kageyama, E A Pete, I Horikawa, J C Barrett, and L E Huang. HIF-1a induces cell cycle arrest by functionally counteracting Myc. *EMBO J.*, 23:1949–1956, 2004.

[135] Ryogo Kubo, Kazuhiro Matsuo, and Kazuo Kitahara. Fuctuation and relaxation of macrovariables. *J. Stat. Phys.*, 9:51–96, 1973.

[136] H Kunz and C K Hemelrijk. Artificial fish schools: collective effects of school size, body size, and form. *Artif. Life*, 9:237–253, 2002.

[137] T G Kurtz. Strong approximation theorems for density dependent markov chains. *Stochastic Processes and their Applications*, 6:223–240, 1978.

[138] Edo Kussell and Stanislas Leibler. Phenotypic diversity, population growth, and information in fluctuating environments. *Science*, 309:2075–2078, 2005.

[139] S Land, S.A. Niederer, W.E. Louch, O.M. Sejersted, and N.P. Smith. Integrating multi-scale data to create a virtual physiological mouse heart. *J. R. Soc. Interface Focus*, 3:20120076, 2013.

[140] Tae J Lee, Guang Yao, Dorothy C Bennett, Joseph R Nevins, and Lingchong You. Stochastic E2F activation and reconciliation of phenomenological cell-cycle models. *PLoS Biology*, 8:e1000488, 2010.

[141] Stephan Legewie, Nils Bluthgen, and Hanspeter Herzel. Mathematical modelling identifies inhibitors of apoptosis as mediators of positive feed-back and bistability. *PLoS Comp. Biol.*, 2:e120, 2006.

[142] Stephan Legewie, Nils Bluthgen, and Hanspeter Herzel. Competing docking interactions can bring about bistability in the MAPK cascade. *Biophys. J.*, 93:2279–2288, 2007.

[143] Jean-Christophe Leloup and Albert Goldbeter. Modeling the molecular regulatory mechanism of circadian rhythms in Drosophila. *BioEssays*, 22(1):84–93, 2000.

[144] Y T Lin, H Kim, and C R Doering. Features of fast living: on the weak selection for longevity in degenerate birth-death processes. *J. Stat. Phys.*, 148:647–683, 2012.

[145] J Liu and P S Ashton. Individual-based simulation models for forest succession and management. *Forest Ecol. Manage.*, 73:157–175, 1995.

[146] Richard Losick and Claude Desplan. Stochasticity and cell fate. *Science*, 320:65–68, 2008.

[147] J.S. Lowengrub, H.B. Frieboes, F Jin, Y.L. Chuang, X Li, P Macklin, S.M. Wise, and V Cristini. Nonlinear modelling of cancer: bridging the gap between cells and tumours. *Nonlinearity*, 23:R1–R9, 2010.

[148] Ben D MacArthur, Colin P Please, and Richard O C Oreffo. Stochasticity and the molecular mechanisms of induced pluripotency. *PLoS One*, 3:e3086, 2008.

[149] P Macklin, S McDougall, A.R.A. Anderson, M.A.J. Chaplain, V Cristini, and J Lowengrub. Multi-scale modelling and nonlinear simulation of vascular tumour growth. *J. Math. Biol.*, 58:765–798, 2009.

[150] Shev MacNamara, Kevin Burrage, and Roger B Sidje. Multiscale Modeling of Chemical Kinetics via the Master Equation. *Multiscale Model. Simul.*, 6:1146–1168, 2008.

[151] Narendra Maheshri and Erin K O'Shea. Living with noisy genes: how cells function reliably with inherent variability in noise expression. *Annu. Rev. Biophys. Biolmol. Struct.*, 36:413–434, 2007.

[152] A Matzavinos and M Ptashnyk. Homogenization of oxygen transport in biological tissues. *Applicable Analysis*, 95:1013–1049, 2016.

[153] A.D. McCulloch. Systems biology and multi-scale modeling of the heart. In *Proccedings of the Biomedical Science & Engineering Conference, 2009*, 2009.

[154] Javier A Menénendez, Jorge Joven, Sívia Cufí, Bruna Corominas-Faja, Cristina Oliveros-Ferreros, Elisabet Cuyás, Begoña Martín-Castillo, Eugeni López-Bonet, Tomás Alarcón, and Alejandro Vázquez-Martín. The Warburg effect 2.0. Metabolic reprogramming of cancer stem cells. *Cell Cycle*, 12:1166–1179, 2013.

[155] Lauren M F Merlo, John W Pepper, Brian J Reid, and Carlo C Maley. Cancer as an evolutionary and ecological process. *Nature Rev. Cancer*, 6:924–935, 2006.

[156] E Moro. Hybrid method for simulating front propagation in reaction-diffusion systems. *Phys. Rev. E.*, 69:060101(R), 2004.

[157] C Morris and H Lecar. Voltage oscillations in the barnacle giant muscle fiber. *Biophysical Journal*, 35(1):193–213, 1981.

[158] James D Murray. *Asymptotic analysis*. Springer-Verlag, New York, NY, USA, 1984.

[159] Jay Newby and Jon Chapman. Metastable behavior in Markov processes with internal states. *J. Math. Biol.*, pages 1–36, 2013.

[160] K Nooter and H Herweijer. Multidrug resistance (mdr) genes in human cancer. *Br. J. Cancer*, 63:663–669, 1991.

[161] B Novak and J J Tyson. A model for restriction point control of the mammalian cell cycle. *J. theor. Biol.*, 230:563–579, 2004.

[162] P.C Nowell. Mechanisms of tumor progression. *Cancer Res.*, 46:2203–2207, 1986.

[163] P.C Nowell. Tumor progression: a brief historical perspective. *Cancer Biol.*, 12:261–266, 2002.

[164] A.C. Oates, N. Gorfinkiel, M. Gonzalez-Gaitan, and C.P. Heisenberg. Quantitative approaches in developmental biology. *Nature Rev. Gen.*, 10:517–530, 2009.

[165] American College of Surgeons. National cancer database.

[166] Bernt Øksendal. *Stochastic Differential Equations*. Springer-Verlag, Berlin, Germany, 2003.

[167] B Ortmann, J Druker, and S Rocha. Cell cycle progression in response to oxygen levels. *Cell. Mol. Life Sci.*, 71:3569–3582, 2014.

[168] J.M. Osborne, A. Walter, S.K. Kershaw, G.R. Mirams, A.G. Fletcher, P Pathmanathan, D Gavaghan, O.E. Jensen, P.K. Maini, and H.M. Bryne. A hybrid approach to multiscale modelling of cancer. *Phil. Trans. R. Soc. A.*, 368:5013–5028, 2010.

[169] N Ouchi, J Glazier, J P Rieu, A Upadhyaya, and Y Sawada. Improving the realism of the cellular Potts model in simulations of biological cells. *Physica A*, 329:451–458, 2003.

[170] Markus R Owen, Tomás Alarcón, Helen M Byrne, and Philip K Maini. Angiogenesis and vascular remodelling in normal and cancerous tissues. *J. Math. Biol.*, 58:689–721, 2009.

[171] Mishal N Patel, Mark D Halling-Brown, Joseph E Tym, Paul Workman, and Bissan Al-Lazikani. Objective assessment of cancer genes for drug discovery. *Nat. Rev. Drug Discov.*, 34:35–50, 2013.

[172] R Penta and D Ambrosi. The role of the microvascular tortuosity in tumor transport phenomena. *J. Theor. Biol*, 364:80–97, 2015.

[173] R Penta, D Ambrosi, and A Quarteroni. Multiscale homogenization for fluid and drug transport in vascularized malignant tissues. *Mathematical Models and Methods in Applied Sciences*, 25:79–108, 2015.

[174] R Penta, D Ambrosi, and R J Shipley. Effective governing equations for poroelastic growing media. *The Quarterly Journal of Mechanics and Applied Mathematics*, 46:69–91, 2014.

[175] Rubén Pérez-Carrasco, Pilar Guerrero, James Briscoe, and Karen M Page. Intrinsic Noise Profoundly Alters the Dynamics and Steady State of Morphogen-Controlled Bistable Genetic Switches. *PLOS Computational Biology*, 12(10):1–23, 2016.

[176] Holger Perfahl, Helen M Byrne, Tingan Chen, Veronica Estrella, Tomás Alarcón, Alexei Lapin, Robert A Gatenby, Robert J Gillies, Mark C Lloyd, Philip K Maini, Matthias Reuss, and Markus R Owen. Multiscale Modelling of Vascular Tumour Growth in 3D: The Roles of Domain Size and Boundary Conditions. *PLoS One*, 6:e14790, 2011.

[177] B Perthame. *Transport equations in Biology*. Birkhauser Verlag, Basel, Switzerland, 2006.

[178] B Perthame. *Parabolic equations in Biology*. Springer, Berlin, Germany, 2015.

[179] G G Powathil, K E Gordon, L A Hill, and M A J Champlain. Modelling the effects of cell-cycle heterogeneity on the response of a solid tumour to chemotherapy: biological insights from a hybrid multiscale cellular automaton model. *J. Theor. Biol.*, 308:1–19, 2012.

[180] G.G. Powathil, D.J.A. Adamson, and M.A.J. Champlain. Towards predicting the response of a solid tumour to chemotherapy and radiotherapy treatments: clinical insights from a computational model. *PLoS Comput. Biol.*, 9:e1003120, 2013.

[181] L Preziosi and A Tosin. Multiphase and Multi-scale Trends in Cancer Modelling. *Math. Model Nat. Phenom.*, 4:1–11, 2009.

[182] Arjun Raj and Alexander van Oudenaarden. Nature, nurture, or chance: stochastic gene expression and its consequences. *Cell*, 135:216–226, 2008.

[183] Christopher V Rao and Adam P Arkin. Stochastic chemical kinetics and the quasi-steady-state assumption: Application to the Gillespie algorithm. *J. Chem. Phys.*, 118:4999–5010, 2003.

[184] Muruhan Rathinam, Linda R Petzold, Yang Cao, and Daniel T Gillespie. Computing communities in large networks using random walks. *J. Chem. Phys.*, 10:12784–12794, 2006.

[185] Sydney Redner. *A guide to first-time passage processes*. Cambridge University Press, Cambridge, U.K., 2001.

[186] K.A. Rejniak and A.R.A. Anderson. Multi-scale hybrid models of tumor growth. *Wiley Interdisciplinary Reviews: System Biology and Medicine*, 3:115–125, 2011.

[187] B Ribba, T Collin, and S Schnell. A multiscale mathematical model of cancer, and its use in analyzing irradiation therapies. *Theor. Biol. Med. Model.*, 3:7, 2006.

[188] James G Robertson. Mechanistic basis of enzyme-targeted drugs. *Biochemistry*, 2005.

[189] M Robinson, M Flegg, and R Erban. Adaptive two-regime method: application to front propagation. *J. Chem. Phys.*, 140:124109, 2014.

[190] Juliano R.V. and V Ling. A surface glycoprotein modulating drug permeability in Chinese hamster ovary cell mutants. *Biochim. Biophys. Acta*, 455:152–162, 1976.

[191] Howard Salis and Yiannis Kaznessis. Accurate hybrid stochastic simulation of a system of coupled chemical or biochemical reactions. *J. Chem. Phys.*, 122:54103, 2005.

[192] A Samant and Dionisios G Vlachos. Overcoming stiffness in stochastic simulation stemming from partial equilibrium: A multiscale Monte Carlo algorithm. *J. Chem. Phys.*, 123:144114, 2005.

[193] Michael Samoilov, Sergey Plyasunov, and Adam P Arkin. Stochastic amplification and signaling in enzymatic futile cycles through noise-induced bistability with oscillations. *Proc. Natl. Acad. Sci.*, 102:2310–2315, 2005.

[194] Daniel Sanchez-Taltavull and Tomas Alarcon. Stochastic modelling of viral blips in hiv-1-infected patients: effects of inhomogeneous density fluctuations. *J. Theor. Biol.*, 371:79–89, 2015.

[195] Kevin R Sanft, Daniel T Gillespie, and Linda R Petzold. Legitimacy of the stochastic Michaelis–Menten approximation. *IET Syst. Biol.*, 5:58–69, 2011.

[196] Santiago Schnell, Philip K Maini, Stuart A Newman, and Timothy J Newman. *Multiscale modeling of developmental systems*, volume 81. 2008.

[197] J G Scott, A G Fletcher, A R A Anderson, and P K Maini. Spatial Metrics of Tumour Vascular Organisation Predict Radiation Efficacy in a Computational Model. *PLoS Comput. Biol.*, 12:e1004712, 2016.

[198] G L Semenza. HIF-1 mediates metabolic responses to intratumoural hypoxia and oncogenic mutations. *J. Clin. Investigation*, 123:3664–3671, 2013.

[199] Y. Setty. Multi-scale computational modeling of developmental biology. *Bioinformatics*, 28:2022–2028, 2012.

[200] R J Shipley and S J Chapman. Multiscale modelling of fluid and drug transport invascular tumours. *Bulletin of Mathematical Biology*, 72:1464–1491, 2010.

[201] H H Shugart. *A Theory of Forest Dynamics: The Ecological Implications of Forest Succession Models*. Springer-Verlag, New York, 1984.

[202] Juswinder Singh, Russell C Petter, Thomas A Baillie, and Adrian Whitty. The resurgence of covalent drugs. *Nature Rev. Drug Discovery*, 10:307–317, 2012.

[203] N.P. Smith, D.P. Nickerson, E.J. Crampin, and P.J. Hunter. Multi-scale computational modelling of the heart. *Acta Numerica*, 13:371–431, 2004.

[204] Paul Smolen, Douglas A Baxter, and John H Byrne. Modeling Circadian Oscillations with Interlocking Positive and Negative Feedback Loops. *Journal of Neuroscience*, 21(17):6644–6656, 2001.

[205] Fabian Spill, Pilar Guerrero, Tomás Alarcón, Philip K. Maini, and Helen Byrne. Mesoscopic and continuum modelling of angiogenesis. Journal of mathematical biology. *Journal of Computational Physics*, pages 1–48, 2014.

[206] Fabian Spill, Pilar Guerrero, Tomás Alarcón, Philip K. Maini, and Helen Byrne. Hybrid approaches for multiple-species stochastic reactiondiffusion models. *Journal of Computational Physics*, 299:429–445, 2015.

[207] Klaus Sterbhard and Axel Ullrich. Paul Ehrlichs magic bullet concept: 100 years of progress. *Nat. Rev. Cancer*, 8:473–480, 2008.

[208] Michael R. Stratton. Exploring the Genomes of Cancer Cells: Progress and Promise. *Science*, 331:1553–1558, 2011.

[209] A B Stundzia and C J Lumsden. Stochastic simulation of coupled reaction–diffusion processes. *Journal of computational physics*, 127:196–207, 1996.

[210] K R Swanson, D Bridge, J Murray, and E C Alvord Jr. Virtual and real brain tumors: using mathematical modeling to quantify glioma growth and invasion. *Journal of the neurological sciences*, 216:1–10, 2003.

[211] A Szabo and R.M.H. Merks. Cellular Potts modeling of tumor growth, tumor invasion, and tumor evolution. *Front. Oncol.*, 3:87, 2013.

[212] Takashi Tateno and Khashayar Pakdaman. Random dynamics of the MorrisLecar neural model. *Chaos: An Interdisciplinary Journal of Nonlinear Science*, 14(3):511–530, 2004.

[213] Uwe C Tauber, Martin Howard, and Benjamin P Vollmayr-Lee. Applications of field-theoretic renormalisation group methods to reaction-diffusion problems. *J. Phys. A: Math. Gen.*, 38:R79—-R131, 2005.

[214] P R Taylor, R E Baker, M J Simpson, and C A Yates. Coupling volume-excluding compartment-based models of diffusion at different scales: Voronoi and pseudo-compartment approaches. *J. R. Soc. Interface*, 13:20160336, 2016.

[215] Philipp Thomas, Ramon Grima, and Arthur V Straube. Rigorous elimination of fast stochastic variables from the linear noise approximation using projection operators. *Phys. Rev. E*, 86:41110, 2012.

[216] Philipp Thomas, Arthur V Straube, and Ramón Grima. Stochastic theory of large-scale enzyme-reaction networks: Finite copy number corrections to rate equation models. *J. Chem. Phys.*, 133:195101, 2010.

[217] Hugo Touchette. The large deviation approach to statistical mechanics. *Phys. Rep.*, 479:1–69, 2009.

[218] P Tracqui. Biophysical models of tumour growth. *Rep. Prog. Phys.*, 72:056701, 2009.

[219] R.D.M. Travasso, E Corvera Poiré, M Castro, J.C. Rodríguez-Manzaneque, and A Hernández-Machado. Tumor angiogenesis and vascular patterning: A mathematical model. *PloS One*, 6:e19989, 2011.

[220] Kunichika Tsumoto, Hiroyuki Kitajima, Tetsuya Yoshinaga, Kazuyuki Aihara, and Hiroshi Kawakami. Bifurcations in Morris-Lecar neuron model. *Neurocomputing*, 69:293–316, 2006.

[221] S Turner and J Sherratt. Intercellular adhesion and cancer invasion: a discrete simulation using the extended Potts model. *J. Theor. Biol.*, 216:85–100, 2002.

[222] Thomas E Turner, Santiago Schnell, and Kevin Burrage. Stochastic approaches for modelling in vivo reactions. *Comp. Biol. Chem.*, 28:165–178, 2004.

[223] John J Tyson, Katherine C Chen, and Bela Novak. Sniffers, buzzers, toggles and blinkers: dynamics of regulatory and signaling pathways in the cell. *Current Opinion in Cell Biology*, 15:221–231, 2003.

[224] John J Tyson and Bela Novak. Regulation of the Eukaryotic Cell Cycle: Molecular Antagonism, Hysteresis, and Irreversible Trasitions. *J. theor. Biol.*, 210:249–263, 2001.

[225] B Verd, A Crombach, and J Jaeger. Classification of transient behaviours in a time-dependent toggle switch model. *BMC Syst. Biol*, 8:43, 2008.

[226] Dionisios G Vlachos. A Review of Multiscale Analysis: Examples from Systems Biology, Materials Engineering, and Other FluidSurface Interacting Systems. *Adv. Chem. Phys.*, 30:1–61, 2005.

[227] J. Walpole, J.A. Papin, and S.M. Peirce. Multi-scale computational models of complex biological systems. *Annu. Rev. Biomed. Eng.*, 15:137–154, 2013.

[228] E Weinan, W Ren, and E Vanden-Eijnden. Minimum action method for the study of rare events. *Communications on Pure and Applied Mathematics*, 57:637–656, 2013.

[229] Robert A. Weinberg. *The Biology of Cancer*. Garland Science, 2013.

[230] W Wen, J Ding, W Sun, K Wu, B Ning, W Gong, G He, S Huang, and X Ding. Cyclin-dependent kinases regulate lysosomal degradation of hypoxia-inducible factor 1a to promote cell-cycle progression. *Cancer Res.*, 70:2010–2019, 2010.

[231] WHO. http://www.who.int/mediacentre/factsheets/fs297/en/.

[232] J Xu, G Vilanova, and H Gomez. A mathematical model coupling tumour growth and angiogenesis. *PLoS One*, 11:e0149422, 2016.

[233] Guang Yao. Modelling mammalian cellular quiescence. *Interface Focus*, 4:20130074, 2014.

[234] Guang Yao, Tae Jun Lee, Seiichi Mori, Joseph R Nevins, and Lingchong You. Asymmetric stochastic switching driven by intrinsic molecular noise. *Nature Cell Biol.*, 7:476–482, 2012.

[235] C A Yates and M B Flegg. The pseudo-compartment method for coupling partial differential equation and compartment-based models of diffusion. *Journal of The Royal Society Interface*, 12, 2015.

[236] R Zhang and H Wang. MDM2 oncogene as a novel target for human cancer therapy. *Curr. Pharm. Des.*, 6:393–416, 2000.

[237] D.I. Zheleva, D.P. Lane, and P.M. Fischer. The p53-Mdm2 pathway: targets for the development of new anticancer therapeutics. *Mini. Rev. Med. Chem.*, 3:257–270, 2003.